BIOMECHANICS AT MICRO- AND NANOSCALE LEVELS

VOL. IV

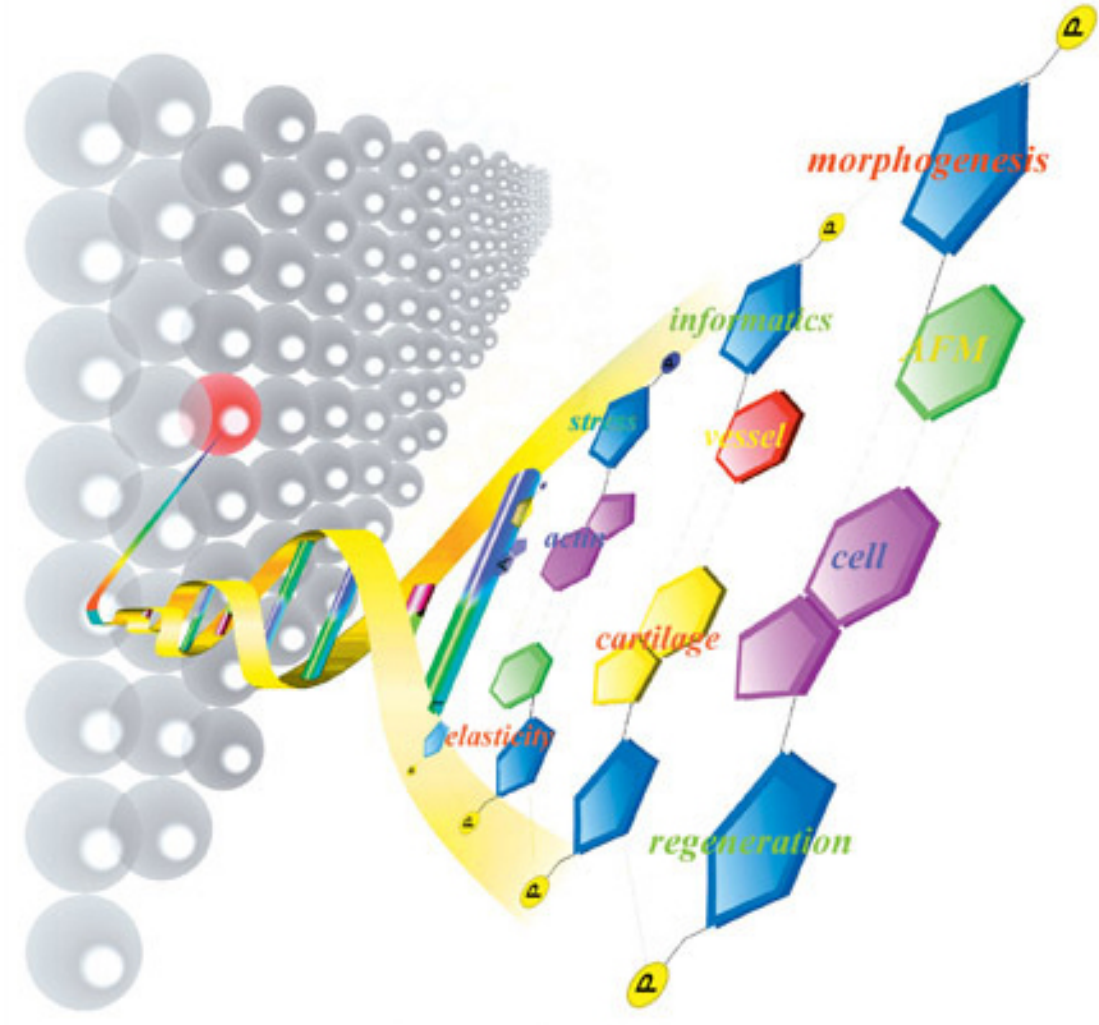

Hiroshi Wada *editor*

BIOMECHANICS AT MICRO- AND NANOSCALE LEVELS

Volume IV

Biomechanics at Micro- and Nanoscale Levels

Editor-in-Charge: Hiroshi Wada
(Tohoku University, Sendai, Japan)

Published

Vol. I: Biomechanics at Micro- and Nanoscale Levels
Edited by Hiroshi Wada
ISBN 981-256-098-X

Vol. II: Biomechanics at Micro- and Nanoscale Levels
Edited by Hiroshi Wada
ISBN 981-256-746-1

Vol. III: Biomechanics at Micro- and Nanoscale Levels
Edited by Hiroshi Wada
ISBN-13 978-981-270-814-4
ISBN-10 981-270-814-6

BIOMECHANICS AT MICRO- AND NANOSCALE LEVELS

Volume IV

editor

Hiroshi Wada

Tohoku University, Sendai, Japan

World Scientific

NEW JERSEY • LONDON • SINGAPORE • BEIJING • SHANGHAI • HONG KONG • TAIPEI • CHENNAI

Published by

World Scientific Publishing Co. Pte. Ltd.

5 Toh Tuck Link, Singapore 596224

USA office: 27 Warren Street, Suite 401-402, Hackensack, NJ 07601

UK office: 57 Shelton Street, Covent Garden, London WC2H 9HE

British Library Cataloguing-in-Publication Data
A catalogue record for this book is available from the British Library.

BIOMECHANICS AT MICRO- AND NANOSCALE LEVELS
Volume IV

ISBN-13 978-981-277-131-5
ISBN-10 981-277-131-X

Printed in Singapore.

PREFACE

A project on "Biomechanics at Micro- and Nanoscale Levels," the title of this book, was approved by the Ministry of Education, Culture, Sports, Science and Technology of Japan in 2003. This four-year-project, carried out by fourteen prominent Japanese researchers, finished in March 2007. The project consisted of four fields of research, which are equivalent to the four chapters of this book, namely, Cell Mechanics, Cell Response to Mechanical Stimulation, Tissue Engineering, and Computational Biomechanics.

Our project can be summarized as follows. The essential diversity of phenomena in living organisms is controlled not by genes but rather by the interaction between the micro- or nanoscale structures in cells and the genetic code, the dynamic interaction between them being especially important. Therefore, if the relationship between the dynamic environment of cells and tissues and their function can be elucidated, it is highly possible to find a method by which the structure and function of such cells and tissues can be regulated. The first goal of this research was to understand dynamic phenomena at cellular and biopolymer-organelle levels on the basis of mechanics. An attempt was then made to apply this understanding to the development of procedures for designing and producing artificial materials and technology for producing or regenerating the structure and function of living organisms.

Volumes I, II and III of a series of books related to this project have already been published, the present volume being the last in this series. The results obtained by individual researchers participating in this project are summarized in this volume.

Hiroshi Wada, PhD,
Project Leader,
Tohoku University,
Sendai,
March, 2007.

This page intentionally left blank

CONTENTS

I. CELL MECHANICS

This page intentionally left blank

STRUCTURAL ANALYSIS OF THE MOTOR PROTEIN PRESTIN

H. WADA, K. IIDA, M. MURAKOSHI AND S. KUMANO

Department of Bioengineering and Robotics, Tohoku University,
6-6-01 Aoba-yama, Sendai 980-8579, Japan
E-mail: wada@cc.mech.tohoku.ac.jp

K. TSUMOTO

Department of Medical Genome Sciences, Graduate School of Frontier Sciences,
The University of Tokyo, 5-1-5 Kashiwanoha, Kashiwa, Chiba 277-8651, Japan

K. IKEDA

Department of Otorhinolaryngology, Juntendo University School of Medicine,
2-1-1 Hongo, Bunkyo-ku, Tokyo 113-8421, Japan

I. KUMAGAI

Department of Biomolecular Engineering, Tohoku University,
6-6-07 Aoba-yama, Sendai 980-8579, Japan

T. KOBAYASHI

Department of Otorhinolaryngology, Head and Neck Surgery, Tohoku University,
Graduate School of Medicine, 1-1 Seiryo-machi, Sendai 980-8675, Japan

The high sensitivity of human hearing is believed to be achieved by cochlear amplification. The basis of this amplification is thought to be the motility of mammalian outer hair cells (OHCs), i.e., OHCs elongate and contract in response to acoustical stimulation. This motility is made possible by the motor protein prestin, which is embedded in the lateral membrane of OHCs. Amino acid sequence analyses showed that prestin is a member of solute carrier (SLC) 26 family. However, information on the structure and function of prestin is limited. In the present study, therefore, attempts were made to generate stable prestin-expressing cell lines using Chinese hamster ovary (CHO) cells and to visualize prestin molecules expressed in their plasma membrane by atomic force microscopy. Results indicate that cell lines stably expressing prestin, the activity of which was confirmed, could be established and that the particle-like structures with a diameter of 8–12 nm observed in their plasma membranes are possibly prestin. In addition, to clarify the mechanism by which prestin functions, mutational analysis of prestin was performed. Results show that the GTSRH sequence highly conserved in the SLC26 family is important for the correct folding of prestin.

1 Introduction

The mammalian ear is characterized by its high sensitivity and sharp frequency selectivity, which are believed to be based on the amplification of basilar membrane vibration in the cochlea. This cochlear amplification is actuated by the motility of

outer hair cells (OHCs), i.e., the OHCs are thought to respond to acoustical stimulation with elongation and contraction of their cylindrical soma *in vivo* [1]. Such responses presumably subject the basilar membrane to force, resulting in amplification of its vibration. This motility is thought to be realized due to the motor protein prestin [2], which is thought to be distributed throughout the plasma membrane. Based on the amino acid sequence of prestin, its membrane topology has been predicted (Fig. 1). However, knowledge about the structure and function of prestin is limited. In the present study, first, to facilitate research on prestin, an attempt was made to generate stable prestin-expressing cell lines using Chinese hamster ovary (CHO) cells. Secondly, to visualize prestin, the plasma membranes of prestin-transfected CHO cells and those of untransfected CHO cells were observed by atomic force microscopy (AFM). Finally, to identify amino acids essential for its structure and function, point mutations were introduced into the prestin sequence and comparison of the characteristics of wild-type prestin with those of point mutants was carried out.

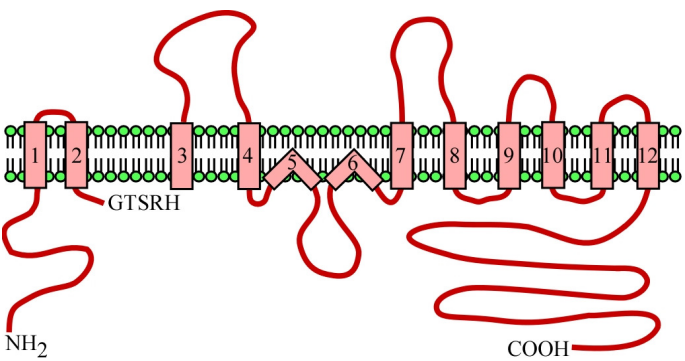

Figure 1. Predicted membrane topology of prestin. Prestin has 12 helices. Helices 5 and 6 form re-entrant loops. The N-terminal and C-terminal are thought to be located in the cytoplasmic side. The GTSRH sequence is located at positions 127-131.

2 Generation of Stable Cell Lines Expressing Prestin

2.1 Materials and methods

CHO-K1 cells were transfected with a pIRES-hrGFP-1a (Stratagene, La Jolla, CA) mammalian expression vector containing gerbil prestin cDNA or C-terminal 3×FLAG-tagged gerbil prestin cDNA. The cells were then plated out at a density of one cell/well in 96-well tissue culture plates. Single colonies contained in these plates were scaled up. Clones showing slow growth were discarded. As the pIRES-hrGFP-1a vector includes the humanized *Renilla reniformis* green fluorescent

protein (hrGFP) gene, transfected clones were chosen based on the fluorescence of hrGFP.

To confirm the expression and localization of 3×FLAG-tagged prestin in the generated cell lines, immunofluorescence experiments were performed. The untransfected CHO cells and those transfected with 3×FLAG-tagged prestin were fixed with 4% formaldehyde in phosphate buffer for 5 min at room temperature and washed with PBS. The samples were then incubated with skimmed milk and fetal bovine serum for 30 min at 37°C. After PBS washing, the cells were incubated with anti-FLAG primary antibody (Sigma, St. Louis, MO) at a 1:250 dilution in PBS with 0.1% saponin solution for 1 hour at 37ºC. The samples were then washed with PBS and incubated with TRITC-conjugated anti-mouse IgG secondary antibody (Sigma) at a 1:70 dilution in PBS containing 0.1% saponin solution for 30 min at 37°C. Finally, the samples were washed with PBS, and immunofluorescence images of the samples were obtained using a confocal laser scanning microscope (Fluoview FV500; Olympus, Tokyo, Japan).

For the motor function of prestin is known to be associated with nonlinear gating charge movement or nonlinear capacitance (NLC) [3, 4]. The activity of prestin is therefore generally evaluated by measuring NLC with the whole-cell patch-clamp method. To confirm the activity of prestin expressed in the generated cell lines, the electrophysiological properties of the cells were measured. Measurements were performed using the membrane test feature of pCLAMP 8.0 software. To determine the voltage dependence of membrane capacitance, cell potential was swung from −140 mV to +70 mV. After the measurements, the membrane capacitance was plotted versus the membrane potential and fitted to the derivative of a Boltzmann function [3],

$$C_{\mathrm{m}}(V) = C_{\mathrm{lin}} + \frac{Q_{\max}}{\alpha e^{\frac{V-V_{1/2}}{\alpha}} \left(1 + e^{-\frac{V-V_{1/2}}{\alpha}}\right)^2}, \tag{1}$$

where C_{lin} is the linear capacitance, $Q_{\max}$ is the maximum charge transfer, α is the slope factor of the voltage dependence of the charge transfer, V is the membrane potential and $V_{1/2}$ is the voltage at half-maximal charge transfer.

2.2 Results and discussion

Cells were plated out into 96 wells after transfection. In the case of CHO cells transfected with prestin, 26 wells contained a single colony, the growth of 22 of them being good. In two of their clones, it was confirmed by fluorescence observation that all cells expressed hrGFP. In the case of CHO cells transfected with 3×FLAG-tagged prestin, 21 wells contained a single colony, the growth of 13 of them being good. In two of their clones, it was confirmed by fluorescence

observation that all cells expressed hrGFP. One of the obtained prestin-transfected cell lines and one of the 3×FLAG-tagged prestin-transfected cell lines were used for the following analysis.

Although introduction of the expression vector and hrGFP expression were clarified by fluorescence observation, the expression of prestin had not yet been confirmed. The expression of 3×FLAG-tagged prestin in generated cells was therefore examined by immunofluorescence experiments. Results are shown in Fig. 2. As shown in this figure, the plasma membrane of the generated cells was stained. By contrast, untransfected cells were not stained. These results show that 3×FLAG-tagged prestin is expressed in the plasma membrane of the CHO cells.

After the expression of prestin was confirmed by immunofluorescence staining, the activity of prestin expressed in the generated cell lines was examined by patch-clamp measurements. The membrane capacitance versus membrane potential measured in a prestin-expressing CHO cell and that measured in a 3×FLAG-tagged prestin-expressing CHO cell are shown in Figs. 3(a) and (b), respectively. As shown in these figures, prestin-expressing cells and 3×FLAG-tagged prestin-expressing cells exhibited voltage-dependent bell-shaped nonlinear membrane capacitance fitted to Eq. (1). In the case of prestin-expressing cells, 20 of the 57 randomly measured cells showed nonlinear membrane capacitance, the fitting parameters of Eq. (1) being obtained as $C_{\mathrm{lin}} = 19.7 \pm 4.1$ pF, $Q_{\mathrm{max}} = 75.5 \pm 37.3$ fC, $\alpha = 38.1 \pm 4.8$ mV and $V_{1/2} = -74.8 \pm 11.6$ mV (mean ± SD). In the case of the 3×FLAG-tagged prestin-expressing cells, 19 of the 53 randomly measured cells showed nonlinear membrane capacitance, the fitting parameters of Eq. (1) being obtained as $C_{\mathrm{lin}} = 24.5 \pm 8.3$ pF, $Q_{\mathrm{max}} = 101.3 \pm 51.9$ fC, $\alpha = 38.0 \pm 5.5$ mV and $V_{1/2} = -73.0 \pm 12.9$ mV (mean ± SD). By contrast, untransfected cells ($n = 21$) did not exhibit nonlinear membrane capacitance (Fig. 3(c)). These results indicate that prestin and 3×FLAG-tagged prestin expressed in the generated cell lines are active. The stable expression of prestin in the established cell lines is advantageous for obtaining prestin molecules.

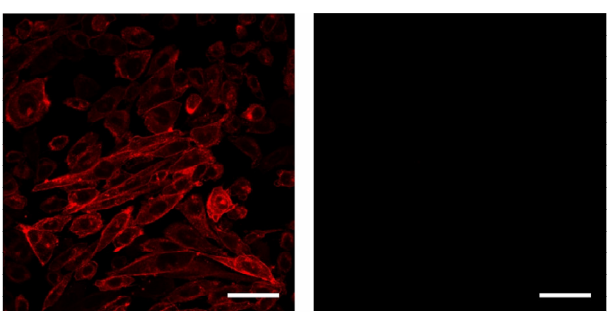

(a) (b)

Figure 2. Immunofluorescence image of CHO cells transfected with 3×FLAG-tagged prestin and that of untransfected CHO cells. (a) 3×FLAG-tagged prestin-transfected CHO cells. (b) Untransfected CHO cells. These results indicate that 3×FLAG-tagged prestin is expressed in the plasma membrane of transfected CHO cells. Scale bars: 50 μm.

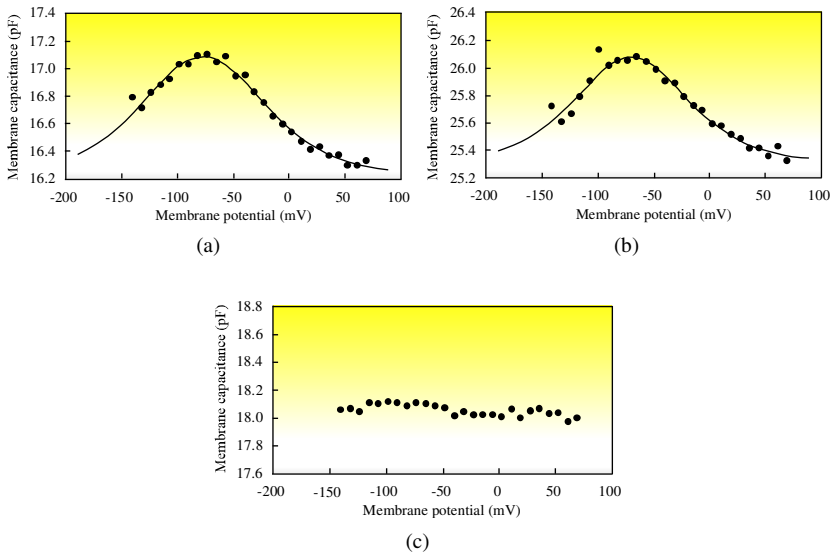

Figure 3. Representative data of the measured membrane capacitance versus membrane potential. (a) Membrane capacitance of a prestin-expressing CHO cell. Data points were fitted to Eq. (1), which is shown by the solid line, with the following parameters: C_{lin} = 16.2 pF, Q_{max} = 127.1 fC, α = 36.8 mV and $V_{1/2}$ = −76.9 mV. (b) Membrane capacitance of a 3×FLAG-tagged prestin-expressing CHO cell. Data points were fitted to Eq. (1), which is shown by the solid line, with the following parameters: C_{lin} = 25.3 pF, Q_{max} = 103.6 fC, α = 33.8 mV and $V_{1/2}$ = −70.4 mV. (c) Membrane capacitance of an untransfected CHO cell.

3 Imaging by Atomic Force Microscopy of the Motor Protein Prestin

3.1 Materials and methods

Experiments were performed in prestin-transfected CHO cells [5] and untransfected CHO cells. Cells were cultured in RPMI-1640 medium with 10% fetal bovine serum, 100 U penicillin/ml and 100 µg streptomycin/ml at 37°C with 5% CO_2. The cells were collected by centrifugation at 250 × *g* for 5 min and the supernatant was removed. The cells were then agitated with an external solution (140 mM KCl, 3.5 mM $MgCl_2$, 5 mM EGTA, 5 mM HEPES and 0.1 mM $CaCl_2$; pH 7.3) and deposited on plastic dishes. After ten minutes, these cells were sonicated in a hypotonic buffer (10 mM PIPES, 10 mM $MgCl_2$, 0.5 mM EGTA; pH 7.2). The membranes attached to the substrate were then incubated with a high salt buffer (2 M NaCl, 2.7 mM KCl, 1.5 mM KH_2PO_4, 1 mM Na_2HPO_4; pH 7.2) and 0.05% trypsin to remove the cytoskeletal materials and the peripheral membrane proteins. The membranes were fixed with 1% glutaraldehyde and then incubated with 2 mM CM-DiI. Finally, the membranes were immersed in filtered 0.1 M phosphate buffer solution.

The AFM system (NVB100, Olympus) used for the experiments consists of a cantilever, laser, mirror, photodiode array, feedback system and piezoscanner. A V-shaped silicon nitride cantilever (OMCL-TR400PSA-2, Olympus) with a spring constant of 0.02 N/m was used. The typical radius of curvature of the cantilever tip was 16 nm. To reduce sample damage during scanning, images were obtained using the oscillation mode (Tapping mode™, Digital Instruments, Santa Barbara, CA).

3.2 Results and discussion

Figure 4 represents three-dimensional AFM images of the isolated plasma membranes of the prestin-transfected and untransfected CHO cells. Particle-like structures were recognized in the plasma membranes of both cells; however, no distinctive difference in such particle-like structures was found between these cells. Since there are many kinds of membrane proteins in the plasma membrane of CHO cells [6, 7], it is impossible to clarify whether the observed structures are prestin or not. Analysis of the shape and size of the observed structures was therefore performed for five AFM images of the prestin-transfected CHO cells and five such images of the untransfected CHO cells. The frequency distribution of the observed particle-like structures, i.e., the density of the particle-like structures plotted against diameter of those structures with 2-nm intervals, is shown in Fig. 5. The diameters of the particle-like structures of the prestin-transfected CHO cells ranged from 6 to 40 nm, and those of the untransfected CHO cells ranged from 6 to 30 nm. When the sizes of the particle-like structures in the plasma membranes were 8–10 nm

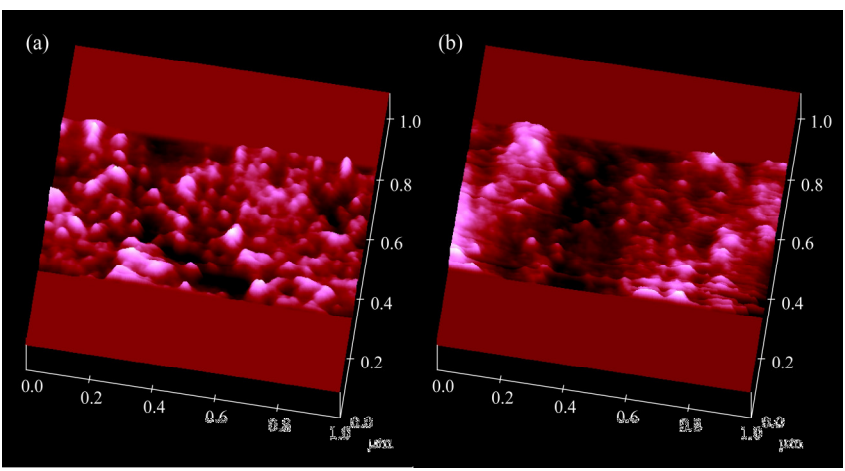

Figure 4. Three-dimensional AFM images of the isolated plasma membranes of the CHO cells. (a) Prestin-transfected CHO cell. (b) Untransfected CHO cell. More particle-like structures with a diameter of 8–12 nm exist in the plasma membrane of the prestin-transfected CHO cells than in that of the untransfected CHO cells.

and 10–12 nm, the differences of their densities between the prestin-transfected CHO cells and the untransfected CHO cells were statistically significant for $P < 0.05$ using Student's t-test, as indicated by asterisks. These diameters were identical to those of the high-density particles (~10 nm) which were observed in the P-fracture face of the lateral membrane of the OHC by electron microscopy [8] and those of the particles which were observed in the cytoplasmic face of the lateral membrane of the OHC by AFM [9]. Since the difference between the prestin-transfected and untransfected CHO cells is due to the existence of prestin, the difference of the densities of the particle-like structures between the prestin-expressing CHO cells and the untransfected CHO cells is considered to be caused by the presence or absence of prestin. Based on Fig. 5, therefore, the density of prestin in the prestin-transfected CHO cells was estimated to be 18 ± 9 proteins/μm^2 (n = 5) after subtracting the value of the density of the particle-like structures in the untransfected CHO cells from those in the prestin-transfected CHO cells in the 8- to 12-nm class. This value corresponds to approximately 75% of the total density of the particle-like structures in the prestin-transfected CHO cell membrane. These results suggest that the majority of these particle-like structures with a diameter of 8–12 nm in the prestin-transfected CHO plasma membrane are possibly prestin.

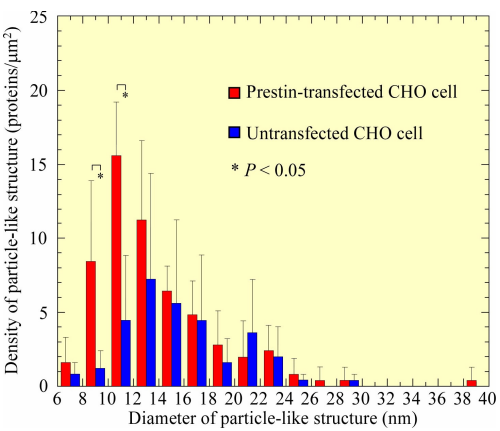

Figure 5. Frequency distribution of the observed particle-like structures in the plasma membrane. The density of the particle-like structure is plotted against the interval in 2-nm classes. Data were obtained from five AFM images of the prestin-transfected CHO cells and five such images of the untransfected CHO cells. When the sizes of the particle-like structures were 8–10 nm and 10–12 nm, differences of their densities between the prestin-expressing CHO cells and the untransfected CHO cells were statistically significant for $P < 0.05$ using Student's t-test, as shown by the asterisks. Error bars represent standard deviations.

4 Mutational Analysis of the GTSRH Sequence of Prestin

4.1 Materials and methods

The GTSRH sequence at positions 127-131 was altered, i.e., alanine was substituted for glycine, threonine, serine, arginine and histidine individually and threonine was substituted for serine, resulting in the following six prestin mutants: G127A, T128A, S129A, R130A, H131A and S129T. These mutants were expressed in human embryonic kidney (HEK) 293 cells for characterization.

Wild-type (WT) prestin-expressing cells exhibit bell-shaped NLC in response to the change of membrane potential. As NLC shows a voltage-dependent charge transfer of prestin, the activity of prestin was evaluated with NLC measured by the whole-cell patch-clamp technique. When the membrane potential of the transfected cells was changed from –140 mV to 70 mV, membrane capacitance was recorded. The recorded membrane capacitance was fitted to Eq (1). To estimate the NLC of the unit cell surface, the normalized NLC $C_{\mathrm{nonlin/lin}}$ was defined as

$$C_{\mathrm{nonlin/lin}}(V) = \frac{C_{\mathrm{nonlin}}}{C_{\mathrm{lin}}} = \frac{\left(C_{\mathrm{m}}(V) - C_{\mathrm{lin}}\right)}{C_{\mathrm{lin}}}, \tag{2}$$

where C_{nonlin} is the nonlinear component of the measured membrane capacitance. Furthermore, to compare the normalized data of the prestin mutants with that of the WT prestin, $C_{\mathrm{nonlin/lin}}(V)$ was divided by the maximum $C_{\mathrm{nonlin/lin}}(V)$ of WT prestin and termed relative $C_{\mathrm{nonlin/lin}}(V)$.

NLC is highly related to the expression level of prestin in the cell membrane. Thus, to investigate the effect of mutations in prestin on its expression level in the cell membrane, this was evaluated by Western blotting using the plasma membrane fraction of transfected cells. The plasma membrane fraction was extracted from transfected cells using a Plasma Membrane Protein Extraction Kit (MBL, Nagoya, Japan) according to the manufacturer's instructions. The plasma membrane fraction were dissolved in SDS sample buffer at a concentration of 2.5×10^5 cells/5 µl for WT prestin and 12.5×10^5 cells/5 µl for empty vectors and the prestin mutants. After boiling for 5 min at 100°C, 5 µl of the cell lysate was subjected to SDS-PAGE and Western blotting.

4.2 Results and discussion

Relative $C_{\mathrm{nonlin/lin}}(V)$ plots are shown in Fig. 6. Data points were fitted to Eq. (1), results of the fitting being shown by solid or dashed lines. WT prestin (n = 20), G127A (n = 10), T128A (n = 10), S129A (n = 10) and R130A (n = 11) exhibited

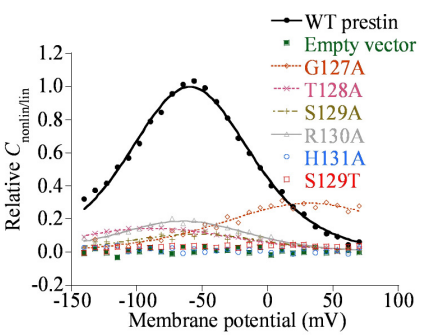

Figure 6. Representative data of patch-clamp recording for WT prestin, G127A, T128A, S129A, R130A, H131A and S129T. Normalized NLC is divided by the maximum of the normalized NLC of WT prestin.

the NLC versus membrane potential. However, the maximum of relative $C_{\text{nonlin/lin}}(V)$ of the prestin mutants were significantly lower than that of WT prestin. On the other hand, the membrane capacitance of cells expressing H131A (n = 11) or S129T (n = 10) versus membrane potential was constant, similar to the data from the cells transfected with the empty vector. The significant reduction or loss of relative $C_{\text{nonlin/lin}}(V)$ indicates that there is a decrease or loss of active prestin molecules in the cell membrane.

The expression levels of the prestin mutants were compared with that of WT prestin by Western blotting. The results of Western blotting are shown in Fig. 7. A strong 100 kDa band was detected in the lane of WT prestin. Two distinct bands of 100 kDa and 80 kDa were observed in the lane of G127A. In the lanes of T128A, S129A and R130A, weak 100 kDa bands and 80 kDa and 70 kDa bands were recognized. In the lanes of H131A and S129T, however, 80 kDa and 70 kDa bands were detected, but no 100 kDa bands were observed. Based on our previous results [10], bands of 100 kDa and 80 kDa were thought to show prestin glycosylated with complex-type oligosaccharides and with high-mannose-type oligosaccharides, respectively, while 70 kDa bands indicated that no glycosylation occurred. In the present results, the 100 kDa bands indicating prestin mutants glycosylated with complex-type oligosaccharides were not detected in the H131A and S129T lanes, which were not thought to be active, according to the results of the patch-clamp recording. In contrast, such bands were observed in the WT prestin, G127A, T128A, S129A and R130A lanes which showed NLC. This result may mean that only the prestin glycosylated with complex-type oligosaccharides is active. Moreover, the plasma membrane fractions of the cells transfected with the prestin mutants, whose concentration was five times higher than that of the plasma membrane fractions of the cells transfected with WT prestin, were used for one lane to detect bands. This may show that most of each prestin mutant was accumulated in the cytoplasm and its expression level in the cell membrane was significantly low. It was therefore considered that the mutations in the GTSRH sequence result in the misfolding of prestin and its accumulation in the cytoplasm, leading to the low

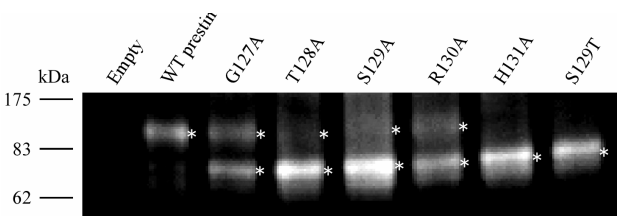

Figure 7. Results of Western blotting using plasma membrane fractions of the cells transfected with WT prestin, G127A, T128A, S129A, R130A, H131A and S129T. 2.5×10^5 cells transfected with WT prestin and 12.5×10^5 cells transfected with the prestin mutants were used for one lane. Asterisks indicate major bands in each lane.

expression level of prestin glycosylated with complex-type oligosaccharides in the cell membrane. The present findings suggest that the GTSRH sequence is important for the correct folding of prestin.

5 Conclusions

In the present study, an attempt was made to generate stable prestin-expressing cell lines using Chinese hamster ovary (CHO) cells. The plasma membranes of prestin-transfected CHO cells and those of untransfected CHO cells were then observed by atomic force microscopy (AFM). Point mutations were introduced into the prestin sequence and comparison of the characteristics of the wild-type prestin with those of the point mutants was carried out. The following conclusions can be drawn:

1. Stable prestin-expressing cell lines were established. The expression and the activity of prestin in the generated cells were confirmed.
2. Particle-like structures with a diameter of 8–12 nm in the prestin-transfected CHO plasma membrane are possibly prestin.
3. The GTSRH sequence highly conserved in the SLC26 family is important for the correct folding of prestin.

Acknowledgments

This work was supported by Grant-in-Aid for Scientific Research on Priority Areas 15086202 from the Ministry of Education, Cultures, Sports, Science and Technology of Japan, Grant-in-Aid for Scientific Research (B) 18390455 from the Japan Society for the Promotion of Science, a Health and Labour Science Research Grant from the Ministry of Health, Labour and Welfare of Japan, Grant-in-Aid for Exploratory Research 18659495 from the Ministry of Education, Culture, Sports, Science and Technology of Japan, a grant from the Human Frontier Science Program, a grant from the Iketani Science and Technology Foundation and a grant from the Daiwa Securities Health Foundation.

References

1. Brownell, W.E., Bader, C.R., Bertrand, D., De Ribaupierre, Y., 1985. Evoked mechanical responses of isolated cochlear outer hair cells. Science 227, 194-196.
2. Zheng, J., Shen, W., He, D.Z.Z., Long, K.B., Madison, L.D., Dallos, P., 2000. Prestin is the motor protein of cochlear outer hair cells. Nature 405, 149-155.

3. Santos-Sacchi, J., 1991. Reversible inhibition of voltage-dependent outer hair cell motility and capacitance. J. Neurosci. 11, 3096-3110.
4. Huang, G., Santos-Sacchi, J., 1993. Mapping of the distribution of the outer hair cell motility voltage sensor by electrical amputation. Biophys. J. 65, 2228-2236.
5. Iida, K., Tsumoto, K., Ikeda, K., Kumagai, I., Kobayashi, T., Wada, H., 2005. Construction of an expression system for the motor protein prestin in Chinese hamster ovary cells. Hear. Res. 205, 262-270.
6. Yang, B., Brown, D., Verkman, A.S., 1996. The mercurial insensitive water channel (AQP-4) forms orthogonal arrays in stably transfected Chinese hamster ovary cells. J. Biol. Chem. 271, 4577-4580.
7. Van Hoek, A.N., Yang, B., Kirmiz, S., Brown, D., 1998. Freeze-fracture analysis of plasma membranes of CHO cells stably expressing aquaporins 1-5. J. Membrane Biol. 165, 243-254.
8. Forge, A., 1991. Structural features of the lateral walls in mammalian cochlear outer hair cells. Cell Tissue Res. 265, 473-483.
9. Le Grimellec, C., Giocondi, M.C., Lenoir, M., Vater, M., Sposito, G., Pujol, R., 2002. High-resolution three-dimensional imaging of the lateral plasma membrane of cochlear outer hair cells by atomic force microscopy. J. Comp. Neurol. 451, 62-69.
10. Kumano, S., Iida, K., Murakoshi, M., Naito, N., Tsumoto, K., Ikeda, K., Kumagai, I., Kobayashi, T., Wada, H., 2006. Importance of the conserved GTSRH sequence in the motor protein prestin. Proceedings of the 9th Western Pacific Acoustic Conference.

EFFECTS OF CYTOSKELETAL STRUCTURES ON ELASTIC AND VISCOELASTIC PROPERTIES OF CELLS IN SOFT TISSUES

T. MATSUMOTO AND K. NAGAYAMA

Department of Mechanical Engineering, Nagoya Institute of Technology, Showa-ku, Gokiso-cho, Nagoya 466-8555, Japan
E-mail: takeo@nitech.ac.jp

H. MIYAZAKI AND Y. UJIHARA

Division of Bioengineering, Department of Mechanical Science and Bioengineering, Graduate School of Engineering Science, Osaka University, 1-3 Machikaneyama-cho, Toyonaka, Osaka 560-8531, Japan

Cytoskeletal structures play crucial roles in mechanical properties of cells. Effects of actin filaments (AFs) and microtubules (MTs) on the elastic properties of cultured fibroblasts (FBs) isolated from rabbit patellar tendons and those of AFs on the viscoelastic properties of cultured rat aortic smooth muscle cells (SMCs) were studied by using micro tensile testers developed in our laboratories. Elastic modulus of FBs measured in a simple tensile test decreased by 75% in response to AF disruption, while the modulus did not change upon MT disruption. Viscoelastic properties of SMCs measured in a stress relaxation test were analysed with a four-parameter Maxwell model, in which stress relaxation response was expressed in a combination of two relaxation processes with different time constants. Elastic modulus of SMCs was similar between the fast and slow relaxation processes and was ~4 times higher than in FBs. The moduli decreased similarly in the fast and slow relaxation processes by 60% in response to AF disruption. Time constant of the slow relaxation process decreased significantly upon AF disruption, while that of the fast process did not change. These results indicate that 1) the effects of MTs on cell mechanical properies are minor compared to AFs; 2) AFs increase not only elastic modulus but also viscoelastic modulus of cells; 3) contribution of cytoskeletons to cell mechanical properties changes depending on cell types. The data obtained in the present study would be useful to estimate the mechanical environment of the cells in the soft tissues.

1 Introduction

It has long been pointed out that soft biological tissues change their mechanical properties and dimensions in response to mechanical environment in which they are exposed. Rabbit patella tendons reduce their tensile strength to 1/10 in 3 weeks if their external load is completely removed [1]. Rat aortic walls increase their thickness in response to hypertension to restore their circumferential stress in a physiological state [2]. These phenomena are driven by the cells in the tissue. Thus, it is very important to know the mechanical properties of cells to estimate stress applied to the cells in the tissue. Conventional mechanical testing methods such as pipette aspiration and nanoindentation are, however, not satisfactory, because we need to know mechanical properties of whole cells under physiological deformation.

From these viewpoints, we have been measuring elastic and viscoelastic properties of cells under large deformation with micro tensile testers developed in our laboratories.

Mechanical properties of cells are largely determined by the cytoskeleton, *i.e.*, polymer networks of actin filaments (AFs), microtubules (MTs), and intermediate filaments (IMs). Among them, AFs play dominant roles in cell mechanical properties, because they are very stiff with high elastic modulus of 1.45 MPa [3], and connect cell surface and internal cell structures directly.

In this chapter, we introduce our studies on the effects of cytoskeletons, mainly of AFs, on the mechanical properties of fibroblasts (FBs) in the patellar tendons and smooth muscle cells (SMCs) in the aortic walls.

2 Contribution of AFs and MTs to Tensile Properties of Fibroblasts

2.1 Materials and methods

Fibroblasts isolated from rabbit patellar tendons with an enzymatic digestion method using collagenase were cultured in DMEM supplemented with 10% fetal bovine serum, 100U/ml penicillin, and 100 μg/ml streptomycin at 37°C. They were subcultured in T-25 tissue culture flasks, and cells at passages 8–12 were treated with 10 μg/ml of cytochalasin D for 3 h (FB-CD) or 0.6 μg/ml of colchicine for 2 h (FB-COL) at 37°C to disrupt actin filaments or microtubules, respectively. Cells were harvested with the treatment of 0.25% trypsin–1 mM EDTA solution for 2 minutes, and washed once with the culture medium. They were then suspended in Hanks' balanced salt solution (HBSS) containing cytochalasin D (10 μg/ml) or colchicine (0.6 μg/ml), and were used for tensile testing. Control data were obtained from non-treated intact cells (FB) in fresh HBSS.

Tensile tests were performed using a tensile tester for single cells that was modified from that reported previously [4]. The tester consists of an inverted microscope (IX-70, Olympus), a thermostatic test chamber, two micromanipulators, a linear actuator (UCM410-5C, Oriental Motor), a CCD camera and a DVD recorder. A micropipette was attached to one of the micromanipulators (MHW-103, Narishige) that can be moved by the linear actuator. A glass microplate was attached to an adaptor that is connected to another micromanipulator (MHW-3, Narishige). Both sides of a floating cell in the test chamber at 37°C were attached to fine tips of the micropipette (outer diameter = 20–40 μm; inner diameter = 3–5 μm) and the microplate (thickness = 15–20 μm; width = 130–160 μm) coated with a urethane resin adhesive (Sista, Henkel). Then, the cell was stretched at the rate of 6 μm/sec by moving the micropipette with a linear actuator. Images of deforming cells were recorded on the DVD recorder via the CCD camera during tensile testing.

After the tensile test, the distance between the micropipette and microplate L, the deflection of each microplate X, and the diameter of the cell perpendicular to the

stretch direction d were measured from the recorded images using an image analyzer (VM-60, Olympus). The elongation of cell ΔL was determined by subtracting initial distance between the pipette and plate L_0 from L. Nominal strain ε was determined as $\varepsilon = \Delta L/L_0$. Tensile load applied to each cell F was calculated by multiplying X with the spring constant of each microplate measured after each test. Nominal stress σ was determined as $\sigma = F/A_0$, where A_0 is initial cross-sectional area of the cell calculated from the initial diameter of the cell assuming circular cross-sectional shape. Initial elastic modulus E_i, the slope of σ–ε curve, was obtained by linear approximation from the region where the cell elongation was not greater than 20 µm.

2.2 *Results and discussion*

The shape of the cells was almost spherical before tensile tests; the diameter of FB, FB-CD, and FB-COL measured before holding with the microtools were 23.1 ± 2.5 µm (mean ± SD, n = 10), 25.0 ± 1.4 µm (n = 6), and 22.3 ± 2.5 µm (n = 6), respectively. Although the diameter was slightly larger in FB-CD than in other groups, there were no significant differences in the cell diameter among the three groups. Examples of the images of cells recorded during tensile testing are shown in Fig. 1. The deformation of cells in FB-CD was much less uniform than in FB. FB-COL showed similar deformation mode to that in FB (not shown).

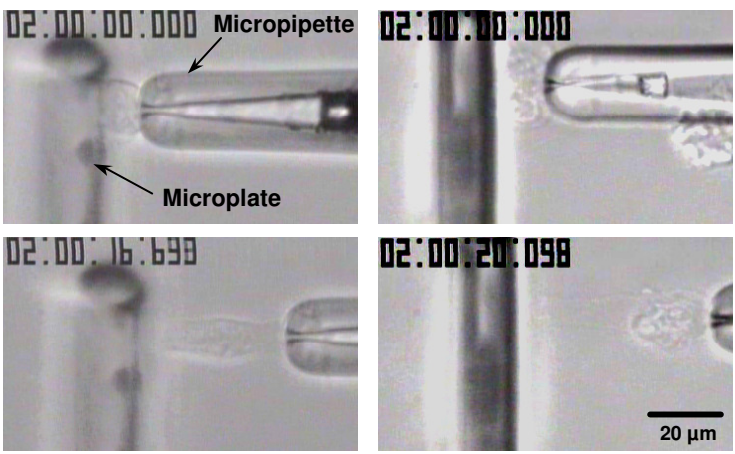

(a) FB (b) FB-CD

Figure 1. Examples of images of (a) non-treated (FB) and (b) cytochalasin D-treated (FB-CD) fibroblasts during tensile testing. As micropipettes were moved by the actuator, microplates were shifted toward the right.

Figure 2 shows the nominal stress-nominal strain curves of each fibroblast. The curves were almost linear in all groups. The slopes of curves were steeper in FB and FB-COL than in FB-CD. The initial elastic modulus E_i decreased by 76% by the treatment with cytochalasin D and was significantly lower in FB-CD (0.35 ± 0.21) than in FB (1.45 ± 0.40) (Fig. 3). This result is similar to that reported in vascular smooth muscle cells [5]. There was no significant difference in E_i between FB and FB-COL (1.60 ± 0.71). These results suggest that actin filaments are the major cytoskeletal component which is responsible for the tensile properties of fibroblasts, and that the contribution of microtubules to the tensile properties is much less than that of actin filaments.

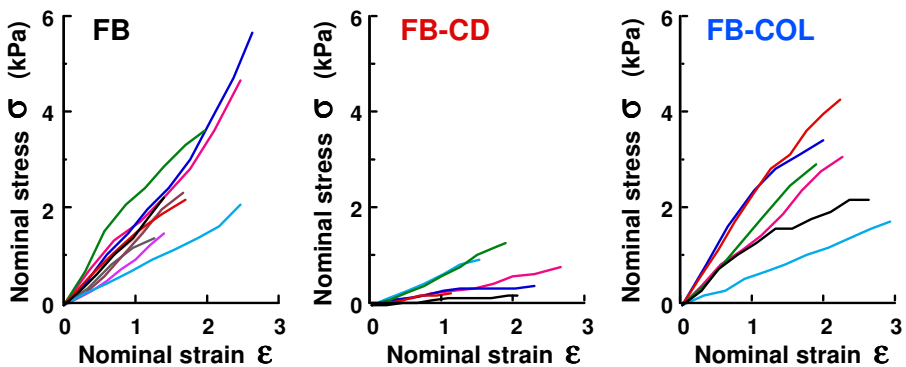

Figure 2. Nominal stress-nominal strain relations of non-treated (FB, n = 10), cytochalasin D-treated (FB-CD, n = 6), and colchicine-treated (FB-COL, n = 6) fibroblasts.

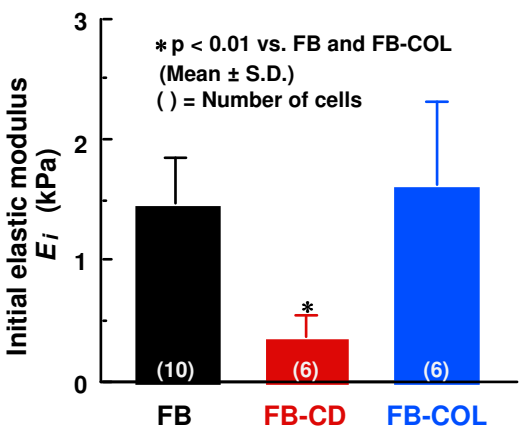

Figure 3. Initial elastic modulus of non-treated fibroblasts (FB) and fibroblasts treated with cytochalasin D (FB-CD) and colchicine (FB-COL). Differences were evaluated by one-way analysis of variance with Bonferroni correction and were considered statistically significant when $p < 0.05$.

3 Contribution of AFs to the Viscoelastic Properties of Single Isolated Aortic Smooth Muscle Cells

3.1 Micro tensile tester for stress relaxation test

Figure 4 shows a schematic diagram (a) and the details of the test section (b) of a micro tensile tester used in the stress relaxation test [6]. A specimen cell was held with two micropipettes by gently pressing their tips onto the cell surface under an inverted microscope (TE2000E, Nikon). The micropipette tips were ~10 µm in diameter, and had been coated with a urethane resin adhesive (Sista M5250, Henkel) [5] to improve adhesion. One micropipette whose spring constant was >100 times higher than that of cultured SMCs (~0.09 N/m [5]) was connected to a 3D micromanipulator (MHW-3, Narishige) and referred to as the rigid pipette. The other pipette, whose spring constant was set to ~0.02 N/m was referred to as the deflectable pipette. The deflectable pipette was moved to stretch the specimen horizontally by using a laboratory-made piezo-actuator whose maximum driving range was ~150 µm, which was large enough for the stress relaxation test for isolated cells. The piezo-actuator was connected to an electric 3D micromanipulator (MMS-77, Shimadzu). The cell stretching process was observed with a CCD camera connected to the microscope. Position of the micropipette tips was tracked using an image processor (Percept Scope C8840, Hamamatsu Photonics) to obtain the x coordinate of the tips (Fig. 4(b)). Cell images during stretching were also recorded on a DVD video recorder.

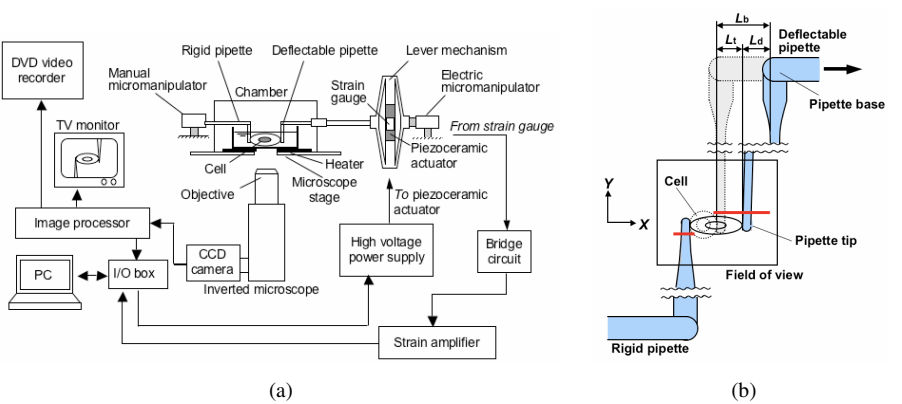

Figure 4. Schematic diagram of the micro tensile tester for stress relaxation test of isolated cells (a), and the details of its test section (b). Red lines in the field of view indicate the binarized regions to track the outline edge of the pipettes with the image processor.

The tension applied to specimen cell T was calculated by multiplying the deflection of the deflectable pipette L_d with its spring constant k, that had been

calibrated by a standard cantilever with known spring constant before each test. L_d was calculated as $L_d = L_b - L_t$, where L_b is the displacement of the base of the deflectable pipette and L_t is the displacement of the pipette tip (Fig. 4(b)). To determine L_b, we attached a strain gauge to the surface of the piezo ceramics of the actuator and measured the deformation of the ceramics directly. The signals corresponding to L_b and L_t were recorded on a personal computer, and the distance between the two pipettes was kept constant by proportional feedback control of L_b using a program written with LabVIEW (Ver. 6.1, National Instruments).

Figure 5 shows typical examples of time-course changes of T and the relative length of the specimen cells in the stress relaxation test of the isolated cultured aortic smooth muscle cells which were stretched from an initial length L_{ini} to a preset length L^*=1.75L_{ini}. Although T differed among cells in the relaxation test, the maximum difference between the cell length and L^* was less than 1%, and the cell length was kept almost constant throughout the stress relaxation test.

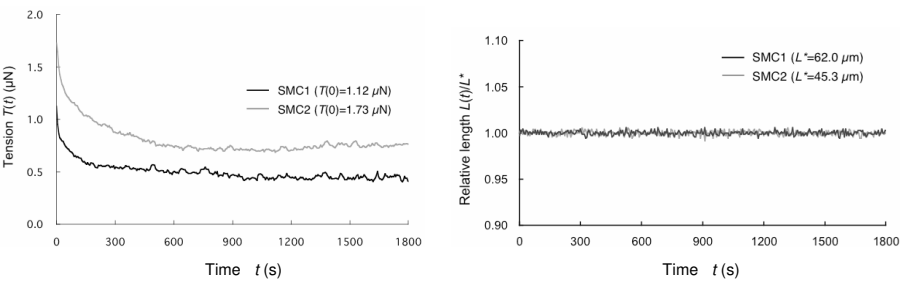

Figure 5. Typical examples of the time-course changes of tension (left) and relative length (right) of cultured aortic smooth muscle cells during the stress relaxation test. L^*, preset length of each cell; $L(t)$, cell length at time t.

3.2 Materials and methods

Rat aortic smooth muscle cells (SMCs) isolated using enzymatic digestion method [5] and passaged >3 times in culture were used as a test model. We used two types of specimens, untreated SMCs and SMCs whose actin filaments were disrupted with cytochalasin D (SMCs-CD).

SMCs cultured on dishes in DMEM supplemented with 10% fetal bovine serum and 1% Penicillin-Streptomycin at 37ºC in 5% CO_2 and 95% air were harvested with trypsinization, and were diluted by at least 1/100 with Ca^{2+}-Mg^{2+}-free Hank's balanced salt solution (HBSS(-)) and placed in a dish at 37ºC to remove the effect of trypsinization. We used cells for the test within 1-3 h after trypsinization, because in the previous study, fiber structure of actin filaments in the detached cells looked recovered fully 1 h after trypsinization [6]. The dish was set on the microscope stage of the micro tensile tester. A single cell in the dish was held with the two micropipettes at each end, and set at no load by moving the rigid pipette to

put the deflectable pipette at the no load position that had been determined before the test (Fig. 6(a)). In case of the SMCs-CD, HBSS(-) was supplemented with 2 μg/ml cytochalasin D and the cell was held on the pipettes for 1 h to disrupt its actin filaments.

Stress relaxation test was employed to measure the viscoelastic properties of the SMCs. Cells were stretched from L_{ini} to L^* that would elongate the cell by 70–85% (L^* = (1.70–1.85) L_{ini}) under proportional control (stretching phase). Cell length was kept constant for 20-30 min using position feedback control (constant length phase). The beginning of the constant length phase was taken as time zero. The diameter of the cell $D(0)$ at time zero was calculated by dividing the tracing area of the cell $S(0)$ with the distance between the two pipettes $L(0) = L^*$, given by $D(0) = S(0)/L(0)$ (Fig. 6(b)). The mean cross-sectional area of the cell $A(0)$ was calculated by assuming that the cell cross-sectional shape perpendicular to the stretch axis is circular: $A(0) = \pi(D(0)/2)^2$. The tension applied to specimen cell T was calculated by multiplying the deflection of the deflectable pipette with their spring constant. The tension at time t, $T(t)$ was normalized with the cross-sectional area of the cell $A(0)$ given by $T^*(t) = T(t)/A(0)$, to reduce the effects of cell dimension on the mechanical properties, and is referred to as the normalized tension. Time course changes in the deflection $L_d(t)$ were recorded during the relaxation test to measure changes in the normalized tension $T^*(t)$.

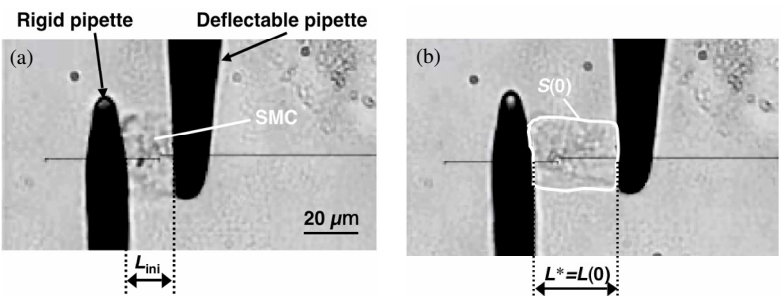

Figure 6. A smooth muscle cell held with micropipettes before (a) and at the end of the stretching phase (b). Horizontal black lines show the binarized regions to track the outline edge of the pipettes with the image processor. The tips of the glass micropipettes were painted black in order to enhance image binarization.

3.3 Analysis

Stress relaxation in response to stretching was modeled using a four-parameter Maxwell model (Fig. 7) consisting of two parallel Maxwell chains, a serial combination of an elastic component with elastic parameter K^* and a dashpot with viscous parameter V^*. By assuming a step input of strain $\varepsilon(0)$, the normalized tension during the relaxation process $T^*(t)$ was expressed by the following equation:

$$T^*(t) = \left\{ K_0^* \cdot \exp\left(-\frac{t}{\tau_0} \right) + K_1^* \cdot \exp\left(-\frac{t}{\tau_1} \right) \right\} \cdot \varepsilon(0) , \quad (1)$$

where the relaxation time constant τ_0 equals V^*_0/ K^*_0, τ_1 equals V^*_1/ K^*_1, and $\varepsilon(0)$ represents the strain at the beginning of the constant length phase, $\varepsilon(0)=(L(0)-L_{ini})/L_{ini}$. Model parameters were determined by minimizing errors between the theoretical and experimental curves for each cell under the following preconditions:

$$T^*(0) = (K_0^* + K_1^*) \cdot \varepsilon(0) \ , \quad V_0^* < V_1^* . \quad (2)$$

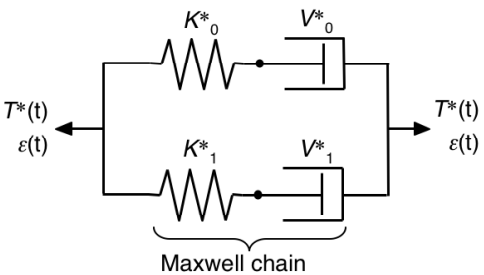

Figure 7. Four-parameter Maxwell model used in viscoelastic analysis. K^*, elastic parameter; V^*, viscous parameter; $T^*(t)$, normalized tension; $\varepsilon(t)$, strain. A serial combination of K^* and V^* is referred to as a Maxwell chain.

3.4 Results and discussion

Actin filaments in untreated SMCs were relatively abundant and looked aggregated and entangled fiber shape, while in SMCs-CD, they looked granular (Fig. 8). Thus, we confirmed the actin disruption with cytochalasin D treatment, and used these two groups for mechanical tests.

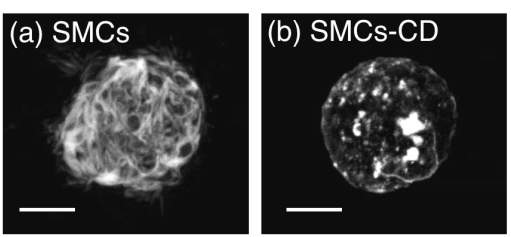

Figure 8. Examples of the morphology of actin filaments in SMCs (a) and SMCs-CD (b) detached from the substrate obtained using a confocal laser scanning microscope. Scale bars = 10 μm.

Figure 9 summarizes the relaxation function ($T^*(t)/ T^*(0)$) of the cells. The normalized tension decreased exponentially in all cells. The stress relaxation response had a wide variation in both groups. Tension fluctuation was observed in the SMCs, while the curves for SMCs-CD were relatively smooth. The fitting with the four-parameter Maxwell model was almost satisfactory up to 1800s in the curves for both SMCs and SMCs-CD (Fig. 10, $R^2 > 0.94$).

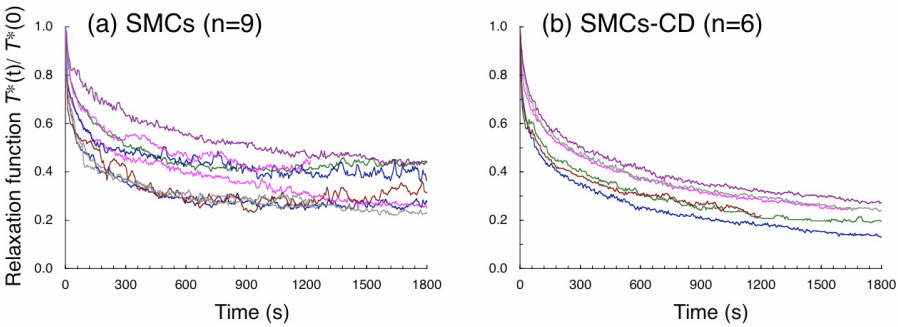

Figure 9. Stress relaxation curves expressed in the form of a relaxation function.

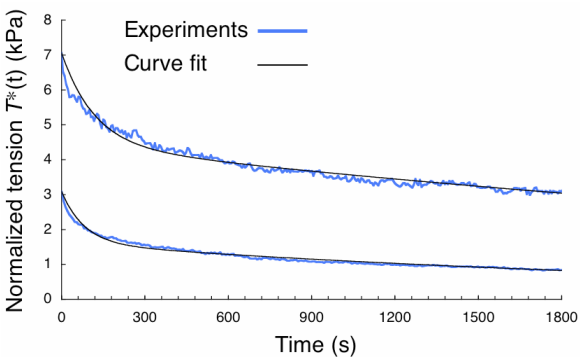

Figure 10. Typical examples of the stress relaxation curves for SMCs and SMCs-CD fitted by the four-parameter Maxwell model.

In the untreated SMCs, although the two elastic parameters parameters K^*_0 and K^*_1 were similar in value, the viscous parameters V^*_1, was over 50 times larger than V^*_0 (Table 1). This indicates that the stress relaxation response was made of two phases: a fast phase and a slow phase. The fast phase, in which the cells decrease their internal stress quickly by their intrinsic mechanical properties, is characterized by the elastic element K^*_0 and the viscous element V^*_0. The slow phase, in which the cells decrease the internal stress more slowly possibly by their cytoplasmic streaming and reorganization of intracellular structures, is characterized by the elastic element K^*_1 and the viscous element V^*_1. We found that the relaxation time constant in the fast phase τ_0 was in the order of minutes, whereas it was in the order of hours in the slow phase τ_1 (Table 1).

Disruption of actin filaments caused significant changes in mechanical properties of SMCs (Table 1). Decrease in the elastic parameters K^*_0 and K^*_1 in

SMCs-CD indicates that cells soften with actin disruption, which is similar to that obtained in the *quasi-static* tensile test [5] and other studies [7-9]. Viscosity of the cells also decreased with actin disruption. It has been reported that viscous properties of endothelial cell surface mesured with magnetic twisting cytometry did not change after actin disruption [7]. On the contrary, Trickey et al. [8] measured the viscoelastic properties of the articular chondrocytes under relatively large deformation using a micropipette aspiration technique, and reported that the viscosity of the cells decreased up to 80% with actin disruption. The cells in this study were also exposed to relatively large deformation (ε = 70–85%). These results may indicate that actin filaments have significant effects not only on elastic but also viscous properties of cells under large deformation. In SMCs-CD, the paremeters in the fast phase K^*_0 and V^*_0 decreased equally, and as a consequence, no difference was observed in the relaxation time constant τ_0 after actin disruption (Table 1). On the other hand, the viscous parameter in the slow phase V^*_1 decreased much more than that of elastic parameter K^*_1 with actin disruption, causing significant decrease in the relaxation time constant in the slow phase τ_1. These results indicate that actin filaments may have significant effect on the slow phase of the stress relaxation of the cells possibly through their active reorganization and/or temporal change in tension in actin filaments driven by their interaction with myosin.

We also found that tension fluctuation during stress relaxation process decreased with actin disruption: root mean square of stress relaxation curves in SMCs-CD (0.024 ± 0.005 kPa, mean ± SEM, n = 6) significantly smaller than that in untreated SMCs (0.101 ± 0.023 kPa, n = 9). These may also indicate that the fluctuation may be caused by active reorganization of actin filaments and/or their dynamic interaction with myosin molecules.

Table 1. Summary of the viscoelastic parameters of SMCs and SMCs-CD obtained with the four-parameter Maxwell model.

Specimens	K^*_0 (kPa)	K^*_1 (kPa)	V^*_0 (kPa·s)	V^*_1 (kPa·s)	τ_0 (s)	τ_1 (s)
SMCs (n=9)	6.48±1.80	5.62±1.07	407±108	22270±5107	62±10	3798±529
SMCs-CD (n=6)	2.49±0.59 #	2.39±0.43 #	109±24 #	4737±699 #	47±10	1816±228 #

K^*_0 and K^*_1, elastic parameters; V^*_0 and V^*_1, viscous parameters; τ_0 and τ_1, relaxation time constants (= V^*_n/ K^*_n, n = 1, 2). #P < 0.05.

4 Conclusions

As suggested in the Introduction, AFs had a strong influence on the mechanical properties of both FBs and SMCs. Elastic modulus decreased by 75% for FBs and 60% for SMCs upon AF disruption. In contrast, the influence of MTs was minor. This might be because MTs are not connected directly to the cell membrane as AFs are. FBs were much softer than SMCs and affected much more by actin disruption.

This might be attributable to thinner actin bundles in FBs than in SMCs [4]. Ratio of AFs to other cytoskeletal elements might also be higher in FBs than in SMCs. Further accumulation of data on the effects of disruption of cytoskeletal elements on the mechanical properties of various types of cells and analysis of their relation to cytoskeletal network morphology are necessary.

Acknowledgments

This work was supported in part by Grant-in-Aid for Scientific Research on Priority Areas 15086209 and Grant-in-Aid for Exploratory Research 17650135 both from MEXT, and Grant-in-Aid for Scientific Research (B) 16360052 from JSPS.

References

1. Yamamoto, N., Ohno, K., Hayashi, K., Kuriyama, K., Yasuda, K., Kaneda, K., 1993. Effects of stress shielding on the mechanical properties of patellar tendon. ASME J. Biomech. Eng. 115, 23-28.
2. Matsumoto, T., Hayashi, K., 1994. Mechanical and Dimensional adaptation of rat aorta to hypertension. J. Biomech. Eng. 116, 278-283.
3. Deguchi, S., Ohashi, T., Sato, M., 2006. Tensile properties of single stress fibers isolated from cultured vascular smooth muscle cells. J. Biomech. 39, 2603-2610.
4. Miyazaki, H., Hasegawa, Y., Hayashi, K., 2002. Tensile properties of fibroblasts and vascular smooth muscle cells. Biorheology 40, 207-212.
5. Nagayama, K., Nagano, Y., Sato, M., and Matsumoto, T., 2006. Effect of actin filament distribution on tensile properties of smooth muscle cells obtained from rat thoracic aortas. J. Biomech. 39, 293-301.
6. Nagayama, K., Yanagihara, S., Matsumoto, T., 2007. A novel micro tensile tester with feed-back control for viscoelastic analysis of single isolated smooth muscle cell. Med. Eng. Phys. 29, 620-628.
7. Wang, N., 1998. Mechanical interactions among cytoskeletal filaments. Hypertension 32, 162-165
8. Trickey, W.R., Lee, G.M., Guilak, F., 2000. Viscoelastic properties of chondrocytes from normal and osteoarthritic human cartilage. J. Orthop. Res. 18, 891-898.
9. An, S.S., Laudadio, R.E., Lai, J., Rogers, R.A., Fredberg, J.J., 2002. Stiffness changes in cultured airway smooth muscle cells. Am. J. Physiol. Cell Physiol., 283, 792-801.

BIOMECHANICAL PROPERTIES OF COLLAGEN GEL ASSOCIATED WITH MICROVESSEL FORMATION IN VITRO

K. TANISHITA, N. YAMAMURA, R. SUDO AND M. IKEDA

Department of System Design Engineering, Keio University,
3-14-1 Hiyoshi, Kohoku-ku, Yokohama 223-8522, Japan
E-mail: tanishita@sd.keio.ac.jp

Vascularization by endothelial cells (ECs) is an important element in tissue engineering of organoids. Morphogenesis of these cells is regulated not only by biochemical properties of the extracellular matrix (ECM) but also by its mechanical properties. Here, we investigated the effect of adhesion substrate elasticity on the formation of capillary-like networks by ECs; in particular, we examined the three-dimensional (3D) configurations of the resulting networks. Bovine pulmonary microvascular ECs were cultured on a series of collagen gels of different elasticities but the same collagen concentration. The cells cultured in rigid and flexible gels formed 3D networks via different processes; cells formed dense, thin networks in the flexible gel, whereas thicker and deeper networks were formed in the rigid gel. Cross-sections of the networks revealed that those formed within the rigid gel had large lumens composed of multiple cells, whereas those formed within the flexible gel had small, intracellular vacuoles.

1 Introduction

Formation of vascular networks within tissue-engineered organoids is important in achieving successful organ replacement therapy [1, 2] because vascularization is essential to supply cells with nutrients and oxygen and to remove waste products. Whereas two-dimensional (2D) tissues, such as skin and cornea, have been successfully reconstructed, reconstruction of three-dimensional (3D) tissues, such as liver and heart, remains difficult.

Mechanical properties of the ECM, as well as biochemical properties, are critical for the control of cell and tissue morphology and function [3, 4]. Several in vitro models have been developed, and studies using these models have shown that the mechanical properties of substrates affect the locomotion of fibroblasts and epithelial cells [5], the proliferation and apoptosis of fibroblasts [6], and the cytoskeletal reorganization, cytoskeleton–ECM coupling, and focal adhesion of ECs [7]. These results suggest that the mechanical properties of substrates influence angiogenesis through a complex process that affects many cellular responses, including migration, proliferation, and differentiation [8]. However, the various mechanical properties of the ECM and their effects on the formation and 3D configuration of EC capillary networks are not well understood.

In the present study, we investigated effects of the mechanical properties of collagen gel on the formation of 3D capillary-like networks within these gels. The result of this study is described in the literature of Yamamura et al. [9].

2 Materials and Methods

2.1 Cell culture

BPMECs were purchased from Cell Systems (Kirkland, WA) and cultured in Dulbecco's modified Eagle's medium (DMEM; Invitrogen, Carlsbad, CA) supplemented with 10% fetal bovine serum, 1% antibiotic-antimycotic (Invitrogen), and 15 mM HEPES (Dojindo, Kumamoto, Japan). The cells of the sixth to tenth passage were used in all experiments.

2.2 Preparation of collagen gels

To prepare collagen mixtures, eight volumes of 3.0 mg/ml acid-soluble type I collagen solution derived from porcine tendon (Cellmatrix Type I-A; Nitta Gelatin, Osaka, Japan) were mixed with one volume of 10× minimum essential medium (Invitrogen) and one volume of 0.08 N NaOH supplemented with 20 mM HEPES on ice. The mechanical properties of collagen gels can be modulated by varying the pH of the collagen solutions during polymerization [10]. The pH of the collagen mixtures was varied from 5 to 10 and verified using a pH meter (KS 723; Shindengen Electric Manufacturing, Tokyo, Japan). The pH-adjusted collagen mixtures were poured into culture dishes and polymerized at 37°C. After polymerization, the collagen gels were incubated with phosphate buffered saline (PBS) in a humidified incubator at 37°C under 5% CO_2–95% air.

2.3 Measurement of Young's modulus (elasticity) of collagen gels

Uniaxial compression tests of collagen gels polymerized at pH 5–10 were performed using a creep meter (RE33005; Yamaden, Tokyo, Japan). Collagen solutions were polymerized within a cylindrical chamber (15 mm in diameter, 5 mm in height) and were then deformed by a columnar plunger of 12 mm in diameter at a rate of 50 μm/sec at 34 ± 2°C. The collagen gels were uniaxially compressed to half their original heights (50% of the distortion rate), and the stress–strain curve of each gel was recorded. Young's modulus, which is given by the stress–strain ratio at very small deformations (5–15% of the distortion rate), was used as the flexibility parameter for the collagen gels.

2.4 In vitro network formation model

An in vitro 3D network model was used as described previously [11]. BPMECs were seeded onto 1.53-mm-thick collagen gels in 35-mm culture dishes (4×10^5 cells/dish). At 24 h after seeding, 30 ng/ml bFGF (Recombinant Human Fibroblast Growth Factor-basic; PeproTech, Rocky Hill, NJ) was added to the culture medium to promote network formation [12]. This 3D network model was used in the cell culture experiments.

3 Results

3.1 Mechanical properties of collagen gels depend on the pH of the collagen polymerization solution

We prepared a series of collagen gels polymerized at pHs of 5 to 10, and their Young's moduli were determined as a macroscopic mechanical parameter. The Young's moduli of the collagen gels as a function of pH are shown in Fig. 1. The gels became more rigid as the pH of the collagen polymerization solution increased, with Young's modulus values increasing linearly from pH 5 to 8 and then plateauing at pH 8. The Young's modulus at pH 9 was 4.6 times greater than that at pH 5. In subsequent experiments, collagen gels that were polymerized at pH 5 (E = 4500 ± 1500 Pa) were used as "flexible" gels, and those polymerized at pH 9 (E = 20800 ± 3100 Pa) were used as "rigid" gels.

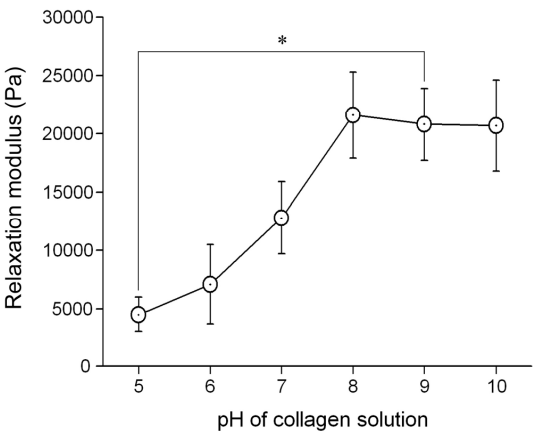

Figure 1. Effect of collagen solution pH on Young's modulus of collagen gels. The pH of the collagen polymerization solutions was varied from 5 to 10. Young's moduli were calculated using stress–strain curves determined from uniaxial compression tests. Data are the means ± SD; n = 25–28; $^*P < 0.05$.

Because the macroscopic mechanical properties of the collagen structures are affected by their microscopic structures, we examined microscopic structure using scanning electron microscopy. We found that fibril diameters increased as the polymerization pH decreased (arrowheads, Fig. 2A–C). Fibril diameters at pH 5 and 9 were approximately 41 and 28 nm, respectively (Fig. 2D).

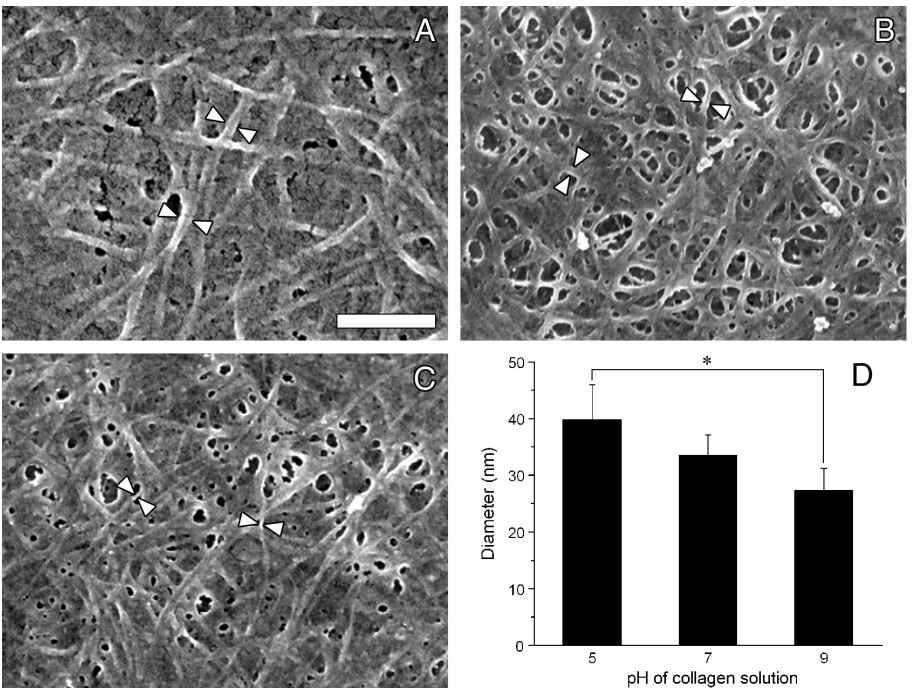

Figure 2. Scanning electron micrographs of reconstructed collagen fibrils. A–C: Collagen gels were polymerized at pH 5 (A), pH 7 (B), and pH 9 (C). Arrowheads indicate collagen fibrils. D: Effect of collagen solution pH on fibril diameters, which decreased as pH increased. The specimens were examined at 5 kV under a field emission scanning electron microscope and all images were taken at the same magnification. Scale bar, 500 nm. Data are the means ± SD; $n = 30$; $^*P < 0.05$.

3.2 Collagen gel elasticity affects the process of network formation by BPMECs

To address the effect of collagen gel elasticity on network formation by BPMECs, the cells were cultured on flexible (pH 5) or rigid (pH 9) gels. The morphology of the networks formed in the gels differed significantly according to gel elasticity (Fig. 3). When cultured on the flexible gel, extended BPMECs formed networks in the gel at day 3 of culture (arrowheads, Fig. 3A). The number of sprouting cells increased and complex networks were formed at day 5 of culture (arrowheads, Fig. 3B). In contrast, when the cells were cultured on the rigid gel, they formed aggregates in the gel (arrowheads, Fig. 3C). In addition, filamentous cytoplasmic processes extended from the aggregates (arrows, Fig. 3C, D). The cells formed thicker networks in the rigid gel than in the flexible gel at day 5 of culture (Fig. 3B, D).

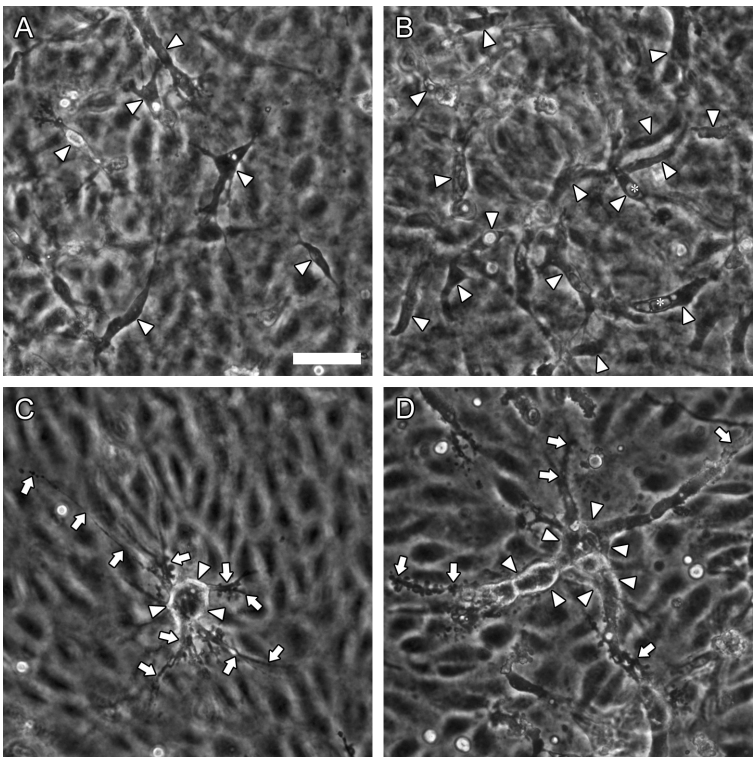

Figure 3. Phase-contrast images of 3D networks forming in flexible (A, B) and rigid (C, D) gels. A, B: Representative images of BPMECs forming networks in flexible gels at day 3 (A) and day 5 (B) of culture. The cells formed thin dense networks, and the number of sprouting cells increased with culture time (arrowheads). Some vacuoles were observed within the cells forming networks (asterisks, B). C, D: Representative images of the cells forming networks in rigid gels at day 3 (C) and day 5 (D) of culture. The cells formed aggregates (arrowheads, C) with filamentous cytoplasmic processes (arrows, C) in the gel. An aggregate developed into thick networks (arrowheads, D). The cytoplasmic processes were mainly formed at tips of the networks. All images were taken at the same magnification. Scale bar, 50 μm.

3.3 Collagen gel elasticity affects the structure of 3D networks formed by BPMECs

The 3D structures of the networks were examined using confocal laser scanning microscopy. In the flexible gel, most cells invaded the gel beneath the cell monolayer and formed thin dense networks (Fig. 4A). The network density was 2.6 times higher than that of networks formed in the rigid gel (data not shown). Lateral views of the 3D network revealed that most of the network structures were distributed in the region 0–50 μm beneath the gel surface (Fig. 4C). In contrast, cells

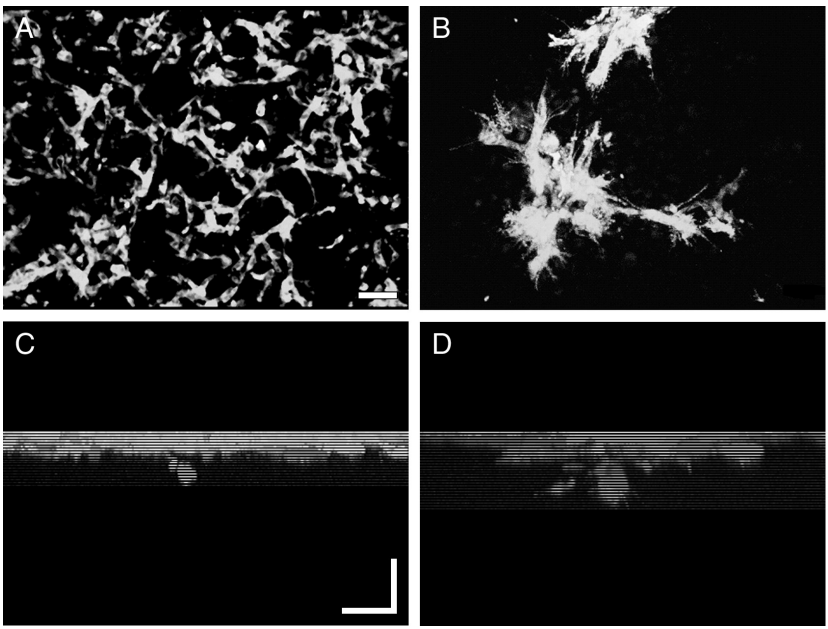

Figure 4. Images of 3D network structures in flexible (A, C) and rigid (B, D) gels at day 7 of culture. Confocal images were recorded at 5-μm depth intervals, starting with cells on the gel surface. A, B: Z-projection images of the 3D networks. To remove images of cell monolayers, the images of the 3D networks were reconstructed using images taken at depths >15 μm. C, D: Lateral views of the 3D networks containing the images of cells on the gel surfaces. Images were taken at the same magnification. Scale bars, 100 μm (A, C).

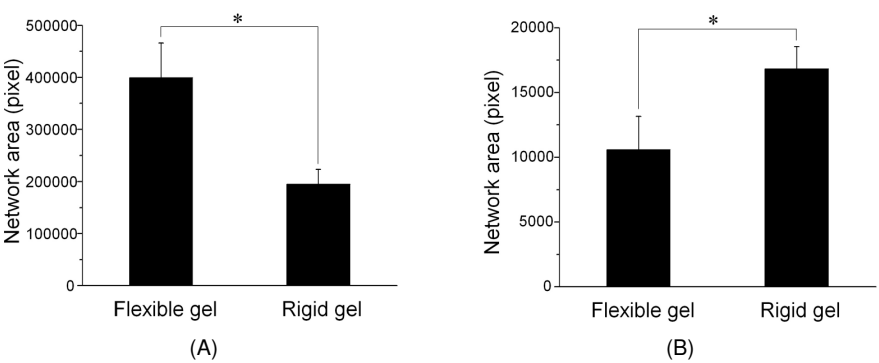

Figure 5. Total area of networks formed in vertical sections of rigid and flexible gels. A: 15–40 μm beneath the surface; B: >40 μm beneath the surface. Data are the means ± SD; $n = 30$; $^*P < 0.05$.

in the rigid gel invaded into the gel as clumps and formed thick networks that were sparsely distributed (Fig. 4B). Cells in the rigid gel formed much deeper networks than those formed in the flexible gel, with some reaching about 120 µm beneath the gel surface (Fig. 4D).

In addition to quantifying the network distribution as a function of depth, we also quantified the amount of network structure formed. The relationship between the total area of networks formed in flexible vs. rigid gels changed at a depth of 40 µm. The total area of networks formed in the region 15–40 µm beneath the gel surface and at depths >40 µm are shown in Fig. 5A and B, respectively. Closer to the gel surface (depth of 15–40 µm), the total area of networks formed in the flexible gel was twice that of networks formed in the rigid gel (Fig. 5A). However, at depths >40 µm, the total area of networks formed in the rigid gel was 1.6 times greater than that of networks formed in the flexible gel (Fig. 5B).

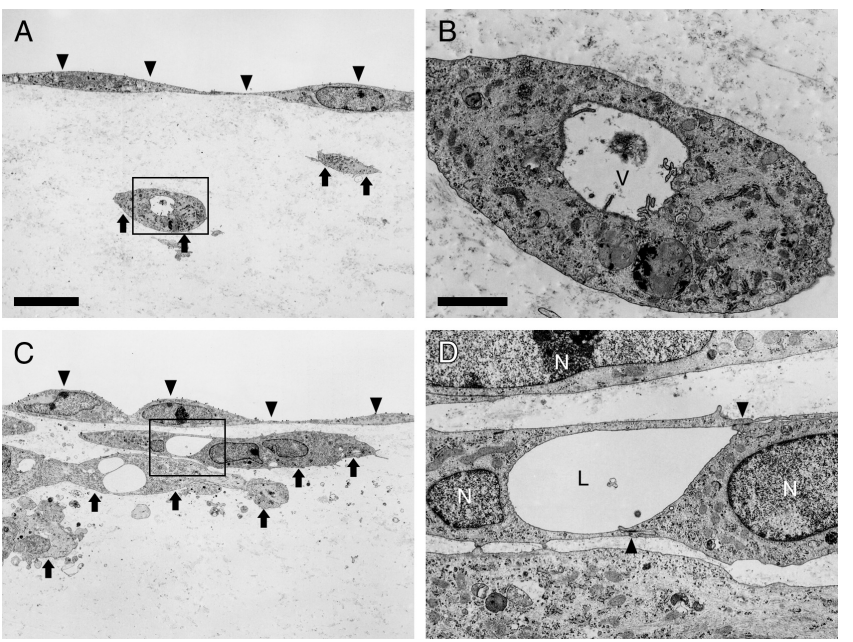

Figure 6. Transmission electron micrographs of vertical sections of 3D networks formed in flexible (A, B) and rigid (C, D) gels. A: Arrowheads indicate cell monolayers on the gel surface. Cells invaded flexible gels independently (arrows). B: Enlarged image of the area indicated by a box in A. A vacuole (V) is formed within a single cell. C: Arrowheads indicate cell monolayers on the gel surface. Cells invaded into rigid gels as clumps (arrows). D: Enlarged image of the area indicated by a box in C. Adjacent cells form a lumen (L), which is confirmed by the junctional complexes between the cells (arrowheads). V: vacuole; L: lumen; N: nucleus. The sections were examined at 80 kV. A and C, and B and D were taken at the same respective magnifications. Scale bars, 10 µm (A) and 2 µm (B).

3.4 Cross sections of network structures

We also examined the fine structure of the vertical sections using transmission electron microscopy (Fig. 6). In the flexible gel, lumens were not observed, although some sprouting cells did have intracellular vacuoles (Fig. 6A, B). In contrast, in the rigid gel, the lumen was delimited by adjacent cells (Fig. 6C, D). These cells constructed junctional complexes to form the lumen (arrowheads, Fig. 6D). These results are consistent with the observations from serial sections.

4 Discussion

Effects of mechanical properties of substrates on 3D network structure

Collagen gels that polymerized at pH 5 and 9 were used as flexible and rigid gels, respectively. Time-lapse microscopy revealed that the process of network formation differed in the two types of gel: in the flexible gel, the cells invaded into the gel more frequently and formed relatively thin networks. The network structures were then developed by the connection of sprouting cells. The density of the networks was 2.6 times greater in the flexible gel than in the rigid gel. In contrast, in the rigid gel, cell aggregates were first formed beneath the gel surface. Relatively thick protrusions then elongated from the aggregates and developed into branching networks. The characteristic filamentous cytoplasmic processes were observed at the tips of the networks formed in the rigid gel, whereas few were formed in the flexible gel. These results indicate that the elasticity of the collagen gels affects cellular migration and the subsequent formation of capillary-like networks.

The mechanical properties of collagen gels also affected the network thickness and the lumen-type structures of the capillary-like networks. In the flexible gel, most cells invaded the gel individually and formed thin networks. Small vacuoles were formed within each cell forming the networks. In the rigid gel, sprouting cells formed thick networks with lumens delimited by multiple cells. These results are consistent with previous results in which the mechanical properties of the collagen gel were controlled by attaching the gel to a solid surface [13]. Compared to a floating gel, an attached gel is less deformable because of the constraint of the rigid interface, and Sieminski et al. [13] demonstrated that ECs exhibit different network formation behaviors in constrained and floating gels. In the rigid, constrained gel, ECs formed thicker networks with larger lumens than in the floating gel.

Vernon et al. [14] also investigated the formation of EC networks in 3D substrates by observing sprout formation from aggregated cells embedded within collagen gels. In their experiment, the collagen concentration was varied from 0.2 to 2.0 mg/ml; presumably, gel rigidity also varied with the collagen concentration. The sprouts formed in the more flexible gels (0.2 mg/ml collagen) were extensive, whereas those formed in the more rigid gels (2.0 mg/ml collagen) were less

extensive. This tendency is consistent with our results from time-lapse microscopy in which we found that BPMECs formed extensive networks in the flexible gel, whereas they formed aggregates in the rigid gel. In the previous study, however, the 3D configuration and branching characteristics of the network structures were very different at different collagen concentrations [14], suggesting that the concentration of collagen also has a direct effect on network formation by ECs. In our model system, we investigated the effects of substrate elasticity without changing the concentration of ECM protein.

We further investigated network structures with respect to their 3D configuration. Networks expanded more deeply into the gel in the rigid gel than in the flexible gel. Although a few cells reached a depth of about 100 μm in the flexible gel, they appeared to have invaded the gel independently and did not form part of a network. In contrast, in the rigid gel, the ECs formed thick interconnected networks that reached a depth of about 100 μm at their tips. Quantitative 3D analysis confirmed that the relationship between the relative network areas formed in flexible vs. rigid gels changed at a depth of around 30 μm. Significantly larger networks were formed in the deep region of the rigid gel than in the deep region of the flexible gel. These results demonstrate that the mechanical properties of the ECM significantly affect the 3D configuration of the resulting network structures.

To control the 3D configuration of networks, the balance between migratory activity and morphogenic properties may be important. As shown by scanning electron microscopy (Fig. 2), the flexible gel was composed of relatively thick fibrils, suggesting that the gel was more porous than the rigid gel because both flexible and rigid gels contained the same amount of collagen. The porous flexible gel probably facilitated the migratory activity of BPMECs. This higher migratory activity was confirmed by phase-contrast, time-lapse microscopy. BPMECs invaded the flexible gel more frequently than the rigid gel (Figs. 4A, B). Thus, the balance shifted toward migratory activity at the expense of morphogenic properties. The higher migratory activity induced dissociated migration in the flexible gel. The cells invaded the gel independently and formed thin networks. The cells tended to form networks beneath the cell monolayers because it was difficult to form continuous networks reaching deeper regions because of the dissociated migration. Therefore, the networks formed in the flexible gel were dominantly distributed at depths of <30 μm.

In contrast, in the rigid gel, the balance shifted toward morphogenic properties at the expense of migratory activity. The rigid gel was composed of relatively thin fibrils, suggesting that the gel was less porous than the flexible gel. BPMECs may need more ECM-degrading activity to penetrate the rigid gel, which may contribute to the decreased migratory activity. Migratory activity may also be inhibited by the viscoelastic resistance of the rigid gel. Thus, the less porous rigid gel decreased the migratory activity of BPMECs. This lower migratory activity induced cell aggregates in the rigid gel. The cells then gradually migrated into the gel and formed aggregates (Figs. 3C and 4D). To develop into networks, the cells extended

filamentous cytoplasmic processes because their migratory activity was inhibited (Figs. 3D and 4E). These cytoplasmic processes may be important for developing networks in the rigid gel because the processes dynamically changed their morphology during network growth. Similar cytoplasmic processes are also formed by ECs at the tips of sprouts in the process of angiogenesis in vivo [15]. The cytoplasmic processes may play a role in the anastomosis of angiogenic sprouts. In vivo, migratory ECs at the tips of adjacent sprouts extend filamentous cytoplasmic processes and link with each other. The anastomosis of networks is initiated by the formation of cytoplasmic bridges. Although the speed of network growth was lower in the rigid gel than in the flexible gel, the networks in the rigid gel grew gradually by extending filamentous cytoplasmic processes; the resulting networks were thick and continuous and penetrated deeper than those in the flexible gel.

Acknowledgments

This work was supported by Grant-in-Aid for Scientific Research on Priority Areas 15086202 from the Ministry of Education, Cultures, Sports, Science and Technology of Japan, the 21st Century Center of Excellence for "System Design: Paradigm Shift from Intelligence to Life", and Keio University Special Grant-in-Aid for Innovative Collaborative Research Projects.

References

1. Griffith, L.G., Naughton, G., 2002. Tissue engineering--current challenges and expanding opportunities. Science 295, 1009-1014.
2. Jain, R.K., Au, P., Tam, J., Duda, D.G., Fukumura, D., 2005. Engineering vascularized tissue. Nat. Biotechnol. 23, 821-823.
3. Ingber, D.E., 2002. Mechanical signaling and the cellular response to extracellular matrix in angiogenesis and cardiovascular physiology. Circ. Res. 91, 877-887.
4. Geiger, B., Bershadsky, A., 2002. Exploring the neighborhood: adhesion-coupled cell mechanosensors. Cell 110, 139-142.
5. Pelham, R.J., Wang, Y., 1997. Cell locomotion and focal adhesions are regulated by substrate flexibility. Proc. Natl. Acad. Sci. USA 94, 13661-13665.
6. Wang, H.B., Dembo, M., Wang, Y.L., 2000. Substrate flexibility regulates growth and apoptosis of normal but not transformed cells. Am. J. Physiol. Cell Physiol. 279, C1345-1350.
7. Deroanne, C.F., Lapiere, C.M., Nusgens, B.V., 2001. In vitro tubulogenesis of endothelial cells by relaxation of the coupling extracellular matrix-cytoskeleton. Cardiovasc. Res. 49, 647-658.

8. Breier, G., Risau, W., 1996. The role of vascular endothelial growth factor in blood vessel formation. Trends Cell Biol. 6, 454-456.
9. Yamamura, N., Sudo, R., Ikeda, M., Tanishita, K., 2007. Effects of the mechanical properties of collagen gel on the in vitro formation of microvessel networks by endothelial cells. Tissue Eng., in press.
10. Christiansen, D.L., Huang, E.K., Silver, F.H., 2000. Assembly of type I collagen: fusion of fibril subunits and the influence of fibril diameter on mechanical properties. Matrix Biol. 19, 409-420.
11. Ueda, A., Koga, M., Ikeda, M., Kudo, S., Tanishita, K., 2004. Effect of shear stress on microvessel network formation of endothelial cells with in vitro three-dimensional model. Am. J. Physiol. Heart Circ. Physiol. 287, H994-H1002.
12. Montesano, R., Vassalli, J.D., Baird, A., Guillemin, R., Orci. L., 1986. Basic fibroblast growth factor induces angiogenesis in vitro. Proc. Natl. Acad. Sci. USA 83, 7297-7301.
13. Galbraith, C.G., Sheetz, M.P., 1998. Forces on adhesive contacts affect cell function. Curr. Opin. Cell Biol. 10, 566-571.
14. Huang, S., Ingber, D.E., 2005. Cell tension, matrix mechanics, and cancer development. Cancer Cell. 8, 175-176.
15. Engler, A.J., Sen, S., Sweeney, H.L., Discher, D.E., 2006. Matrix elasticity directs stem cell lineage specification. Cell 126, 677-689.

DEPTH-DEPENDENT COMPRESSIVE BEHAVIORS OF ARTICULAR CARTILAGE AND CHONDROCYTES

T. MURAKAMI, N. SAKAI, Y. SAWAE, M. OKAMOTO, I. ISHIKAWA, N. HOSODA AND E. SUZUKI

Department of Intelligent Machinery and Systems, Kyushu University, 744 Motooka, Nishi-ku, Fukuoka 819-0395 Japan
E-mail: tmura@mech.kyushu-u.ac.jp

The natural synovial joints have excellent performance of long durability with low friction even under high load. To study metabolic mechanism in articular cartilage containing chondrocytes, it is important to know the actual structure and stress-strain state of the cartilage and extracellular matrix around chondrocytes during cartilage deformation, where chondrocytes seem to experience similar deformation to extracellular matrix. The articular cartilage of high water content has a biphasic viscoelastic property and shows the time-dependent and depth-dependent deformation behavior. In this study, the morphology of chondrocyte was visualized, and the compressive behaviors in articular cartilage containing chondrocytes were observed in the compressive apparatus located in the stage of confocal laser scanning microscope. The time-dependent and depth-dependent behaviors of articular cartilage were evaluated by the finite element method for biphasic model.

1 Introduction

With progress of population of aged people particularly in Japan, the increase of disabled persons with inferior walking ability due to osteoarthritis, rheumatoid arthritis or damages of natural synovial joints is anticipated. The initiation of osteoarthritis is considered to be brought about by the deficiency of lubricating ability in synovial joints. The natural synovial joints have excellent tribological performance known as very low friction and very low wear for various daily activities in human life. To maintain the excellent performance, the adaptive multimode lubrication mechanism is likely to operate under various activities in which the elastohydrodynamic lubrication, weeping, adsorbed film and/or gel film lubrication can become effective depending on the severity of operating conditions [1, 2]. However, in natural joints subjected to severe loading and rubbing, the local direct contact between rubbing cartilage surfaces occurs, and then the adsorbed film is removed and the underlying gel layer also is damaged. It is important to repair the damaged surface layer by not only synovial fluid containing phospholipids, proteins, hyaluronic acid etc. but also the supply of proteoglycan from extracellular matrix produced by chondrocytes [3-5]. For supply of proteoglycan to surface gel film, the chondrocytes in surface zone appear to play an important role. The chondrocyte and articular cartilage adapt to changing mechanical environments, but the detailed adaptive and/or restorative process has not yet been clarified. Furthermore, for tissue-engineered cartilage, the appropriate mechanical stimulation is expected to enhance the matabolic activity of chondrocytes.

To study such mechanism involved, it is important to know the structure and stress-strain state of the cartilage and extracellular matrix around chondrocytes during cartilage deformation, where chondrocytes seem to experience similar deformation to extracellular matrix. The articular cartilage has a biphasic viscoelastic property based on a high water content up to 80%. In this study, therefore, the time-dependent deformation of compressed articular cartilage was observed under unconfined compression in the compressive apparatus located in the stage of confocal laser scanning microscope (CLSM) [4,5]. The stained chondrocytes were used as markers to evaluate the local strain of articular cartilage. The variation in depth direction and time-dependent strain behaviors were evaluated.

For these compressive tests, the finite element method (FEM) for biphasic model was applied to evaluate the time-dependent and depth-dependent mechanical behaviors of articular cartilage. The influence of difference of Young's modulus in the depth-direction for cartilage on the deformation was examined.

2 Materials and Methods

2.1 Visualization of chondrocytes and compression tests of articular cartilage in confocal laser scanning microscope

The articular cartilage specimens are prepared from the intact femoral condyle of porcine knee joint. The cylindrical specimen of 3 mm diameter was prepared by the punch. Then, the cylinder was sectioned as half size with a scalpel. The semi-cylindrical specimen includes the subchondral bone of about 0.5 mm thickness. Next, we observed the morphology of chondrocytes, cytoskeleton such as microfilament, intermediate filament and microtubule, and integrin ($\alpha 2$, $\beta 1$) in the cartilage specimen by the CLSM. The cartilage specimens were arranged in either direction perpendicular to the surface (Fig. 1(a)) or as cross-section (Fig. 1(b)). The staining of living chondrocyte in observation of whole morphology and in compression tests was treated with calcein-AM, at 1 μl/ml and 37°C for 30 min. The microfilament, intermediate filament and microtubule were visualized with immunostaining method. The cartilage specimens were rinsed in phosphate buffered saline (PBS) for 10 min twice and incubated for 60 to 240 minutes in a 1% BSA(bovine serum albumin)- PBS solution containing the primary antibodies for each group. The primary antibody for microfilament was AlexaFluor568 phalloidin (Molecular Probes), FITC-phalloidin (ALEXIS BIOCHEMICAL) for 4 h, or Rhodamine phalloidin (Molecular Probes) for 60 min. The primary antibodies for the intermediate filament and microtubule were Anti-Vimentin (NeoMakers) and Anti-β-Tubulin (Neo Makers) for 4h, respectively. The integrin $\alpha 2$ and $\beta 1$ were incubated for 4 h with MAB1950 (CHEMICON) and MAB2000(CEMICON), respectively. After incubation with the primary antibody, the samples were washed for 5 min three times in BSA-PBS. These specimens were incubated in a secondary antibody solution (Alexa Flour 488, or AlexaFluor568, Molecular Probes) for one hour at 37°C and subsequently washed with BSA-PBS.

The compression tests of articular cartilage were carried out by means of the newly developed compression apparatus (Fig. 2) [4, 5] with high precision within 0.2 μm for position control, which was allocated on the stage of CLSM. The compression speed can be adjusted from 1 μm/s to 4 mm/s by feed-back control of DC servo-motor. In most of compressive tests, 10 to 15% total compressive strain was applied by moving impermeable alumina ceramic plate at constant speed. The local strain was estimated as the approaching distance divided by the initial distance in perpendicular direction to the surface between corresponding stained chondrocytes. On the basis of these visualized images, the time-dependent and depth-dependent changes in local strain of articular cartilage were evaluated.

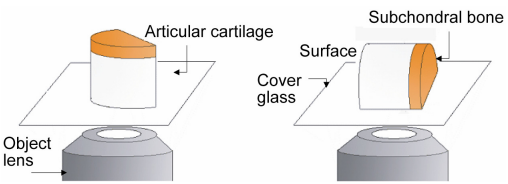

(a) Observation from superficial layer (b) Observation of cross-section

Figure 1. Observation of chondrocytes in cartilage by CLSM.

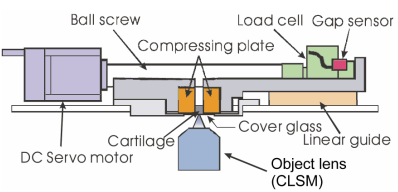

Figure 2. Compressive apparatus on CLSM stage.

2.2 *Finite element analyses for biphasic articular cartilage*

The articular cartilage with high water content is treated as the biphasic model proposed by Mow et al. [6]. Two kinds of FEM analyses were conducted.

(a) Three-dimensional FEM for cylindrical model with uniform elastic modulus

As described in our previous paper [5], to evaluate time-dependent and depth-dependent compression behaviors in articular cartilage, the biphasic FEM analysis [7] was applied for an axisymmetric cylindrical model. The governing equations for linear biphasic model are shown in previous paper [5]. The cylindrical model of 1.5 mm radius and 2.0 mm thickness is composed of tetrahedron elements with 10 nodes (including midpoints), where the bottom plane is fully fixed as the tidemark connected to subchondral bone without fluid flow. The upper surface was uniformly compressed to attain 15% total compression at the constant rate for 10 s and then kept as constant total compressive deflection under unconfined condition for outer cylindrical surface. In this study, the typical values for constituent volume fraction;

solid $\phi^s = 0.17$, fluid $\phi^f = 0.83$, Lame constants; $\lambda = 0.1\text{MPa}$, $\mu = 0.3\text{MPa}$ were used. For the permeability, constant values in horizontal direction of 9.14 x 10^{-15} $m^4/N \cdot s$ were used and the formula proposed by Jurvelin et al. [8] was applied in the compressed direction. The influence of surface conditions on the compressive behavior was evaluated by changing the friction level and permeability.

(b) Two-dimensional FEM for model considering depth-dependent elastic modulus

Furthermore, to examine the depth-dependent strain behavior of articular cartilage, the commercial software of finite element method ABAQUS (v.6.5) was applied for a simplified two-dimensional square model of 3 mm horizontal length and 2 mm thickness. The biphasic pore pressure plane strain elements (CPE8RP: 8-node biquadratic displacement, bilinear pore pressure, reduced integration) of 10 μm x 10 μm square were used. Total number of the elements was 60,000. In this FEM analysis, the void ratio is assumed as 80%. Poisson's ratio of solid phase is 0.125 and permeability is 2.0 x 10^{-15} $m^4/N \cdot s$. The average value of 0.74 MPa or depth-dependent value was used as Young's modulus, as described in 3.2.

3 Results

3.1 Visualization of chondrocytes and compression tests of articular cartilage in confocal laser scanning microscope

In Fig. 3, three-dimensional images of chondrocytes in surface, middle and deep zones in articular cartilage are shown, which were reconstructed by stacks of fluorescent images sliced by CLSM with about 1.5 μm thickness. The chondrocytes have different morphology and sizes depending on their location. Particularly, in the uppermost superficial layer, the chondrocytes are flattened with complicated boundary as shown in Fig. 4. At 50 μm below from the surface, the chondrocytes become elliptical bodies. Therefore, the specified modeling is required for the chondrocytes particularly at the uppermost superficial layer and deep zone.

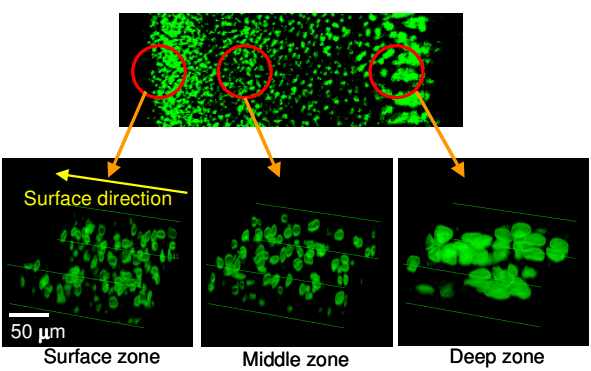

Figure 3. Three-dimensional morphology of chondrocytes constructed from CLSM fluorescent images.

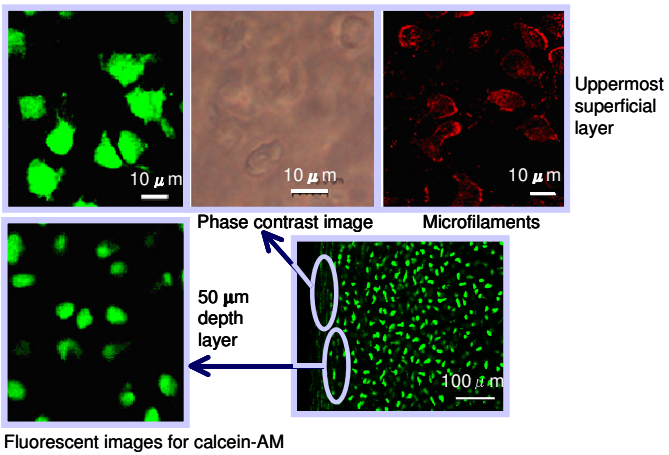

Figure 4. Morphology of chondrocytes at superficial layer.

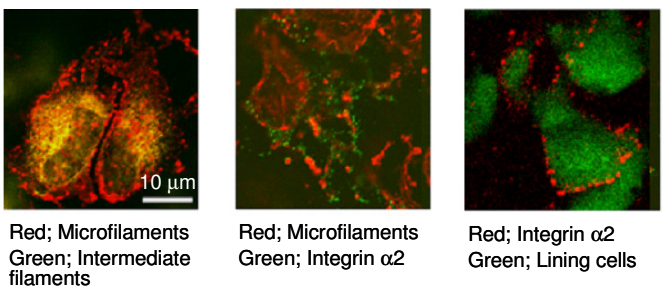

Figure 5. Double stained fluorescent images of cytoskeleton at uppermost superficial layer.

From the observation of images for cytoskeleton in Fig. 5, it was suggested that the microfilaments concentrate along complicated cell boundary through the cell membrane with the integrin and connect extracellular matrix at the uppermost superficial layer. The intermediate filaments exhibit the clear filaments in cytoplasm but the microtubules show unclear fibrous images. The microfilaments and intermediate filaments seem to be connected to nucleus. The elastic modulus of extracellular matrix is 3 orders larger than the cell and the volume fraction of chondrocytes is within 10%. Therefore, the deformation of articular cartilage is considered to be controlled by the structure and property of extracellular matrix composed of type II collagen and proteoglycan. The chondrocytes deforms according to the deformation of surrounding tissue. The cartilage tissue has heterogeneous material properties and the measurement of the local strain is required to understand the actual mechanical stimulating state to the chondrocytes.

The local strain in cartilage specimen in compression tests is estimated by calculating the changes of the distance before and after compression in perpendicular direction to the cartilage surface between the definite stained chondrocytes as reported in the previous paper [4, 5] in Fig. 6 as follows;

Local strain $= (\boldsymbol{a} - \boldsymbol{b}) / \boldsymbol{a}$

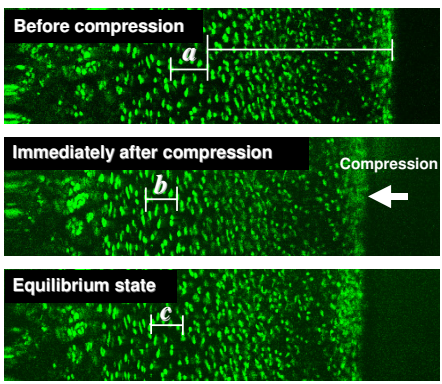

Figure 6. Compression test of articular cartilage.

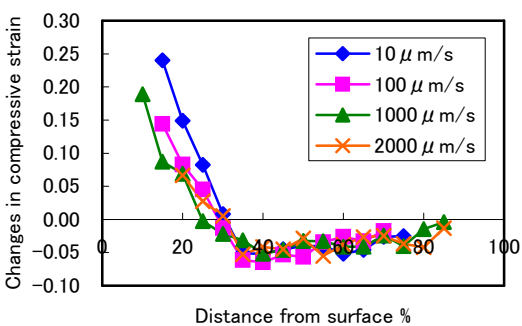

Figure 7. Changes in local strain in articular cartilage at equilibrium during stress relaxation process after compression.

The local strain exhibited not only the depth-dependence but also time-dependence. The changes in local strain at equilibrium during stress relaxation process under constant total compression of 15% (0.15) are shown in Fig. 7. The deformation of deeper zone was clearly recovered probably accompanied with flowing of fluid into the middle and deep zone. On the contrary, the surface zone was largely compressed than average strain during stress relaxation in unconfined compression.

3.2 Finite element analyses for biphasic articular cartilage

In our previous paper [5], the time-dependent and depth-dependent compression behaviors of articular cartilage were evaluated by changing the surface boundary conditions as follows;

Condition 1: Fixed, impermeable, Condition 2: Frictionless, impermeable,
Condition 3: Fixed, permeable, Condition 4: Frictionless, permeable.

In this analysis, the strain in the depth-direction was calculated at the slow speed of 30 μm/s for 10 s to attain 15% (0.15) total strain. Figure 8 shows the distribution in compressive strain at depth-axis at 10 s, when 15% total strain has been attained. Under simplified condition 1 where both upper surface and lower planes are fixed, the middle zone is intensely compressed as larger strain than average level of 0.15, as suggested from the bulging behavior of cylindrical specimen. Under condition 2 which corresponds to healthy cartilage, the constant strain higher than the average is observed at the zone from middle layer to surface. At this low friction surface, the movement or extension of surface region to outer direction is not constrained, and thus the uniform compressive strain appears to be formed at higher level than the average but at lower level than the middle zone under condition 1, as indicated for soft tissues [9]. At the deep zone, there are not large differences among these four kinds of conditions. The strains from middle to surface zones are affected with differences in surface conditions.

Next, time-dependent strain behaviors near surface at 0.1 mm (at 5% depth) from the surface under these surface conditions are shown in Fig. 9. In this analysis for biphasic material of uniform and isotropic properties except permeability, all of the equilibrium strain values under four surface conditions approach asymptotically to the average strain of 0.15, although the time-dependent paths are different. Under condition 1, the strain gradually increases. Under condition 2 for normal intact cartilage, at 10 s the strain attain a little higher value than the average but changes to decrease during stress relaxation process.

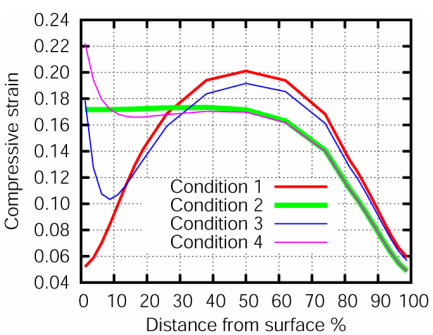

Figure 8. Strain distribution of cartilage at 10 s under four kinds of surface conditions.

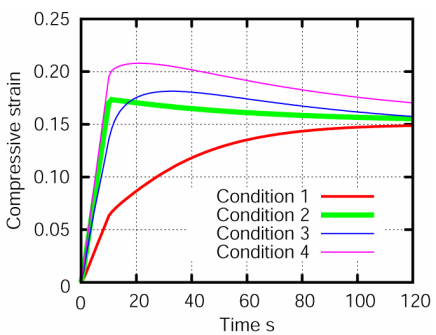

Figure 9. Changes in strain near surface under four kinds of surface conditions.

As shown in Fig. 9, the local strain near surface approaches to the average strain value, because the average elastic modulus was used in this FEM analysis (a). Therefore, it is suggested that the depth-dependency in elastic modulus should be considered in analysis to simulate actual time-dependent and depth-dependent strain behaviors of articular cartilage observed in visualized compression tests.

In this study, two-dimensional biphasic FEM analysis (b) with depth-dependent elastic modulus under the condition 2 for 10% compression for 0.2 s (1 mm/s) was applied to simulate actual strain behavior. The depth-dependency was estimated from the strain distribution at equilibrium (Fig. 10) after stress relaxation in constant total compression test. Estimated Young's modulus is shown in Fig. 11.

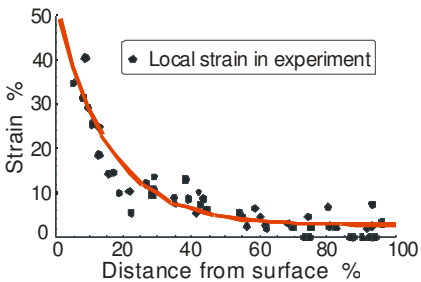

Figure 10. Strain distribution at equiribrium.

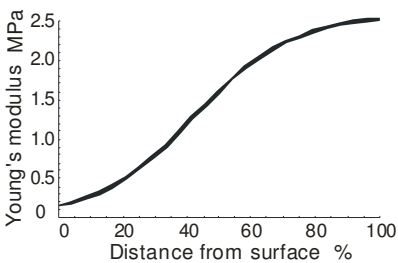

Figure 11. Depth-dependent elastic modulus.

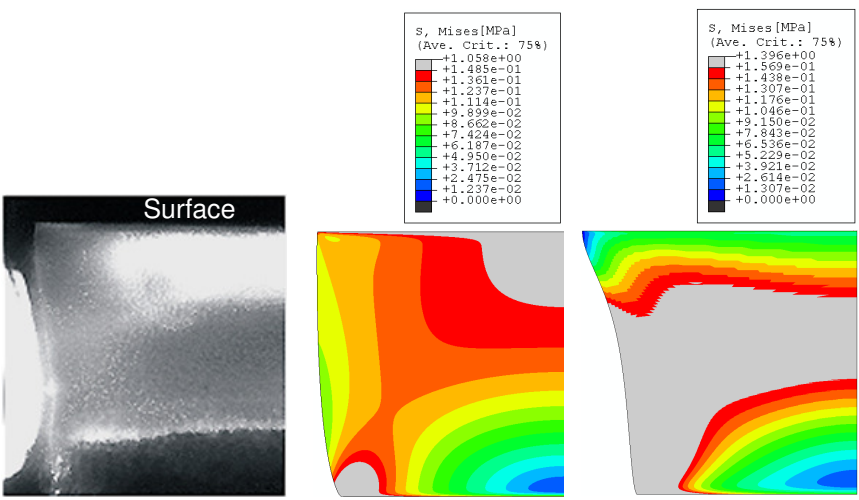

(a) (b) (c)

Figure 12. (a) Profile of compressed specimen immediately after compression, and Mises stress contours and profiles for (b) model with uniform elastic modulus and (c) model with depth-dependent elastic modulus.

It is noticed that the profile of cylindrical surface immediately after compression shown in Fig. 12(a) corresponds to the profile of FEM model with depth-dependent elastic modulus (Fig. 12(c)), while the FEM analysis for model with uniform elastic modulus indicates the different outer profile which is similar to the condition 2 in three-dimensional FEM analysis with uniform elastic modulus (Fig. 8).

The time-dependent strain behaviors at 5% (surface zone) and 50% (middle zone) are shown in Fig. 13. The local strain at surface zone remarkably increases during stress relaxation, while the strain at middle zone recovers to lower strain than average strain as 0.1, similarly to the experimental behaviors in Fig. 7. The higher strain at surface zone gives higher stimulus to chondrocytes at superficial layer.

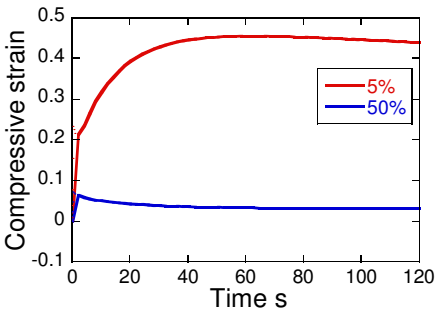

Figure 13. Time-dependent strain behaviors at 5% and 50% depth from the surface in FEM analysis for model with depth-dependent elastic modulus.

4 Discussion

As shown in the fluorescent images of chondrocytes, three-dimensional morphology of chondrocytes depends on their location in cartilage. The cytoskeleton of chondrocyte mainly composed of microfilaments and intermediate filaments appears to be connected to collagen and proteoglycan through the integrin and cell membrane. Most of load seems to be supported by the extracellular matrix composed of type II collagen and negatively charged proteoglycan and thus the chondrocytes deform similarly to the surrounding cartilage tissue. The difference in chondrocyte morphology in surface, middle and deep zones corresponds to the difference in material properties and structure of extracellular matrix.

In compression tests of articular cartilage in the apparatus on the stage of CLSM, the time-dependent and depth-dependent behaviors in the local strain of cartilage could be evaluated by observing the stained chondrocytes as markers. The fluorescent images indicated that the surface zone was largely compressed during stress relaxation, while the cartilage at deeper zone recovered during stress relaxation. Although excessive strain of cartilage and chondrocyte in surface zone at equilibrium is mainly caused by lower elastic modulus after disappearance of fluid pressure after stress relaxation. The importance of depth-dependent elastic

modulus was confirmed in both experimental test and FEM analysis considering the inhomogeneity including the depth-dependent elastic modulus. Wang et al. [10] indicated that large strain of 50% occurs near surface during the ramp loading phase in confined stress-relaxation compression with porous plate at average strain of 10%, although deep zone experiences only low strains less than average strain in the finite deformation biphasic analysis for articular cartilage with depth-dependent aggregate modulus ranging 20-fold difference between the surface and the deep zones. Although we focused the strain behaviors at the present stage, we plan to simulate appropriately the stress behaviors by modification of modeling at the next stage, because the stress values in Fig. 12 do not always correspond to measured values.

The effectiveness of mechanical stimulation was shown for the enhancement of the matabolic activity of chondrocytes in tissue-engineered cartilage. Figures 14 and 15 show the influence of cyclic compressive loading on the tangent modulus and glycoasaminoglycan (GAG) content of chondrocyte-agarose(4%, type IX-A) construct during culture tests, respectively [11]. It was confirmed that the cyclic unconfined compressive stimulation of 15% strain at 1 Hz for 6 h/day was effective in enhancement of tangent modulus and GAG production at 15 days of culture.

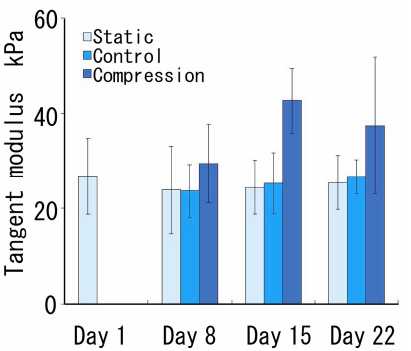

Figure 14. Tangent modulus of chondrocyte-agarose constructs, Error bar:SD, n = 5-7.

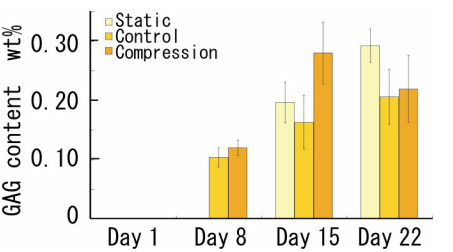

Figure 15. GAG content of chondrocyte-agarose constructs, Error bar:SD, n = 2-8.

5 Conclusions

It was shown that the morphology of chondrocytes was different depending on the location, and the chondrocytes at uppermost superficial layer were flattened with irregular boundary but supported with appropriate cytoskeleton. The visualized compression tests of articular cartilage and corresponding biphasic FEM analyses indicated that the consideration of depth-depending elastic modulus controlled the time-dependent and depth-dependent strain behavior of cartilage.

To evaluate the actual function and mechanotransduction in articular cartilage and chondrocyte, the integrated multi-scale researches at macroscopic tissue level, microscopic cellular level and nanoscopic cytoskeleton/molecular level are required.

Acknowledgments

Financial support was given by the Grant-in-Aid of the Ministry of Education, Culture, Science and Sport (Priority Area, No. 15086212).

References

1. Dowson, D., 1966-67. Modes of Lubrication in Human Joints. Proc. Instn. Mech. Engrs. 181, 45-54.
2. Murakami, T., Higaki, H., Sawae, Y., Ohtsuki, N., Moriyama, S., Nakanishi, Y., 1998. Adaptive multimode lubrication in natural synovial joints and artificial joints. Proc. Instn. Mech. Engrs. 212, 23-35.
3. Murakami, T., Sawae, T., Ihara, M., 2003. The protective mechanism of articular cartilage to severe loading: roles of lubricants, cartilage surface layer, extracellular matrix and chondrocyte. JSME Int. J. 46C, 594-603.
4. Murakami, T., Sakai, N., Sawae, Y., Tanaka, K., Ihara, M., 2004. Influence of Proteoglycan on time-dependent mechanical behaviors of articular cartilage under constant total compressive deformation. JSME Int. J. 47C, 1049-1055.
5. Murakami, T., Sakai, N., Sawae, Y., Kurohara, Y., Ishikawa, I., Okamoto, M., 2006. Time-dependent mechanical behaviors of articular cartilage and chondrocytes under constant total compressive deformation. In: Wada, H. (Ed.), Biomechanics at Micro- and Nanoscale Levels, Vol. II, World Scientific, pp. 37-47.
6. Mow, V.C., Kuei, S.C., Lai, W.M., Armstrong, C.G., 1980. Biphasic creep and stress relaxation of articular cartilage in compression theory and experiment. J. Biomech. Eng. 102, 73-84.
7. Vermilyea, M.E., Spilker, R.L., 1992. A hybrid finite element formulation of the linear biphasic equations for hydrated soft tissue. Int. J. Numer. Meth. Eng. 33, 567-593.
8. Jurvelin, J.S., Buschmann, M.D., Hunziker, E.B., 2003. Mechanical anisotropy of the human knee articular cartilage in compression. Proc. Instn. Mech. Engrs. 217, 215-219.
9. Wu, J.Z., Dong, R.G., Schopper, A.W., 2004. Analysis of effects of friction on the deformation behavior of soft tissues in unconfined compression tests. J. Biomech. 37, 147-155.
10. Wang, C.C-B., Hung, C.T., Mow, V.C., 2001. An analysis of the effects of depth-dependent aggregate modulus on articular cartilage stress-relaxation behavior in compression. J. Biomech. 34, 75-84.
11. Sawae, Y., Honda, J., Suzuki, E., Morita, Y., Watanabe, M., Sanada, T., Murakami, T., 2007. Experimental characterization of regenerated cartilage model cultured under cyclic compression. To be published in Proc. ATEM (Advanced Technology in Experimental Mechanics)'07, JSME-MMD.

II. CELL RESPONSE TO MECHANICAL STIMULATION

This page intentionally left blank

CYTOSKELETAL REASSEMBLING AND CALCIUM SIGNALING RESPONSES TO MECHANICAL PERTURBATION IN OSTEOBLASTIC CELLS

T. ADACHI

Department of Mechanical Engineering and Science, Kyoto University, Yoshida-honmachi, Sakyo, Kyoto 606-8501, Japan
E-mail: adachi@me.kyoto-u.ac.jp

K. SATO

Department of Medical Engineering Science,Yamaguchi University, 2-16-1 Tokiwadai, Ube 755-8611, Japan

M. HOJO

Department of Mechanical Engineering and Science, Kyoto University, Yoshida-honmachi, Sakyo, Kyoto 606-8501, Japan

Y. TOMITA

Department of Mechanical Engineering, Kobe University, 1-1 Rokkodai-cho, Nada, Kobe 657-8501, Japan

In bone functional adaptation by remodeling, it is recognized that bone cells can sense mechanical stimuli and modulate their activities. However, the mechanosensory mechanism by which these cells sense mechanical stimulus and transduce it into intracellular biochemical signals is still not clearly understood. From a viewpoint of cell biomechanics, this study focuses on actin cytoskeleton and cell membrane as functional components in the mechanosensory system. First, intracellular tension in the actin stress fibers was locally released in a single osteoblastic cell, and dynamic reassembling process of the fiber structure was observed using a EGFP-actin. The results indicated that only tension-released stress fibers were selectively disassembled, suggesting that the existence of tension is essential for dynamical stability of the stress fibers. Second, mechanical stimulus was applied to a single cell using a microneedle indentation, and the local strain on the cell membrane at the initiation point of calcium signaling response was measured. The cellular calcium resoponse and membrane deformation were simultaniously observed using multiple fluorescent labeling. These studies suggested that interactions among mechanical and biochemical factors would be key issues to explore the detail mechanism of mechanosensory system in osteoblastic cells.

1 Introduction

Mechanosensing by bone cells, such as osteoblasts and osteocytes, is one of the essential mechanisms of adaptive bone remodeling [1]. Experimental studies have been conducted to clarify the effects of mechanical stimuli on these cellular activities, and demonstrated that bone cells can respond to mechanical stimuli by

increasing their proliferation rate [2] and gene expression levels [3], and by reorganizing their cytoskeletal structure [4]. From these experimental studies, the basic characteristics of the osteoblastic response to mechanical stimuli and its downstream biochemical signaling pathways have been gradually clarified [5]. In most of these experimental studies, however, force and deformation were applied to a population of cells and average cellular response was evaluated to the homogeneous mechanical stimuli [6, 7]. From the viewpoint of cell biomechanics, to understand fundamental mechanosensory mechanism, it is important to study the effect of local mechanical perturbation to cell structural components, such as cytoskeleton and membrane, at which cellular responses are induced.

In this study, first we proposed an experimental system by which intracellular tension in the targeted stress fiber was selectively released in a single osteoblastic cell, and observed the change in stress fiber structure. Focal adhesions that connect the stress fiber to extracellular matrix were locally dissolved to release the targeted adhesion, where tension-released and tension-retained stress fibers coexisted in a single cell, and disassembling process of the targeted stress fibers was observed. Second, we apply a localized deformation to a single cell using a tip of a glass microneedle. The deformation of cell membrane and the change in intracellular calcium ion concentration, $[Ca^{2+}]_i$, were simultaneously observed using a multiple fluorescence labeling and a confocal laser scanning microscope with high spatial and temporal resolutions. From the obtained images, area strain distribution on the cell membrane was analyzed, and its magnitude at the initiation point of cellular calcium signaling was evaluated.

2 Local Disassembly of Actin Stress Fibers Induced by Release of Tension

2.1 Materials and methods

Osteoblastic cells, MC3T3-E1, obtained from RIKEN BioResource Center (BRC) were plated on a $\phi = 35$ mm glass bottom dish (MatTek) at a density of 2.5×10^4 cells/dish, in α-MEM (ICN Biomedicals) containing 10% FBS (ICN). Cells were incubated at 37°C, 5% CO_2 - 95% air atmosphere and 100% humidity. In case of the observation for actin reorganization, after preincubation for 24 hours, EGFP-actin pDNA (Clontec) was transfected into the cells using FuGENE6 transfection reagent (Roche Diagnostics) by the following procedure. During the transfection procedure, the medium was replaced by Opti-MEM (Qiagene) and cells were incubated in the medium containing pDNA and FuGENE6 for 4 hours. Subsequently, the medium was replaced again by α-MEM containing 10% FBS and the cells were incubated additionally for 48 hours for the expression of transfected EGFP-actin pDNA.

In this study, we induced targeted stress fiber contraction by locally dissolving the focal adhesions in a sub-region of a single osteoblastic cell. The stress fiber

structure in osteoblastic cells connects its one end to the extracellular matrix via a focal adhesion complex and its other end to another focal adhesion or the intracellular structures as shown in Fig. 1(a). Therefore, the local release of adherence between focal adhesions and the extracellular matrix induce the selective release of intracellular tension in the targeted stress fiber as shown in Fig. 1(b).

A tip of the micropipette mounted on the microinjection system (IM-88H, Narishige) that was used to dissolve the targeted focal adhesion locally. In the present experimental system, focal adhesion was not fluorescently tagged. We considered focal adhesions locate at the end of stress fibers, and selected area in which targeted focal adhesions assumed to locate. To dissolve the focal adhesions locally, trypsin/EDTA (0.05% / 0.02%) (Sanko Jun-yaku) was squirted onto the targeted focal adhesions using the microinjection system.

The size of the micropipette was approximately of 10 and 6 μm in outer and inner diameters, respectively, so that trypsin/EDTA could be locally squirted to the targeted adhesions in a single osteoblastic cell. The serum contained in the medium is expected to inhibit trypsin activity, so that the dissolving activity of the trypsin was limited within the local area around the micropipette tip, even though trypsin/EDTA diffuses into the surrounding area of the targeted adhesions. Thus, the local contraction was selectively applied to the targeted stress fiber to release the tension in a single osteoblastic cell. Therefore, the coexisting situation of tension-released and tension-retained stress fibers in a single cell could be set up.

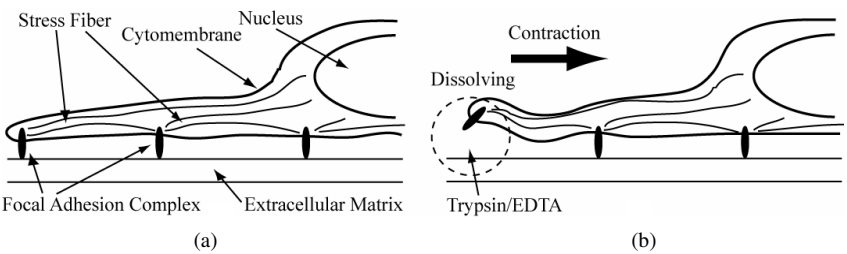

Figure 1. Cytoskeletal actin structure in osteoblastic cell [8]. (a) Actin stress fiber connects its one end to extracellular matrix via focal adhesions. (b) Local dissolving of focal adhesion causes contraction in the stress fibers that connects to the dissolved focal adhesions, due to the release of prestreched tension.

2.2 Results and discussion

Selective disassembly of stress fibers was induced by local contraction of cell body. The change in stress fiber structure induced by the local contraction in a single osteoblastic cell is shown in Fig. 2. In Fig. 2(a), a single osteoblastic cell is located at the center, and the micropipette tip is at the bottom. The dotted circle indicates the targeted area in which focal adhesions were locally dissolved by trypsin/EDTA. Figure 2(b) shows a fluorescent image of the stress fibers labeled by EGFP in the initial state. In this cell with a triangle-like shape, the stress fibers structure mainly

consists of three groups, which connect to the focal adhesions; those are located in the upper corner of the triangle, and at the lower left and right corners. These stress fibers have linear or arc shape, which indicates the intracellular tension in each fiber is in a mechanical equilibrium state to maintain their shape.

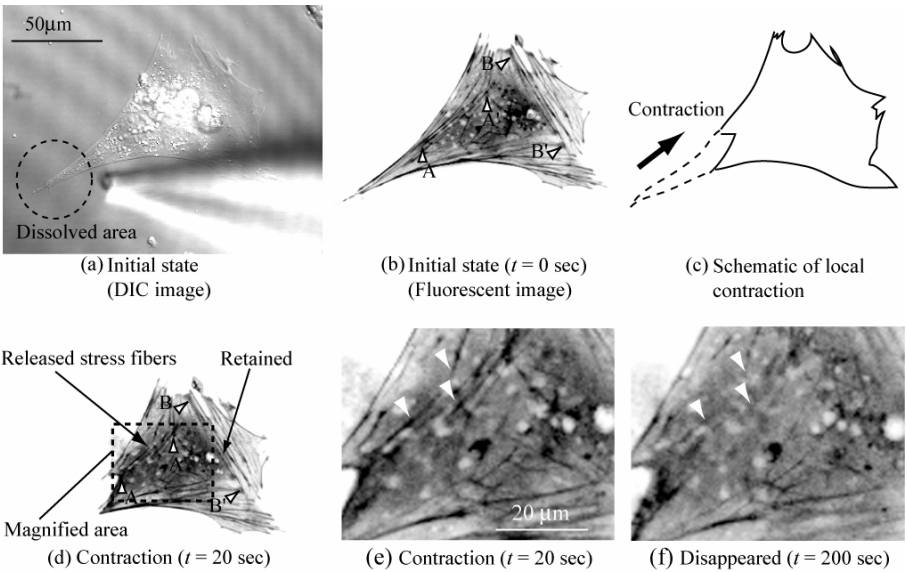

Figure 2. Selective disassembly of tension released stress fibers. (a) DIC image showing cell body and micropipette tip. The focal adhesions in the dotted circle were selectively dissolved. (b) Fluorescent image of actin stress fibers labeled using EGFP, and this image shows the initial state of the stress fiber structure. (c) Schematic that shows the local contraction of the cell. (d) The cell body locally contracted, and the stress fibers which connected to the dissolved focal adhesion (A - A') also contracted. While the stress fibers that do not connect to dissolved adhesions (B - B') did not contract. The area in a dotted box is magnified and represented in (e) and (f). (e) Arrow heads indicate tension-released stress fibers. (f) At t = 200 sec after the initiation of the local contraction, only the tension-released stress fibers changed into the blur structure. On the contrary, the tension-retained stress fibers retained its clear structure (d).

The time at which localized contraction initiated was defined as t = 0 sec. The deformation continued to t = 20 sec, and cell shape changed as illustrated in Fig. 2(c) and shown in Fig. 2(d). This localized contraction induced selective contraction of the fibers which connected to the released focal adhesions as indicated by arrow heads (A - A') in Fig. 2(b). In the contracting process, buckling- or bending-like deformation of the fibers was not observed. Therefore, it was suggested that this contraction of the targeted fiber did not proceed to the compressive state but to the stress-free configuration. On the contrary, contractive deformation was not observed in other fibers connected to the unreleased focal adhesions, for example, as indicated by white arrows (B - B') in Figs. 2(b) and (d).

Figure 2(f) shows the stress fiber structure at t = 200 sec. The outlines of the cell shape were almost same as that in Fig. 2(e), suggesting that the focal adhesions that were not in the targeted area kept their adherence, and that the fibers connected to the unreleased focal adhesion did not show contraction. In these unreleased stress fibers, the structure could be clearly observed and the fibers seemed to keep their structure. Contrary to this, in the tension-released stress fiber (A -A') as shown in Fig. 2(b), the structure turned into a blur. To show the change of the tension-released stress fibers structure from t = 20 to 200 sec clearly, the magnified images are shown in Figs. 2(e) and (f), where the area in a dotted box in Fig. 2(d) is magnified. Figure 2(e) shows the state approximately after the tension release (t = 20 sec), and Fig. 2(f) shows the state after the fibers disappeared (t = 200 sec). Although the fibers indicated by arrows have clear structures at t = 20 sec (Fig. 2(e)), the fiber structure changes into a blur structure or disappears at t = 200 sec (Fig. 2(f)).

In previous studies, some researchers have reported that the application of mechanical stimulus induces reorganization of stress fibers. In these experimental systems, deformation or force as a mechanical stimulus was applied to the whole cell body via deformation of elastic substrate on which cells adhere [2, 9, 10]. Thus, it is difficult to directly demonstrate the relationship between the mechanical condition of individual stress fibers and fiber reorganization. Therefore, in the present study, we set up a coexisting situation of tension-released and tension-retained stress fibers in a single osteoblastic cell, and the change in the stress fiber structure after the application of contraction was observed. As a result, only tension-released stress fibers were selectively disassembled. This result directly suggests that the existence of tension in the stress fiber is crucial for the dynamic stability of the fiber structure.

In the disassembling process of the stress fiber, various biochemical factors play important roles. It is probably not appropriate to consider that tension in the stress fiber directly affects the activities of such biochemical modulators. It may be reasonable to assume that the tension in the stress fiber affects the conformation of molecules. In our speculative hypothesis, the secondary structure or higher structure of the peptide chain in the stress fiber is mechanically stabilized under the existence of tension force. In addition, the tension release may cause an increase in the degrees of freedom of the stress fiber, and consequently this increase brings about the change in affinity between actin molecules and actin modulating proteins, which directly associate with actins. Based on this hypothesis, we believe tension existing in stress fibers is important to maintain stability of the stress fiber structure.

The result in this study, the tension release in the stress fiber induces the disassembly of the fiber, gives us a hypothetical explanation for the mechanical stimulus-induced actin reorganization phenomenon. The actin reorganization mechanism might consist of two phases, the actin disassembling and assembling phases. In this study, we observed the disassembling phase of the fiber, while we did not observe the assembling phase which probably follows the disassembling phase. Further study has to be conducted to evaluate the effect of tension on the individual assembling and disassembling processes of the stress fiber structures.

3 Measurement of Local Strain on Cell Membrane at Initiation Point of Calcium Signaling Response to Applied Mechanical Stimulus

3.1 Materials and methods

Osteoblastic cells, MC3T3-E1, were plated at a density of 7.0×10^4 cells on a glass bottom culture dish (ϕ = 35 mm). The cells were cultured in α-MEM containing 10% FBS, and maintained in a 95% air - 5% CO_2 humidified environment at 37°C. After 24 hours of preincubation, the cells were used in the experiment.

After preincubation, the cell membrane and intracellular calcium ions were labeled using fluorescent dyes. Firstly, the cell membrane was labeled by incubating cells in Opti-MEM (Invitrogen) containing 5 μM Vybrant DiI (Molecular Probes) for 4 min at 37°C. Secondly, after rinsing 3 times with PBS (Wako Pure Chemical Industries), calcium ions were labeled by incubating cells in Opti-MEM containing 6 μM Fluo 3-AM (Dojindo) for 20 min at 25°C. Finally, after the PBS rinsing, the medium was replaced with α-MEM for observation. Fluorescence images were obtained using a confocal laser scanning microscope (LSM 510, Carl Zeiss) with a 100× oil immersion objective lens. All images were recorded on a PC as intensity data at an 8-bit resolution and a spatial resolution of 0.18 μm/pixel. Depending on the velocity of the microneedle, the observed rectangle area was reduced to obtain images with a time resolution as high as possible. The observed rectangle areas were 72.0×23.4 μm (400×130 pixels) in the case of low microneedle velocities of 1 and 10 μm/sec, and 36.0×13.5 μm (200×75 pixels) in the case of high velocities of 20, 30, 40 and 50 μm/sec. Thus, the time intervals for obtaining sequential images were 0.126 and 0.069 sec/image for the low and high velocities, respectively.

To apply localized deformation as a mechanical stimulus to a single cell, we perturbed a cell membrane using a glass microneedle with a 2 μm tip diameter [11]. The microneedle was formed using a micropipette puller (PC-10, Narishige), and the tip of the microneedle was heat-polished to make it smooth and round using a microforge (MF-900, Narishige). The microneedle was mounted on a three-dimensional micromanipulator (ONW135, Narishige) using an attachment with a linear slider and a piezoelectoric actuator as shown in Fig. 3(a).

In this study, the deformation as the mechanical stimulus was applied to a cell by two successive processes as schematically represented in Fig. 3(b). First, the microneedle was moved vertically downward to indent the tip onto the cell membrane at a height of 2 μm from the dish bottom. After the vertical indentation by the microneedle tip, the microneedle was kept in this position for approximately 10-30 sec to confirm whether there is no cellular response to vertical indentation. Second, as the mechanical stimulus, the microneedle was moved horizontally to apply local deformation to the cell, which is parallel to the dish bottom. The displacement and velocity of the microneedle tip in the horizontal direction, defined

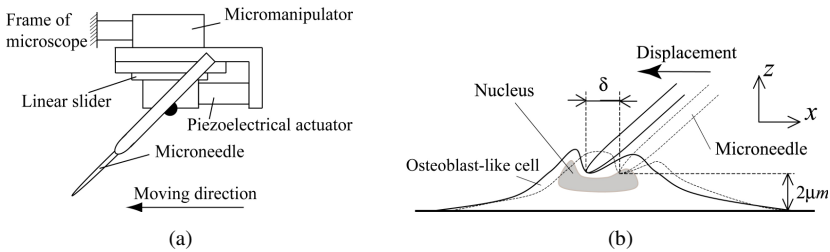

Figure 3. Application of local deformation to a single cell using a glass microneedle [12]. (a) Device for mechanical stimulus application. The displacement and velocity of the microneedle were controlled using a piezoelectric actuator attached to a micromanipulator. (b) Local deformation applied to a single cell. The glass microneedle was indented vertically onto the cell membrane at a height of 2 μm from the dish bottom. Then, the needle was slid horizontally on the membrane to apply local deformation.

as δ and v, respectively, were controlled using a piezoelectoric actuator; various velocities were used: v = 1, 10, 20, 30, 40 and 50 μm/sec.

Area strain distribution on the cell membrane attributable to the application of local deformation was measured by the following image analysis. Because of the features of the confocal laser scanning microscope, all images were obtained from a 6-μm-thick fixed focal plane; the images were two-dimensional projections from the top view. Therefore, strain analysis was also conducted using a two-dimensional projected image. First, a displacement field in the observed region was measured by the image correlation method between obtained time sequence images using image processing software (Flow-vec 32, Library). Second, grid points at 10 pixel intervals were set on the observed region, and triangle finite elements were formed by closing each grid point, while considering them as nodal points. To obtain the large displacement vector from the initial state to the state at which the cellular response was observed, all of the stepwise displacements measured from each sequential image were summed up. That is, the total area strain of the triangle elements was obtained by integrating the incremental displacement vector of each node. The change in the area of the triangle elements was defined as

$$\varepsilon_A = (A - A_0)/A_0 , \tag{1}$$

where A_0 is the initial area of the triangle and A is the area after the deformation.

3.2 Results and discussion

Figure 4 shows images of cellular response to the applied local deformation. Figure 4(a) shows the entire image of the cell, and the area enclosed in a rectangle is the analyzed area. Figures 4(b), (c) and (d) show the cell membrane labeled by Vybrant DiI, intracellular calcium ions labeled by Fluo 3, and the transmitted image of the glass microneedle tip, respectively. In these figures, the time immediately before the stimulus application, that is, the horizontal displacement of the microneedle tip, was

defined as $t = 0$ sec. Before $t = 0$ sec, although the microneedle was already indented vertically onto the cell membrane, no change in $[Ca^{2+}]_i$ was observed. At $t = 0$ sec, the microneedle was moved horizontally to apply local deformation to the cell membrane. Then, at $t = 1.26$ sec, the microneedle tip was moved at a constant velocity to the left at $\delta = 8.3$ μm, as shown in Fig. 4(b). At this point, no change in $[Ca^{2+}]_i$ was observed. At $t = 1.51$ sec and $\delta = 9.7$ μm, a local increase in the fluorescence intensity of Fluo 3 was observed at the front of microneedle tip, as shown in Fig. 4(c). This localized increase in fluorescence intensity could be considered as the initiation of intracellular calcium signaling response to the applied deformation. Subsequently, a local increase in fluorescence intensity of Fluo 3 propagated into the entire cell body at $t = 2.77$ sec and $\delta = 10.7$ μm.

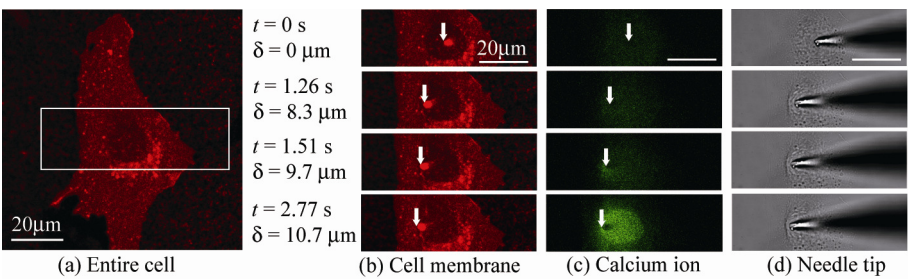

Figure 4. Deformation of the cell membrane and the cellular calcium response [12]. (a) Image of entire cell. (b) Magnified images of the cell membrane, (c) intracellular calcium ion concentration, $[Ca^{2+}]_i$, and (d) transmitted images of the microneedle, respectively. The magnified area is indicated as a rectangle in (a). The arrows in (b) and (c) indicate the position of the needle tip. A localized increase in $[Ca^{2+}]_i$ was observed at the front region of the needle tip at $t = 1.51$ sec ($\delta = 9.7$ μm).

To evaluate the relationship between the deformation of cell membrane and the initiation of calcium signaling response, fluorescence images of the cell membrane and contour images of $[Ca^{2+}]_i$ were analyzed, as shown in Fig. 5(a). In this figure, the upper row shows the images of the cell membrane labeled by Vybrant DiI, the middle shows the contour images of $[Ca^{2+}]_i$ labeled by Fluo 3, and the lower shows the line profiles of the fluorescence intensity of Fluo 3 corresponding to the line indicated in the middle row, and arrows indicate the position of the microneedle tip.

The distribution of the area strain ε_A on the cell membrane and the contour image of Fluo 3 at the initiation time point of calcium signaling are shown in Fig. 5(c). In this figure, the arrow indicates the position of the microneedle tip, and "×" indicates the position of the initiation point of calcium signaling. In this case, at point ×, the area strain was evaluated as $\varepsilon_A = -0.57$, which was a compressive strain from the two-dimensional projected image. The average area strain evaluated in a number of cells was $\varepsilon_A = -0.57 \pm 0.14$ (mean ± S.D., $n = 20$).

Figure 6 shows the relationship between displacement velocity of microneedle and area strain magnitude at the initiation point of calcium signaling response. At a low velocity between v = 1 μm/sec and v = 10 μm/sec, there was no significant difference in area strain magnitude. In contrast, at a high velocity (v = 10 - 50 μm/sec) there was a significantly smaller area strain magnitude; that is, the cells responded more sensitively to the mechanical stimulus at a higher velocity.

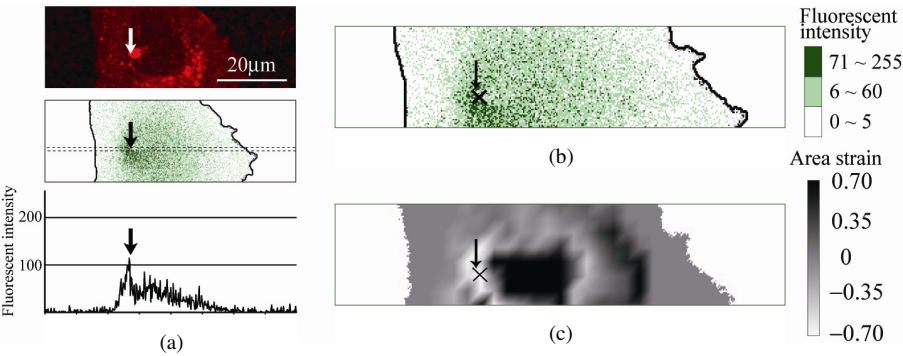

Figure 5. Strain distibution at the initiation point of calcium resoponse at t = 1.51 sec (δ = 9.7 μm) [12]. (a) The upper row shows cell membrane labeled with Vybrant DiI, the middle shows the contour images of $[Ca^{2+}]_i$ labeled with Fluo 3, and the lower shows the line profile of fluorescence intensity of Fluo 3 on the dotted line indicated in the middle., local increase in fluorescence intensity was observed at a region adjacent to the microneedle tip. (b) The magnified image of the middle of (a). (c) The strain distribution and the initiation point of calcium signaling response. In these images, arrows indicate the position of the microneedle tip, and "×" indicates the initiation point of local increase in $[Ca^{2+}]_i$.

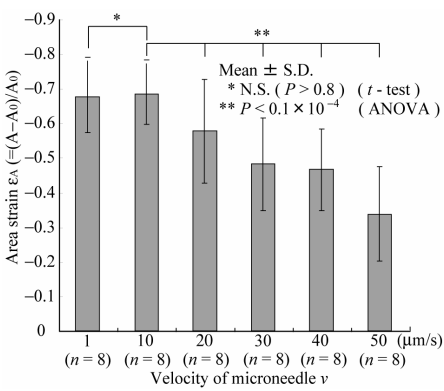

Figure 6. The strain magnitude at the initiation point of calcium signaling response depends on the displacement velocity of the microneedle [12]. At a low microneedle velocity, there was no significant difference in strain magnitude between v = 1 μm/sec and v = 10 μm/sec. In contrast, at a higher velocity, the cells responded with a smaller strain magnitude.

A novel point of the present study is that we quantitatively evaluated the local area strain of cell membrane at the initiation point of cellular calcium response to the local perturbation. Evaluation of the mechanical condition at the cell structural level is important to clarify the mechanosensory mechanism from a viewpoint of cell biomechanics. Mack *et al*. [13] have reported that the application of local force to a single vascular endothelial cell using magnetic microparticles adhering to the cell membrane induced the translocation of focal adhesions, and it was effected by force amplitude and frequency. This result might also suggest that the viscoelastic properties of cellular structure affect the characteristics of cellular responses.

Possible velocity-dependent mechanism could be proposed. Because of the viscoelastic properties of the cell membrane, cytoskeleton, and other cellular structural components, the apparent strain magnitude that induces the calcium signaling response is observed in a velocity-dependent manner. That is, even though the mechanosensors themselves are not velocity-dependent, the viscoelastic property of the cell structure could modulate the relationship between apparent strain and the actual deformation of mechanosensor immersed in the cell structure.

In this study, a compressive strain was observed at the initiation point of the calcium signaling response. One limitation is that the strain was analyzed in two-dimensionally projected images. In our experimental system, we applied local deformation as a mechanical perturbation by directly indenting a microneedle onto the cell membrane and sliding it horizontally. This caused a very complex three-dimensional deformation of the cell membrane around the microneedle tip, including not only stretching and compression but also bending and shearing. Thus, two-dimensional projected images obtained using a confocal laser scanning microscope might lack complex information. Despite several such limitations, the proposed experimental system and the obtained results using this system in the present study could be considered as the fundamental step to the further understanding of the mechanosensory mechanism of osteoblastic cells.

In the future, the experimental system should be further improved. In addition to the use of the present system, analysis at higher spatial and temporal resolutions, multiple labeling of the cell membrane, cytoskeletal structures and focal adhesions, and three-dimensional observation will be necessary to overcome the above-mentioned limitations. These improvements might provide us further understanding of the local mechanical conditions under which the osteoblastic calcium signaling response to a mechanical stimulus is induced.

Acknowledgments

This work was partially supported by Grant-in-Aid for Scientific Research on Priority Areas, “Biomechanics at Micro- and Nanoscale Levels” (No.15086211) from the Ministry of Education, Culture, Sports, Science and Technology of Japan. Figures 3-6 are partly reprinted from publication [12] with permission from Elsevier.

References

1. Duncan, R.L., Turner, S.H., 1995. Mechanotransduction and the functional response of bone to mechanical strain. Calcif. Tis. Int. 57, 344-358.
2. Buckley, M.J., Banes, A.J., Levin, L.G., Sumpio, B., Sato, M., Jordan, R., Gilbert, J., Link, G.W., Tran Son Tay, R., 1998. Osteoblasts increase their rate of division and align in response to cyclic, mechanical tension in vitro. Bone & Min. 4-3, 225-236.
3. Roelofsen, J., Klein-Nulend, J., Burger, E.H., 1995. Mechanical stimulation by intermittent hydrostatic compression promotes bone-specific gene expression in vitro J. Biomech. 28-12, 1493-1503.
4. Sato, K., Adachi, T., Matsuo, M., Tomita, Y., 2005. Quantitative evaluation of threshold fiber strain that induces reorganization of cytoskeletal actin fiber structure in osteoblastic cells. J. Biomech. 38-9, 1895-1901.
5. Gillespie, P.G., Walker, R.G., 2001. Molecular basis of mechanosensory transduction. Nature 413, 194-202.
6. Jones, D.B., Nolte, H., Scholubbers, J.G., Turner, E., Veltel, D., 1991. Biochemical signal transduction of mechanical strain in osteoblast-like cells. Biomat. 12-2, 101-110.
7. Klein-Nulend, J., Burger, E.H., Semeins, C.M., Raisz, L.G., Pilbeam, C.C., 1997. Pulsating fluid flow stimulates prostaglandin release and inducible prostaglandin G/H synthase mRNA expression in primary mouse bone cells. J. Bone Min. Res. 12-1, 45-51.
8. Sato, K., Adachi, T., Shirai, Y., Saito, N., Tomita, Y., 2006. Local disassembly of actin stress fibers induced by selected release of intracellular tension in osteoblastic cell. J. Biomech. Sci. & Eng. 1-1, 204-214.
9. Wang, H.-C. J., Grood, E.S., Florer, J., Wenstrup, R., 2000. Alignment and proliferation of MC3T3-E1 osteoblasts in microgrooved silicone substrata subjected to cyclic stretching. J. Biomech. 33, 729-735.
10. Costa, K.D., Hucker, W. J., Yin., F.C.-P., 2002. Buckling of actin stress fibers: A new wrinkle in the cytoskeletal tapestry. Cell Motil. & Cytoskel. 52, 266-274.
11. Adachi, T., Sato, K., Tomita, Y., 2003. Directional dependence of osteoblastic calcium response to mechanical stimuli. Biomech. & Model. in Mechanobiol. 2-2, 73-82.
12. Sato, K., Adachi, T., Ueda, D., Hojo, M., Tomita, Y., 2007. Measurement of local strain on cell membrane at initiation point of calcium signaling response to applied mechanical stimulus in osteoblastic cell. J. Biomech. 40-6, 1246-1255.
13. Mack, P.J., Kaazempur-Mofrad, M.R., Karcher, H., Lee, R.T., Kamm, R.D., 2004. Force-induced focal adhesion translocation: effects of force amplitude and frequency. Am. J. Physiol. - Cell Physiol. 287, C954-C962.

EXPERIMENTAL ESTIMATION OF PREEXISTING TENSION IN SINGLE ACTIN STRESS FIBER OF VASCULAR CELLS

S. DEGUCHI*, T. OHASHI AND M. SATO

Department of Bioengineering and Robotics, Tohoku University,
6-6-01 Aoba-yama, Sendai 980-8579, Japan
E-mail: deguchi@mech.okayama-u.ac.jp

**Present: Graduate School of Natural Science and Technology, Okayama University,*
3-1-1 Tsushima-naka, Okayama 700-8530, Japan

Actin stress fibers (SFs) in vascular smooth muscle cells and endothelial cells play a critical role in transmitting intracellular forces between separate focal adhesion sites. However, quantitative studies on the berable tension level for single SFs have not yet appeared. Here, we estimated magnitude of preexisting tension in SFs based on measurements of their preexisting stretching strain and tensile properties. Cultured cells expressing fluorescently-labeled actin were treated with detergents to extract the acin bundles. One end of an individual SF was then dislodged from the substrate by using a microneedle, resulting in a shortening of the SF due to a release of preexisting tension. Tensile tests of the isolated single SFs were conducted with a pair of cantilevers to measure the force required for stretching it up to the original length that corresponds to preexisting tension. The magnitude of the preexisting tension, ~10 nN on average, was comparable in magnitude to previously reported data on the cell traction force generated by living adherent cells at focal adhesion sites to keep cell integrity. The Young's modulus of the isolated SFs was estimated to be ~300–1500 kPa from the tensile tests. These data will be fundamental in considering the intracellular force transmission mechanism in vascular cells.

1 Introduction

Adaptation of vascular smooth muscle cells (SMCs) and endothelial cells (ECs) to mechanical stimuli has been reported in many studies [1, 2]. For instance, when exposed to fluid shear stress, biochemical responses appear in ECs, which align the cells and their actin filaments in the direction of flow. The accurate mechanism of such cellular directional responses remains elusive. It has been proposed and gained increasing attention that the extracellular force loaded onto cell is mechanically transmitted to local intracellular mechano-sensing sites, where the force is converted into a change in affinity between biomolecules [1, 3]. If the force loaded has a vector component, then the resultant intracellular stress distribution would also differ in magnitude depending on the direction of the loading. Hence, unlike uniform diffusion of biochemical substances, it allows the directional cell response.

To elucidate the mechanical pathway, it is critical to understand how cell architecture is constructed from what subcellular components. Here, we focus on SFs as such structural components that developed around the cell bottom. SFs are

composed of actin filaments grouped together with myosin, vinculin, and other actin-binding proteins forming a thick fiber with a diameter of several hundred microns [4]. Importantly, cells drag the substrate surface toward the cell center to keep their structural integrity [4]. Actomyosin contraction-based isomeric tension in SFs is probably responsible for the pull or cell traction [4, 5]. Both ends of an SF are anchored to the stiff substrate (i.e., glass or plastic surface in vitro and the basement membrane in vivo) via the focal adhesions. The distance between the two focal adhesions, each located at each end of SF, does not change in statically cultured condition, thus producing isometric tension. Although the isometric tension would be a critical factor in considering the cell architecture, mechanical properties of SF and magnitude of its tension remain mainly unclear.

In the present study, we estimated preexisting tension in SFs isolated from SMCs and ECs [6–9]. We first investigated preexisting strain of SF after isolated from the cells. Tensile tests of the isolated SFs were then conducted to measure the tension required for keeping the preexisting strain. The Young's modulus was determined taking into account its average diameter obtained from electron microscopy to establish macroscopic and averaged mechanical properties.

2 Measurement of Preexisting Strain of Stress Fiber

2.1 Materials and methods

Vascular SMCs and ECs were cultured in Dulbecco's modified Eagle medium supplemented with 10% fetal bovine serum and 1% each of penicillin and streptomycin. Cells were co-transfected with GFP-actin vector and RFP-FAT vector (a gift from Dr. N. Mochizuki, National Cardiovascular Center, Japan; FAT, an amid acid sequence at C-terminus of focal adhesion kinase) using a liposomal method. For preexisting strain measurement experiment, cells expressing GFP-actin and RFP-FAT were incubated with a buffer A (10 mM imidazole, 100 mM KCl, and 2 mM EGTA) containing 25 μg/ml saponin for 8 min at 37°C to remove intracellular ATP and cations that induce actomyosin contraction. To extract SFs, cells were treated with a low-ionic-strength extraction solution (2.5 mM triethanolamine and 1 μg/ml each of leupeptin and pepstatin in distilled water) for 20–40 min, PBS with 0.05% NP-40 for 5 min, and PBS with 0.05% Triton X-100 for 5 min [4, 8].

To confirm whether SFs carry preexisting tension, we observed shape changes after the extracted SF were detached at one end from the substrate. The dish with the cells expressing the fluorescent proteins was fixed on the stage of an inverted microscope. The cells were washed with a buffer consists of 10 mM imidazole, 100 mM KCl, and 2 mM EGTA. After washing the cells three times with a Ca^{2+}- and Mg^{2+}-free PBS, SFs were extracted according to the method described above. Fluorescence images of both SF and FAT were acquired whenever the extraction solutions were changed. After the extraction, PBS were replaced with the buffer A.

Oxygen-removal reagents (2.3 mg/ml glucose, 0.018mg/ml catalase, and 0.1mg/ml glucose oxidase) were added to reduce photo-bleach. By manipulating a fine glass needle made of a capillary tube, one of the focal adhesions visualized by RFP-FAT was carefully dislodged from the substrate surface. The change in the SF length during the experiments was obtained by image analysis using NIH image software.

2.2 Results and discussion

SFs were extracted from the cells (Fig. 1). To estimate preexisting strain of SFs, changes in SF shape during the chemical treatments were observed. The detergent treatment removed the cell membrane and some cell organelles (Fig. 2). Basal SFs were still attached to the substrate and clearly seen even after the chemical treatments (Figs. 2A and 2B). Superimposition of fluorescence images before and after the treatments showed that some peripheral SFs (Fig. 2C, arrowheads) changed in shape from an inward-curved arch (green color) to a relatively straight line (red color). Similar results showed that when cytoplasmic constituents were flown away, some SFs (Fig. 2D, open arrowheads, green color) cross-linking thick SFs were also removed together with the cell membrane or disappeared probably because they were mechanically severed. The thick SFs meanwhile remained stayed on the substrate because they firmly attached to the substrate and were not severed when cytoplasmic constituents were flown away. Some of such fine and fragile actin bundles were entangled around focal adhesions (Fig. 2D, closed arrows, red color). A number of the thick and originally inward-curved SFs (Figs. 2C and 2D, closed arrowheads) pivoted around the focal adhesion sites located at the ends, whereas the positions of the end focal adhesions remained unchanged (Fig. 2E, schematic drawing showing a typical morphological change). In contrast, originally straight SFs did not change the curvature unless their end focal adhesions were detached (Figs. 2C and 2D, open arrows). After the Triton treatment, the length ratio of after to before was 0.94 ± 0.057 for SMCs (mean ± SD, n = 18 SFs) and 0.93 ± 0.05 for

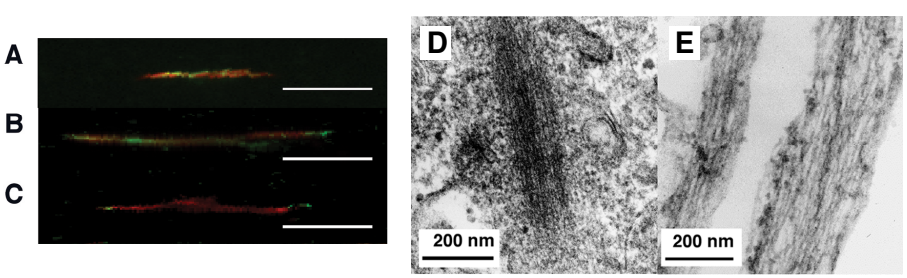

Figure 1. Isolated SFs [8]. (A–C) Double staining patterns of rhodamine phalloidin (red) and FITC monoclonal antibodies (green) against α-actinin (A), smooth muscle myosin heavy chain (B), and vinculin (C). Scale bars = 20 μm. (D and E) Transmission electron micrographs. Longitudinal section of SFs in cell (D) and in vitro (E).

ECs (n = 13 SFs) (Fig. 2E), indicating that the SFs were being stretched in the intact cytoplasm with, on average, 6.4% (= (1 – 0.94) / 0.94 x 100) stretching strain for SMCs and 7.5% strain for ECs.

After detached owing to the needle manipulation, the SFs shrank like a recoil of an elastic material (Figs. 3A and 3B). This shrink is attributable to a sudden release of preexisting tension in the SF as observed similarly in the cell process in previous studies [10]. Assuming that the detached SF finally reached its non-stress state, we examined magnitude of the shortening. The ratio of initial length (before detachment) to non-stress length (after detachment) was 0.83 ± 0.11 for SMCs (n = 30) (Fig. 3C) and 0.82 ± 0.11 for ECs [6]. If we define preexisting strain as ((initial length) - (non-stress length))/(non-stress length), SFs had a preexisting stretching strain of 0.21 for SMCs and 0.24 for ECs on average.

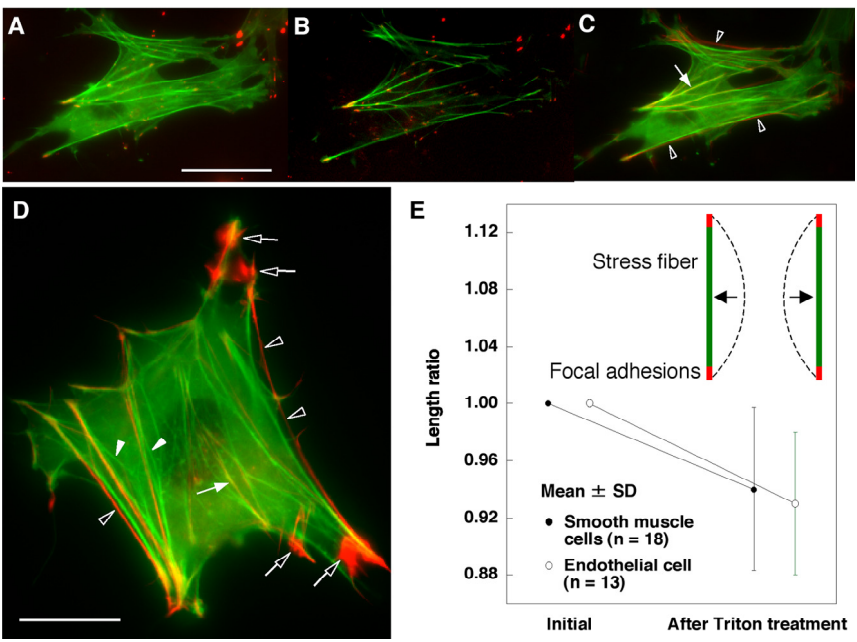

Figure 2. Shortening of SFs after chemical extraction [6]. (A, B) An SMC before (A) and after (B) Triton treatment. GFP-actin and RFP-FAT were pseudocolored green and red, respectively. (C) A superimposed image of GFP-actin images in A (green) and B (red). The pixels show yellow when green and red overlap. Note that thick and originally inward-curved SFs (arrowheads) displaced outward after cytoplasmic constituents were removed. Originally straight SFs (arrow) did not deform. Scale bar = 20 μm. (D) A similar result with C showing superimposition of GFP-actin images of an SMC acquired before (green) and after (red) Triton treatment. Note that some SFs (open arrowheads) were removed after Triton treatment, and thick SFs (closed arrowheads) pivoted outward. The positions of end focal adhesions remained unchanged as shown by yellow color (see text for details). (E) Change in SF length following Triton treatment.

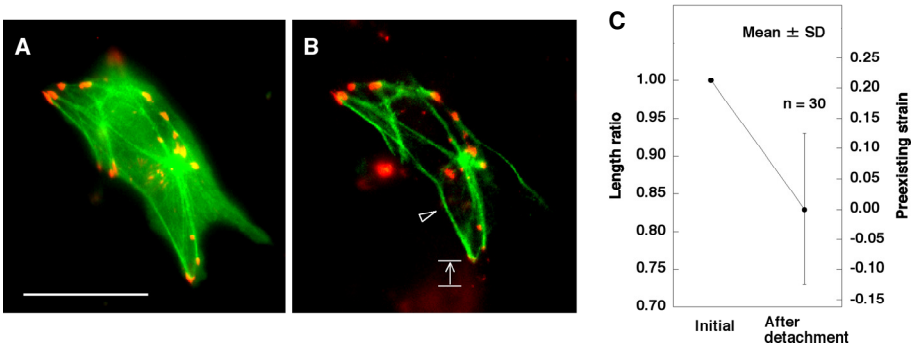

Figure 3. Shortening of SFs after detachment from the substrate [8]. (A, B) A typical example of the cell at intact (A) and after the extraction treatments and the detachment from the substrate (B). The dislodged SF (arrowhead) shortened (arrow). Scale bar = 20 µm. (C) Changes in the SF length. Preexisting strain was calculated from the mean value by dividing the displacement by the zero-stress length.

3 Measurement of Tensile Properties of Stress Fiber

3.1 Materials and methods

A tensile tester was built on an inverted fluorescence microscope (Fig. 4A) [9]. A carbon fiber, 7 µm in diameter and ~600 µm in length, was attached to the tip of a rigid glass rod with epoxy adhesive. This carbon fiber facilitates optical measurement of its displacement. The carbon fiber–glass rod, referred to as cantilever, was used to manipulate individual SFs. A deflectable cantilever, whose spring constant is calibrated before experiment, was placed vertically at one end of the specimen, while a non-deflectable cantilever was placed in parallel at the other end (Fig. 4B); therefore, the latter does not bend against tensile loading. A halogen lamp was used to illuminate the cantilevers. The cantilevers were displaced using piezoelectric ceramic actuators (PZT) connected to each base glass rod. The tip position of the deflectable cantilever was tracked with a photosensing system consists of a circular split photodiode, an I–V converter, and a differential amplifier. A strain gauge, attached to the surface of the PZT, was used to measure the base displacement of the cantilever. To conduct feedback control of strain rate during tensile test, a servo control system was employed (Fig. 4C) in which a reference input having a triangular-shape waveform was used for moving the cantilever as a desired displacement path along which the slope of displacement–time curve is constant; therefore, the moving velocity can be kept constant.

Tensile tests were carried out at room temperature (20°C) using the tensile tester. The tips of both cantilevers were coated with epoxy adhesive prior to test.

The oxygen-removal reagents were administered to reduce photo-bleach. Under illuminations from halogen and mercury light sources, a targeted single SF was lifted up slightly by the cantilevers. Great care was taken not to apply any tension to the specimen before tests. The lifted specimen was kept held for 5 min until the adhesive hardened. Tensile tests were initiated while controlling the position of non-deflectable cantilever with PZT to stretch the specimen at 0.02 s^{-1} strain rate, yielding force–displacement relationship.

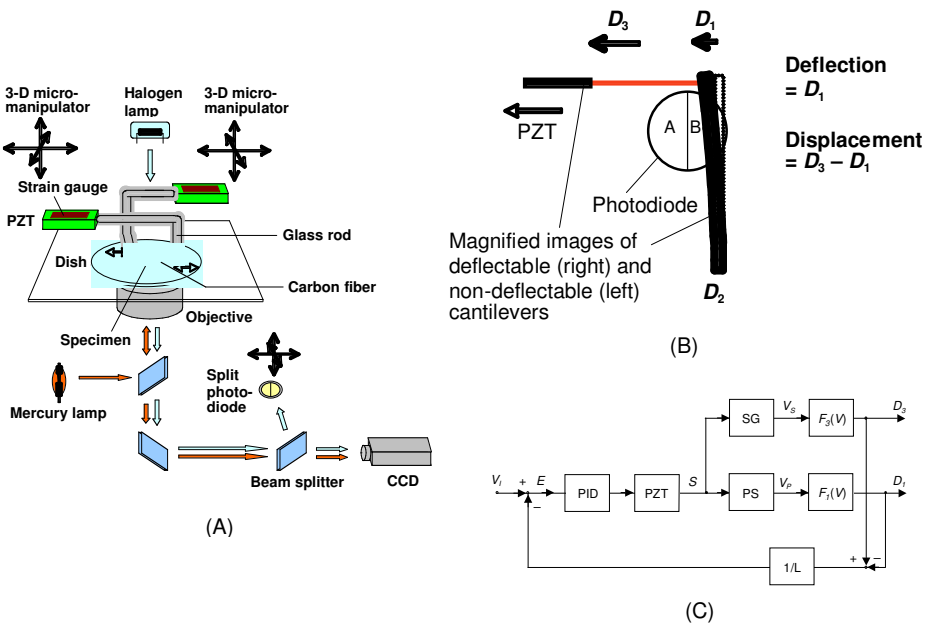

Figure 4. Tensile tester [9]. (A) Schematic drawing of the apparatus. (B) Detection of cantilever position. (C) Servo system for strain rate control. $F_1(V)$, fitting function of photosensing system curve; $F_3(V)$, fitting function of strain gauge system curve; PID, PID controller; PS, photosensing system; SG, Strain gauge system; D_1, displacement of deflectable cantilever tip; D_3, displacement of non-deflectable cantilever tip; E, actuating error signal; L, initial length of the specimen; S, strain of PZT; V_I, triangular waveform input; V_P, photosensing system output; V_S, strain gauge system output.

3.2 Results and discussion

The chemically extracted SFs were scraped off from the substrate before tensile test. The isolated single SFs were stretched in tensile test from the non-stress state up to a strain (defined as the ratio of displacement to initial length) of >1.0 across the preexisting strain level (i.e., ~0.2). The deflectable cantilever was gradually bent since tensile load was given via the specimen (Fig. 5). Force–strain relationship was obtained and averaged in a 0.0–1.0-strain range at a 0.1-strain interval (Fig. 6).

Under higher stretching strains of >0.1, we observed that tensed SFs detached at one end from either of the cantilevers and then rapidly returned to almost their original lengths, indicating that the deformation was elastic. The mean force plots (Fig. 6, circles) were fitted to a quadratic expression by the least-squares method to obtain a regression curve of the force (F)–strain (S) relationship, $F = 20.6\ S^2 + 45.7\ S$ (nN) for SMCs [8] and $F = 12.7\ S^2 + 14.2\ S$ (nN) for ECs [7]. By substituting $S = 0.00$ or $S = 0.237$ (≈ 0.24) into the first derivative dF/dS of the EC curve, we obtained stretching stiffness as 14.2 (nN) at the non-stress state or 20.2 (nN) at the pre-tensed state, respectively. If D (μm) is a diameter of an isolated SF cross-section assumed to be a homogeneous circle, the incremental elastic modulus (E) is calculated as $E = 4 \times dF/dS\ /(\pi D^2)$ (kPa). Hence, if $D = 0.251$ μm (Fig. 7) [7], the elastic modulus is 287 kPa at the non-stress state (that represents the Young's modulus of the SF isolated from ECs) or 408 kPa at the pre-tensed state (Fig. 8). By substituting the average preexisting strain 0.237 for S of the regression curve, preexisting tension in SF of EC was estimated to be 4.08 nN. Similarly, we estimated that the Young's modulus and preexisting tension in the SF of SMCs are 1.45 MPa and 10 nN, respectively [8].

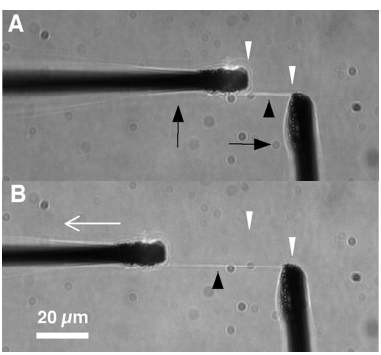

Figure 5. Sequential images of an SF during tensile test [8]. (A) Before stretching of single SF (black arrowhead). (B) During stretching. A white arrow indicates the direction of cantilever (black arrows) displacement.

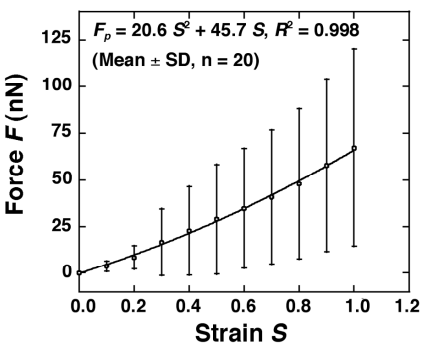

Figure 6. Force–strain relationship of SFs from SMCs in a physiological strain range of 0.0–1.0 [8]. The curve F_p was obtained by least-squares regression for mean plots.

So far as we know, this is the first measurement of mechanical properties of single SFs isolated from living cells. The SFs showed intriguing mechanical properties in vitro, which are different from those of actin filaments. The SFs were capable of large deformation as much as they achieved a maximum length of 3.75-fold of the zero-stress length [8]. There is no report of the breaking strain of actin filaments, whereas their physiological strain reached 0.2–0.42% of the initial length [11]. The breaking force of the SFs was on average 377 nN [8], which was

approximately 600-fold greater than that of untwisted actin filaments, 600 pN [12]. SFs shortened in an ATP independent manner after detached from the substrate, suggesting that the SFs themselves had a preexisting strain. The force required for stretching the single SFs from the zero-stress length back to the original length was ~10 nN, which is comparable in magnitude to the order of living cell traction force [5]. These results suggest that single actin filament is not probably sufficient for bearing the intracellular stresses existing in adherent cells to keep their own integrity [3]. Variations in the composition and the amounts of the subfilaments in single SFs were probably responsible for the data dispersion of force–strain curves since diameters of each specimen were not evaluated in the present study.

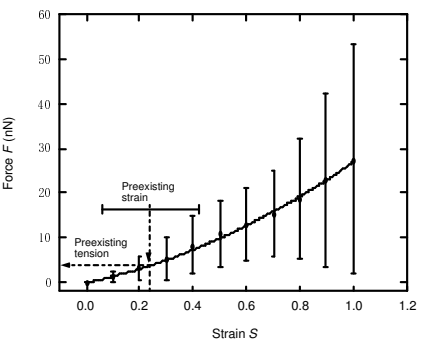

Figure 7. Force–strain relathionship of SFs from ECs [7]. Vertical solid bars indicate standard deviation (n = 6). A horizontal solid bar and a vertical dashed line indicate standard deviation and mean of preexisting strain, respectively. A horizontal dashed arrow indicates an estimated preexisting tension.

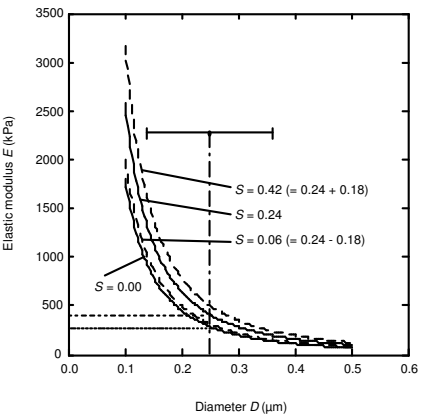

Figure 8. Elastic modulus–diameter relathinship of SFs from ECs [7]. A parameter S indicates strain. A horizontal solid bar indicate standard deviation of SF diameter. Two kinds of horizontal dashed lines indicate each level of incremental elastic modulus corresponding to their strain levels.

The Young's modulus of SFs estimated in this study is comparable in magnitude to previous results obtained from atomic force microscopy [13, 14], in which localized increases in elastic modulus of more than 100 kPa along SFs were detected. The Young's modulus was three orders of magnitude lower than that of synthesized F-actin, 2.6 GPa reported by Gittes et al. [15] or 1.8 GPa by Kojima et al. [16] estimated under similar analytical assumptions of homogeneity. The elastic modulus of SFs at the breaking point (S = 1.99) was also evaluated with another assumption that SFs were incompressible [8]. Strain due to an infinitesimal displacement Δl from the breaking point can be represented as $\Delta l/(L + 1.99L)$, where L is the specimen length at the zero-stress state. The cross-sectional area at

the breaking point is 1/(1 + 1.99) times of that at zero-stress state under the rough assumption of incompressibility. The elastic modulus at the breaking point is then obtained from the regression curve F as $E = 10^{-9}(1 + 1.99)(1 + 1.99)F'/((10^{-7})^2\,\pi)$ = 104 MPa, which is ~70-fold of the Young's modulus at the zero-stress point, where F' is the derivative of F at S = 1.99. Thus, elastic modulus of SFs increased nonlinearly as stretch proceeds; yet, it was still one order of magnitude smaller at the breaking point than that of actin filaments or thick filaments, 1.0 GPa [17].

According to the regression curve (Fig. 6), when stretching strain of SFs increased 5% from the physiological strain S = 0.2, the stiffness, given by the first derivative, increased 4.6%. Pourati et al. [10] reported that 5% stretch caused 30% increase in stiffness of living endothelial cells. Even though the measuring methods and the definitions of stiffness are different between this and Pourati's studies, the result suggests that strain-induced stiffening, a key mechanical feature of living adherent cells [3], was observed in a physiological strain range of single SFs; therefore, SFs may bear intracellular stresses that affect overall cell mechanical properties.

SFs have a heterogeneous structure, which was neglected at this stage in order to establish averaged or apparent macroscopic properties. Since detailed microstructure of SFs remains unknown, a structure assumption would be necessary to explain the mechanism of the mechanical properties, which will be the subject of future investigation. Despite some limitations, the mechanical properties determined here will be fundamental in considering force transmission in the cytoplasm [18–22]. So far, numerical approaches attempted to explain mechanical behaviors of living cells [23, 24]. Those results, however, seem lacking quantitative validity since those models were based on fundamental cytoskeletal components such as actin filaments and microtubules, not SFs. Since individual microtubules were supposed to play a critical role in bearing stresses in those models, force levels allowing to deform cell or to provoke the strain-induced stiffening were on the order of 1–10 pN [24]. This may be true when the only existing forces are thermal forces or protein-producing forces, i.e. on the order of ~10 pN [15, 16]. In cell scale, however, forces of much higher order of magnitude ~10 nN, such as cell traction force [5], are present at single adhesion sites to determine the whole cell integrity. Therefore, single microtubules solely cannot be viewed as stiff structural components in the cell architecture or a major determinant for it. Alternatively, enhancement of bearable force for microtubules by surrounding cytoskeletal lattice [19] or cell organelles [2, 6] should be taken into account to explain quantitatively intracellular force transmission via microtubules. Thus, there is a hierarchy in the cell structure, where existing forces are different in magnitude at each scale. The present study showed SFs themselves were extensible and strain-induced stiffened in a physiological strain range, and forces were consistent in magnitude between the local traction forces at adhesion sites and tension in SFs. These results suggest that SFs are a principal structural component in bearing intracellular stresses at the cell bottom.

4 Conclusions

We measured preexisting strain and tensile properties of SF isolated from SMCs and ECs to understand its macroscopic and average mechanical behavior. SFs shortened after they were detached from the substrate in an ATP-independent manner to ~80% of the original length, indicating that a stretching strain of ~0.2 may exist in SFs in the cytoplasm. Tensile test showed that the isolated SFs had ~300–1500-kPa Young's modulus. Tensile force existing in SFs in cells was estimated to be ~10 nN based on the force–strain relationship. These findings will be fundamental in considering the contribution of SFs to intracellular force transmission from quantitative viewpoints.

Acknowledgments

The authors thank Dr. N. Sakamoto for fruitful discussions. This work was supported in part by Grants-in-Aids for Priority Areas (No. 15086202), Scientific Research (A) (No. 14208100), and Young Scientists (B) (No. 17700397) from the Ministry of Education, Culture, Sports, Science, and Technology of Japan.

References

1. Davies, P.F., 1995. Flow-mediated endothelial mechanotransduction. Physiol. Rev. 75, 519-560.
2. Deguchi, S., Maeda, K., Ohashi, T., Sato, M., 2005. Flow-induced hardening of endothelial nuclei as an intracellular stress-bearing organelle. J. Biomech. 38, 1751-1759.
3. Ingber, D.E., 1997. Tensegrity: the architechtural basis of cellular mechanotransduction. Ann. Rev. Physiol. 59, 575-599.
4. Katoh, K., Kano, Y., Masuda, M., Onishi, H., Fujiwara, K., 1998. Isolation and contraction of the stress fiber. Mol. Biol. Cell 9, 1919-1938.
5. Tan, J.L., Tien, J., Pirone, D.M., Gray, D.S., Bhadriraju, K., Chen, C.S., 2003. Cells lying on a bed of microneedles: an approach to isolate mechanical force. Proc. Natl. Acad. Sci. USA 100, 1484-1489.
6. Deguchi, S., Ohashi, T., Sato, M., 2005. Intracellular stress transmission through actin stress fiber network in adherent vascular cells. Mol. Cell. Biomech. 2, 205-216.
7. Deguchi, S., Ohashi, T., Sato, M., 2005. Evaluation of tension in actin bundle of endothelial cells based on preexisting strain and tensile properties measurements. Mol. Cell. Biomech. 2, 125-134.

8. Deguchi, S., Ohashi, T., Sato, M., 2006. Tensile properties of single stress fibers isolated from cultured vascular smooth muscle cells. J. Biomech. 39, 2603-2610.
9. Deguchi, S., Ohashi, T., Sato, M., 2005. Newly designed tensile test system for in vitro measurement of mechanical properties of cytoskeletal filaments. JSME Int. J. 48C, 396-402.
10. Pourati, J., Maniotis, A., Spiegel, D., Schaffer, J.L., Butler, J.P., Fredberg, J.J., Ingber, D.E., Stamenovic, D., Wang, N., 1998. Is cytoskeletal tension a major determinant of cell deformability in adherent endothelial cells? Am. J. Physiol. Cell Physiol. 274, C1283-C1289.
11. Liu, X., Pollack, G.H., 2002. Mechanics of F-actin characterized with microfabricated cantilevers. Biophys. J. 83, 2705-2715.
12. Tsuda, Y., Yasutake, H., Ishijima, A., Yanagida, T., 1996. Torsional rigidity of single actin filaments and actin-actin bond breaking force under torsion measured directly by in vitro micromanipulation. Proc. Natl. Acad. Sci. USA 93, 12937-12942.
13. Haga, H., Sasaki, S., Kawabata, K., Ito, E., Ushiki, T., Abe, K., Sambongi, T., 2000. Elasticity mapping of living fibroblasts by AFM and immunofluorescence observation of cytoskeleton. Ultramicroscopy 82, 253-258.
14. Charras, G.T., Horton, M.A., 2002. Determination of cellular strains by combined atomic force microscopy and finite element modeling. Biophys. 83, 858-879.
15. Gittes, F., Mickey, B., Nettleton, J., Howard, J., 1993. Flexural rigidity of microtubules and actin filaments measured from thermal fluctuations in shape. J. Cell Biol. 120, 923-934.
16. Kojima, H., Ishijima, A., Yanagida, T., 1994. Direct measurement of stiffness of single actin filaments with and without tropomyosin by in vitro nanomanipulation. Proc. Natl. Acad. Sci. USA 91, 12962-12966.
17. Dunaway, D., Fauver, M., Pollack, G.H., 2002. Direct measurement of single synthetic vertebrate thick filament elasticity using nanofabricated cantilevers. Biophys. J. 82, 3128-3133.
18. Wang, N. and Suo, Z., 2005. Long-distance propagation of frces in a cell. Biochem. Biophys. Res. Commun. 328, 1133-1138.
19. Brangwynne, C.P., MacKintosh, F.C., Kumar, S., Geisse, N.A., Talbot, J., Mahadevan, L., Parker, K.K., Ingber, D.E., Weitz, D.A., 2006. Microtubules can bear enhanced compressive loads in living cells because of lateral reinforcement. J. Cell Biol. 173, 733-741.
20. Kumar, S., Maxwell, I.Z., Heisterkamp, A., Polte, T.R., Lele, T.P., Salanga, M., Mazur, E., Ingber, D.E., 2006. Viscoelastic retraction of single living stress fibers and its impact on cell shape, cytoskeletal organization, and extracellular matrix mechanics. Biophys. J. 90, 3762-3773.

21. Hu, S. and Wang, N., 2006. Control of stress propagation in the cytoplasm by prestress and loading frequency. Mol. Cell. Biomech. 3, 49-60.
22. Na, S., Meininger, G.A., Humphrey, J.D., 2007. A theoretical model for F-actin remodeling in vascular smooth muscle cells subjected to cyclic stretch, J. Theor. Biol. 246, 87-99.
23. Stamenovic, D., Fredberg, J.J., Wang, N., Butler, J.P., Ingber, D.E., 1996. A microstructural approach to cytoskeletal mechanics based on tensegrity. J. Theor. Biol. 181, 125-136.
24. Volokh, K.Y., Vilnay, O., Belsky, M., 2000. Tensegrity architecture explains linear stiffening and predicts softening of living cells. J. Biomech. 33, 1543-1549.

BIOPHYSICAL MECHANISMS OF TENSION-DEPENDENT FORMATION OF STRESS FIBERS FROM ACTIN MESHWORK

H. HIRATA[1,2], H. TATSUMI[3] AND M. SOKABE[1,2,3]

[1]ICORP/SORST, Cell Mechanosensing Project, Japan Science and Technology Agency, 65 Tsurumai, Showa-ku, Nagoya, Aichi 466-8550, Japan; [2]Department of Molecular Physiology, National Institute for Physiological Sciences, Okazaki, Aichi 444-8585, Japan; [3]Department of Physiology, Graduate School of Medicine, Nagoya University, 65 Tsurumai, Showa-ku, Nagoya Aichi 466-8550, Japan

E-mail: msokabe@med.nagoya-u.ac.jp

The actin cytoskeleton, stress fiber, is an actomyosin-based contractile structure seen as a bundle of actin filaments. Although tension developed in a cell is believed to affect stress fiber formation, little is known for the underlying biophysical mechanisms. To address this question, we examined the effects of tension on the behaviors of individual actin filaments during stress fiber (actin bundle) formation using cytosol-free semi-intact fibroblast cells that were pre-treated with the Rho kinase inhibitor Y-27632 to disassemble stress fibers into a meshwork of actin filaments. When ATP and Ca^{2+} were applied to these semi-intact cells, centripetal traction forces were generated in the meshwork due to its actomyosin-based contractile nature. Then the actin meshwork in protruded a lamella was reorganized into ordered actin bundles oriented along the direction of the generated tension in the meshwork. Dragging the meshwork towards the cell baody with externally applied mechanical forces excerted essentially the same effects as ATP and Ca^{2+}, strongly suggesting that directed force (tesion) is essential for the actin bundles formation. By tracking the motion of quantum dot-labeled actin filaments during the bundles formation, it was revealed that individual actin filaments in the meshwork moved towards the cell body with intermittent and sudden changes in their direction, which may reflect the destruction and construction processes of cross-links between actin filaments. These results suggest that force-dependent remodeling of cross-links within the actin meshwork is crucial for the rearrangement of actin filaments into oriented actin bundles.

1 Introduction

In endothelial cells and fibroblasts, bundles of actin filaments, called stress fiber, are developed [1,2]. Stress fibers are capable of contractility [3,4] that exerts traction forces on cell-to-substrate contact regions, focal adhesions [5,6]. This force exertion is crucial for regulating focal adhesions [6,7] and remodeling extracellular matrices [8].

It has been well established that intracellular and extracellular mechanical environments largely affect the formation and the orientation of stress fibers in concert with certain intracellular chemical signaling. Cellular contractility mediated by the small GTPase Rho is necessary for the formation of stress fibers [9]. Fibroblasts within an anchored collagen gel develop stress fibers but not within a floating gel [10], probably because the rigidity of the floating gel is insufficient to

produce enough tension in cells. When cells are subjected to mechanical forces generated by fluid flow [11] or pulling a cell with a microneedle [12,13], stress fibers are aligned along the direction of developed tension.

Machesky and Hall [14] showed that stress fibers are assembled primarily from pre-existing actin filaments. It has been mentioned that tension development in the pre-existing actin cytoskeleton is crucial for the formation of stress fibers [12,13,15]. However, the effects of tension on the dynamic behaviors of individual actin filaments have not been clarified. Actin filaments are thought to be mechanically interconnected to form a meshwork structure [16], and tension would act on these mechanical connections to reorganize the meshwork into bundles. Direct observations of individual actin filaments in the meshwork under tension will provide a basis for biophysical understanding of the tension-dependent formation of stress fibers.

In this report, we summarize our recent studies [17,18] on the behaviors of actin filaments during tension-dependent reorganization of actin meshwork into actin bundles. Actin filaments in digitonin-permeabilized fibroblast cells (semi-intact cells) were sparsely labeled with quantum dots (Qdots), and their movements in response to tension development were tracked and analyzed.

2 Materials and Methods

2.1 Cell culture

Human foreskin fibroblasts, Hs 68 cells, were cultured in Dulbecco's modified Eagle's medium supplemented with 10% fetal bovine serum at 37°C in 5% CO_2. Cells were grown on glass coverslips. For the dragging-lamella experiments, cells were grown on fibronectin-conjugated polyacrylamide gel substrata prepared as described by Dembo and Wang [19]; concentrations of acrylamide and bis-acrylamide were 10% and 0.05%, respectively.

2.2 Preparation of semi-intact cells

Digitonin-permeabilized semi-intact cells were prepared as described previously [17]. After a treatment with 20 μM Y-27632 for 1h at 37°C, cells were permeabilized with 0.003% digitonin in the presence of 3.3 U/ml Alexa488-phalloidin (Molecular Probes, Inc., Eugene, OR) in a working solution (125 mM potassium acetate, 2.5 mM $MgCl_2$, 1 mM $MnCl_2$, 25 mM HEPES, 12 mM glucose, 0.1 μM phenylarsine oxide, 10 μg/ml leupeptin, 10 μg/ml pepstatin, 10 μg/ml chymostatin, and 10 mM dithiothreitol; pH = 7.0) for 1 min at room temperature. Semi-intact cells with actin filaments labeled with Qdots were prepared as follows; Y-27632-treated cells were permeabilized for 1 min with 0.003% digitonin in the presence of 0.33 μM biotinXX-phalloidin (Molecular Probes, Inc.), then treated

with 0.1 nM streptavidin-conjugated Qdot (Quantum Dot Co., Hayward, CA) for 1 min. Qdots were applied in the presence of 1% BSA. After washing the preparation with the working solution, unbound Qdots were removed from the semi-intact cells, ensuring the specificity of labeling actin filaments with Qdots [17].

When semi-intact cells were treated with blebbistatin, 1% BSA was added to the working solution as vehicle. One-percent BSA did not affect the actin filaments' organization in semi-intact cells. As the motions of Qdots were not altered with a lowered Qdot density (1/5 of standard), Qdot-labeling itself should have little effect on the dynamics of actin filaments.

2.3 Fluorescence microscopy

An epi-fluorescence microscope (IX70, OLYMPUS, Tokyo) equipped with an oil immersion objective (NA 1.40, 100×; PlanApo, OLYMPUS) and a charge-coupled device camera (Micromax, Princeton Instruments, Trenton, NJ) was used for observations of actin filaments labeled with Alexa488. Photobleaching experiments were performed by focusing a solid state blue laser (λ = 473 nm; HK-5512-01, SHIMADZU Co., Kyoto, Japan) on the specimen. Qdots bound to actin filaments were illuminated with the blue laser and imaged with the same microscope. The acquired images were analyzed off line with the public domain ImageJ program (version 1.36b).

2.4 Tracking and analysis of single Qdots movement

As the Qdot is a nano-crystal of semiconductor with bright fluorescence and high photo-stability [20], Qdots can be used as a fluorescent marker for long-term tracking of the motion of intracellular molecules. The position of each Qdot was determined frame-by-frame by calculating the centroid of the fluorescence image of the Qdot.

Qdots exhibited repeated changes in the direction of their motion (see Results). To quantify the period between the directional changes, the motion of a Qdot was analyzed as a "persistent random walk" [21]. In a persistent random walk, mean square displacement (*MSD*) is expressed as a function of time intervals (Δt) and persistence time (P) as follows;

$$MSD \propto P[\Delta t - P\{1-\exp(-\Delta t/P)\}].$$

The parameter P represents a measure of the average time period between "significant" changes in the direction of movement [21].

2.5 Dragging lamella

Glass capillaries with a diameter of 1 mm (G-1, Narishige Co., Tokyo) were pulled with a Flaming/Brown micropipette puller (P-97, Sutter Instrument Co., Novato, CA). The micropipettes were bent in the middle by heating them with a gas burner.

They were then treated with 3-aminopropyltriethoxysilane, dried, coated with 20% glutaraldehyde for 5 min at room temperature, and washed before use. When samples were in 0.1 mM ATP and 0.1 mM $CaCl_2$-containing working solution for 3 min, the tip of the micropipette was attached on a lamella of a semi-intact cell horizontally and then it was dragged by using a micromanipulator (MC-35A, Narishige Co.). To avoid clashing the actin filament meshwork by pressing the micropipette, the dragging of a lamella was performed on a flexible polyacrylamide substratum.

3 Results

Cells were treated with the Rho kinase inhibitor Y-27632 for 1 h to disorganize stress fibers and then permeabilized with 0.003% digitonin in the presence of Alexa488-phalloidin to make semi-intact cells with fluorescently labeled actin filaments. In lamellae of semi-intact cells, there were no apparent actin bundles; instead uniform staining of actin filaments was observed (Fig. 1A), suggesting the

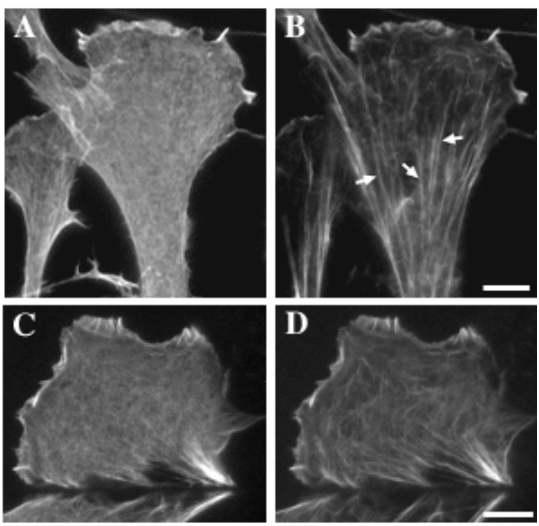

Figure 1. Formation of actin bundles in lamellae of semi-intact cells. Cells were permeabilized with 0.003% digitonin after treatment with 20 μM Y-27632 for 1 h. (A) Uniform staining of actin filaments with Alexa488-phalloidin in a lamella of a semi-intact cell. (B) The same field as in (A) was imaged 15 min after the application of 0.1 mM ATP and 0.1 mM $CaCl_2$. Actin bundles oriented along the long axis of the cell were formed (*arrows*). (C) Alexa488-phalloidin-stained actin filaments in a lamella isolated from the cell body. (D) The same field as in (D) was imaged 15 min after the application of 0.1 mM ATP and 0.1 mM $CaCl_2$. Only short and winding bundles were formed. Bars, 10 μm. Reprinted from [17] and [18] with permission from JSME and Elsevier.

existence of an isotropic meshwork of actin filaments. When semi-intact cells were treated with 0.1 mM ATP and 0.1 mM $CaCl_2$, the actin meshwork in lamellae was transformed into actin bundles oriented along the long axis of the cell (Fig. 1B). These actin bundles contained myosin, filamin and α-actinin, as seen in stress fibers. The formation of actin bundles was almost completely inhibited by the myosin II inhibitor blebbistatin. These results suggest that actin bundles can be formed by reorganization of actin meshwork in a myosin II-dependent manner.

When a part of the Alexa488-phalloidin-stained actin meshwork in a lamella was photobleached and the motion of the photobleached area was observed, the photobleached area moved inside the lamella toward the cell body in response to ATP and $CaCl_2$ (data not shown). Since the periphery of the meshwork in a lamella remained in the same region while the central domain of the meshwork in the lamella moved toward the cell body, it is conceivable that centripetal forces are generated in the meshwork in the presence of ATP and $CaCl_2$. In a lamella severed with a glass micropipette in order to isolate it from the cell body, actin meshwork showed no movement towards the cell body (data not shown), suggesting that no long-range, directed force developed in the actin meshwork of this preparation. In the isolated lamellae, actin bundles formed in response to ATP and $CaCl_2$ were short and winding (Figs. 1C and D). These results suggest that the formation of oriented actin bundles depends on the large scale centripetal forces generated in the actin meshwork.

We next examined the movements of individual actin filaments during the formation of actin bundles. For this purpose, actin filaments in the meshwork were sparsely labeled with Qdots and the trajectories of individual Qdots were tracked and analyzed. When the motion of individual Qdots was tracked in the presence of ATP and $CaCl_2$, trajectories of neighboring Qdots often merged into a single line (Fig. 2A), suggesting that neighboring actin filaments merged into a thick actin bundle.

Individual Qdots moving towards the cell body were accompanied with sudden changes in the direction of their movements (Fig. 2B). The timing of the directional changes was independent among Qdots, indicating that the directional changes of Qdot movements are not due to changes in the direction of movement of the entire actin meshwork. To evaluate the interval time between the directional changes, the movements of individual Qdots were analyzed as a “persistent random walk”. The persistence time, which corresponds to the average time period between directional changes, was 84 ± 82 s (mean ± SD; Fig. 2C); i.e., the mean frequency of directional changes was 0.7 turns/min. Sudden changes in the direction of Qdot motion were also seen in the lamellae subjected to an externally applied artificial force, where a semi-intact cell was treated with ATPγS, a non-hydrolyzable analog of ATP, instead of ATP, and the lamella was dragged with a micropipette (data not shown). These observations suggest that sudden changes in the direction of Qdot motion are induced by large-scale tension in the actin meshwork. We will discuss the

mechanisms underlying the motions of Qdots and the relation between these motions and the formation of oriented actin bundles.

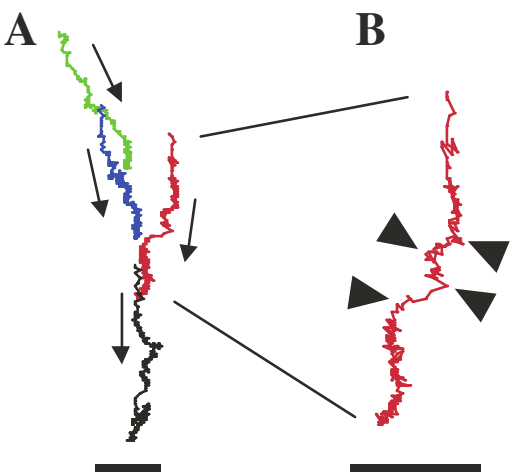

Figure 2. Tracking of the movements of Qdot-labeled actin filaments during the formation of oriented actin bundles in lamellae of semi-intact cells. (A) Trajectories of 4 Qdots bound to actin filaments in a lamella of a semi-intact cell in the presence of 0.1 mM ATP and 0.1 mM $CaCl_2$. Motion of Qdots was tracked from immediately after the application of ATP and Ca^{2+} in 2-s interval for 800 s. These Qdots moved downward as indicated by *arrows*, corresponding to the movement toward the cell body. (B) The trajectory colored red in (A) is enlarged. Sudden changes in the direction of the movement were seen (*arrowheads*). Bars, 1 μm.

4 Discussion

Our analyses of the process of actin bundles formation in semi-intact fibroblasts suggest that the formation of oriented actin bundles depends on directed tension in the actin meshwork. Since the digitonin-treated plasma membrane is permeable to molecules of at least 200 kDa [22] and to streptavidin-conjugated Qdots (ca. 10 nm in diameter), monomeric actin (42 kDa) can pass through the digitonin-treated plasma membrane, and semi-intact cells will lose monomeric actin. Therefore, it is conceivable that rearrangement of pre-existing actin filaments is responsible for the formation of actin bundles in our semi-intact cells.

We showed that actin filaments in lamellae exhibited sudden changes in the direction of their movements during the actin bundle formation. In a uni-axially deformed meshwork, in which actin filaments are cross-linked randomly, the force vectors acting on individual filaments would differ among filaments. When tension in the actin meshwork increases, weak links between the filaments in the meshwork

will be disrupted, which will change the local distribution of tension in the meshwork, leading to sudden changes in the direction of the motion of actin filaments.

How does tension in the actin meshwork induce the formation of oriented actin bundles? We present a hypothetical model based on the motions of Qdots. We assume here that short winding bundles are formed in the meshwork before tension develops along the long axis of the cell and that these bundles are cross-linked (Fig. 3Aa) as seen in the isolated lamellae. When tension along the long axis of the cell develops in the meshwork, weak links will be disrupted (Fig. 3Ab). Since peripheral termini of these bundles are anchored to the substratum (Figs. 3Aa-d, *red points*), these bundles are stretched and aligned along the direction of tension (Fig. 3Ac). Then, actin filaments and actin bundles with free ends will be gradually fused to the stretched bundles by the actomyosin-based zippering (Fig. 3Ad), consequently forming thick straight bundles oriented along the tension. Then the movements of Qdots on individual actin filaments would show sudden changes in their direction in accordance with the disruption of cross-links (Fig. 3B).

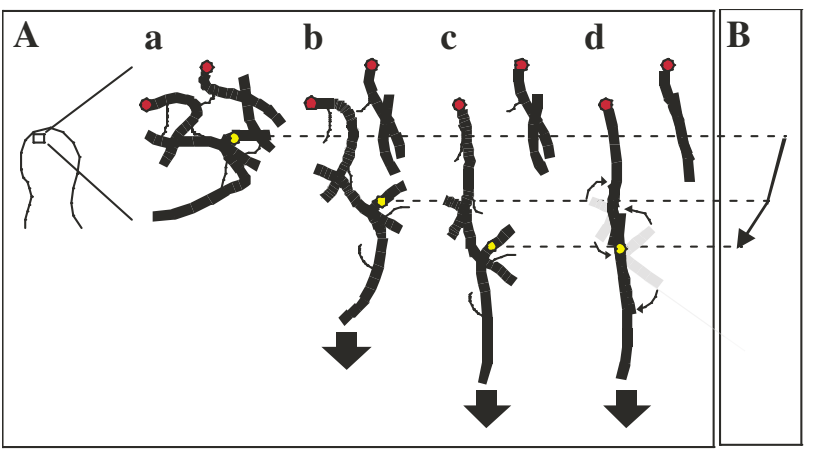

Figure 3. A schematic drawing of a hypothetical model of the tension-dependent formation of oriented actin bundles in semi-intact cells. (Aa) Short winding bundles (*black heavy line*) are formed in the meshwork before the development of tension along the long axis of the cell. These bundles are cross-linked to each other. A yellow dot represents a Qdot bound to an actin bundle. (Ab) When tension develops in the meshwork, weak links are disrupted. (Ac) Since the peripheral termini of these bundles are anchored to the substratum (*red points*), these bundles are stretched and aligned along the tension. (Ad) Actin filaments and actin bundles with free ends gradually fuse to the stretched bundles by actomyosin-based zippering. (B) An envisaged trajectory of the Qdot. Disruption of a cross-link confers a new mechanical balance in the meshwork, and the direction of the movement of the Qdot on the actin filament changes according to the new mechanical balance. Reprinted from [18] with permission from Elsevier.

Architecture of cytoskeletal network has been modeled by Ingber based on tensegrity [15]. This model can partially account for tension-dependent reorganization of cytoskeletal network. In the original tensegrity model, cytoskelatal elements were assumed to be interconnected stably each other maintaining tensional integrity of the network. However, it has been predicted that severing a part of the network is necessary for the formation of locally emerging structures such as actin bundles in the network [15,23]. Consistently with this hypothesis, we herein showed experimental results suggesting remodeling of cross-links between actin filaments during the formation of actin bundles, which process was included in our model described above. The remodeling of cross-links was suggested to depend on tension developed in the actin meshwork. Actin filaments in the meshwork could be cross-linked with various cross-linking proteins including α-actinin, filamin and myosin II. Further studies are needed to clarify the cross-link(s) remodeled during the tension-dependent actin bundles formation.

In this study, we showed reorganization of actin meshwork into bundles oriented along the direction of tension in cytosol-free semi-intact cells. In semi-intact cells, another cytoskeleton, microtubules are largely fragmented [17], and integrity of plasma membranes is disrupted. Therefore, actin meshwork seems to be responsible for transducing macroscopic vectorial mechanical signals into the formation of oriented bundles. To support this, when mechanical forces were externally applied on the cell body of a semi-intact cell, movements of actin filaments located near the periphery of the lamella were observed (our unpublished result), which suggests that mechanical forces acting on actin meshwork can be transmitted at a far distance. In other words, actin meshwork can act as a long-range transmitter of mechanical signals. Such a property of actin meshwork may be essential for the formation of stress fibers linking between focal adhesions located at a distance.

Acknowledgments

This work was supported in part by Grants-in-aid for Scientific Research on Priority Areas (#15086270 to M.S.), General Scientific Research (#13480216 to M.S. and #14580769 to H.T.), Creative Research (#16GS0308 to M.S.) from the Ministry of Education, Cultures, Sports, Science and Technology of Japan and a grant from Japan Space Forum (to M.S. and H.T.).

References

1. Ridley, A.J., Hall, A., 1992. The small GTP-binding protein rho regulates the assembly of focal adhesions and actin stress fibers in response to growth factors. Cell 70, 389-399.

2. Vouret-Craviari, V., Boquet, P., Pouyssegur, J., Van Obberghen-Schilling, E., 1998. Regulation of the actin cytoskeleton by thrombin in human endothelial cells: role of Rho proteins in endothelial barrier function. Mol. Biol. Cell 9, 2639-2653.
3. Isenberg, G., Rathke, P.C., Hülsmann, N., Franke, W.W., Wohlfarth-Bottermann, K.E., 1976. Cytoplasmic actomyosin fibrils in tissue culture cells. Direct proof of contractility by visualization of ATP-induced contraction in fibrils isolated by laser microbeam dissection. Cell Tissue Res. 166, 427-443.
4. Katoh, K., Kano, Y., Masuda, M., Onishi, H., Fujiwara, K., 1998. Isolation and contraction of the stress fiber. Mol. Biol. Cell 9, 1919-1938.
5. Smilenov, L.B., Mikhailov, A., Pelham, R.J., Marcantonio, E.E., Gundersen, G.G., 1999. Focal adhesion motility revealed in stationary fibroblasts. Science 286, 1172-1174.
6. Balaban, N.Q., Schwarz, U.S., Riveline, D., Goichberg, P., Tzur, G., Sabanay, I., Mahalu, D., Safran, S., Bershadsky, A., Addadi, L., Geiger, B., 2001. Force and focal adhesion assembly: a close relationship studied using elastic micropatterned substrates. Nat. Cell Biol. 3, 466-472.
7. Riveline, D., Zamir, E., Balaban, N.Q., Schwarz, U.S., Ishizaki, T., Narumiya, S., Kam, Z., Geiger, B., Bershadsky, A.D., 2001. Focal contacts as mechanosensors: externally applied local mechanical force induces growth of focal contacts by an mDia1-dependent and ROCK-independent mechanism. J. Cell Biol. 153, 1175-1185.
8. Zhong, C., Chrzanowska-Wodnicka, M., Brown, J., Shaub, A., Belkin, A., Burridge, K., 1998. Rho-mediated contractility exposes a cryptic site in fibronectin and induces fibronectin matrix assembly. J. Cell Biol. 141, 539-551.
9. Chrzanowska-Wodnicka, M., Burridge, K., 1996. Rho-stimulated contractility drives the formation of stress fibers and focal adhesions. J. Cell Biol. 133, 1403-1415.
10. Farsi, J.M.A., Aubin, J.E., 1986. Microfilament rearrangements during fibroblast-induced contraction of three-dimensional hydrated collagen gels. Cell Motil. 4, 29-40.
11. Wechezak, A.R., Viggers, R.F., Sauvage, L.R., 1985. Fibronectin and F-actin redistribution in cultured endothelial cells exposed to shear stress. Lab. Invest. 53, 639-647.
12. Kolega, J., 1986. Effects of mechanical tension on protrusive activity and microfilament and intermediate filament organization in an epidermal epithelium moving in culture. J. Cell Biol. 102, 1400-1411.
13. Maniotis, A.J., Chen, C.S., Ingber, D.E., 1997. Demonstration of mechanical connections between integrins, cytoskeletal filaments, and nucleoplasm that stabilize nuclear structure. Proc. Natl. Acad. Sci. USA 94, 849-854.

14. Machesky, L.M., Hall, A., 1997. Role of actin polymerization and adhesion to extracellular matrix in Rac- and Rho-induced cytoskeletal reorganization. J. Cell Biol. 138, 913-926.
15. Ingber, D.E., 1993. Cellular tensegrity: defining new rules of biological design that govern the cytoskeleton. J. Cell Sci. 104, 613-627.
16. Heuser, J.E., Kirschner, M.W., 1980. Filament organization revealed in platinum replicas of freeze-dried cytoskeletons. J. Cell Biol. 86, 212-234.
17. Hirata, H., Tatsumi, H., Sokabe, M., 2004. Tension-dependent formation of stress fibers in fibroblasts: a study using semi-intact cells. JSME Int. J. 47C, 962-969.
18. Hirata, H., Tatsumi, H., Sokabe, M., Dynamics of actin filaments during tension-dependent formation of actin bundles. Biochim. Biophys. Acta, in press.
19. Dembo, M., Wang, Y.-L., 1999. Stresses at the cell-substrate interface during locomotion of fibroblasts. Biophys. J. 76, 2307-2316.
20. Chan, W.C.W., Nie, S., 1998. Quantum dot bioconjugates for ultrasensitive nonisotopic detection. Science 281, 2016-2018.
21. DiMilla, P.A., Albelda, S.M., Lauffenburger, D.A., Quinn, J.A., 1992. Measurement of individual cell migration parameters for human tissue cells. AIChE J. 37, 1092-1104.
22. Schulz, I., 1990. Permeabilizing cells: some methods and applications for the study of intracellular processes. Methods Enzymol. 192, 280-300.
23. Forgacs, G., 1995. On the possible role of cytoskeletal filamentous networks in intracellular signaling: an approach based on percolation. J. Cell Sci. 108, 2131-2143.

This page intentionally left blank

III. TISSUE ENGINEERING

This page intentionally left blank

EFFECTS OF CYCLIC HYDROSTATIC PRESSURE LOADING ON REGULATION OF CHONDROCYTE PHENOTYPES

A. OURA, M. KAWANISHI AND K. S. FURUKAWA

Biomedical Engineering Laboratory, Department of Mechanical Engineering, Graduate School of Engineering, The University of Tokyo, 7-3-1 Hongo, Bunkyo-ku, Tokyo 113-8656, Japan

T. USHIDA

Center for Disease Biology and Integrative Medicine, School of Medicine, The University of Tokyo, 7-3-1 Hongo, 113-0033 Tokyo, Japan
E-mail: ushida@m.u-tokyo.ac.jp

It is known that articular chondrocytes loose their phenotype in vitro according to subculturing them. On the other hand, proliferation in vitro of collected articular chondrocytes is indispensable for regenerating articular cartilages. Therefore, redifferentiation of dedifferentiated chondrocytes is required in tissue engineering. Hydrostatic pressure is one of the most frequently used mechanical stimuli in chondrocyte experiments. A variety of hydrostatic pressure loading devices have been used in cartilage cell experiments. However, no gas-controlled system with other than a low pressure load was used up to this time. Hence we used a polyolefin bag from which gas penetration was confirmed. Chondrocytes were extracted from bovine normal knee joint cartilage. After 3 passages, dedifferentiated chondrocytes were seeded and cultured in chemically defined serum-free medium with ITS + Premix for 3 days. Then 3.5 MPa of cyclic hydrostatic pressure was applied at 0.5 Hz for 4 h or 24 h per day for 4 days. Semiquantitative reverse transcriptase-polymerase chain reaction showed a 3-fold increase in the levels of aggrecan mRNA due to cyclic hydrostatic pressure load ($p < 0.15$). Type II collagen mRNA levels were also up-regulated 2-fold by a cyclic hydrostatic pressure load ($p < 0.15$). Type I collagen mRNA levels were similarly reduced in the cyclic hydrostatic pressure load group. The partial oxygen pressure (PO_2) and partial carbon dioxide pressure (PCO_2) of the medium in the bag reached equilibrium in 24 h, and no significant change was observed for 3 days afterwards. PO_2 and PCO_2 were very well controlled. These results suggest that gas-controlled cyclic hydrostatic pressure could regulate the phenotype of dedifferentiated chondorcytes into that of differentiated chondrocytes in vitro, enhancing cartilaginous matrix formation such as aggrecan and type II collagen.

1 Introduction

Articular cartilage defects have recently treated by using autologous chondrocyte transplantation in tissue engineering [1–3]. However, this treatment is still limited in focal defects. Many more cells are required to treat a large defect. Cells must be proliferated in vitro by a monolayer culture because of the very limited amount of donor biopsy cartilage available. However, monolayer culture proliferation leads to dedifferentiation. This is a process during which chondrocytes lose their ability to

express articular cartilage-specific extracellular matrices (ECM) such as type II collagen and aggrecan, and produce fibroblastspecific ECM, type I collagen [4, 5]. To be used for clinical applications, dedifferentiated cells must be redifferentiated. Different methods have been attempted to induce the redifferentiation of dedifferentiated articular chondrocytes so that they regain their cartilaginous features. These methods have included the application of growth factors or mechanical forces and the creation of an environment supporting a spherical morphology such as pellets, alginate beads, or polymer gels [6–13]. Hydrostatic pressure is one of the most frequently used mechanical factors in chondrocyte experiments. A variety of hydrostatic pressure loading devices have been reported for cartilage cell experiments [14–19]. However, no gas exchange system at other than a low pressure load had been used up to this time [18]. But articular cartilage is exposed to intermittent mechanical compression with peak load amplitudes of about 3.5–18 MPa in vivo [20]. Recently Toyoda et al. also reported the difficulty of gas control at such a pressure load [21]. Carver's system [22] and our previous system [23] had a medium circulation system, not only hydrostatic pressure loading. Further, our system had a risk of contamination in a long-term culture. Hence in this experiment we used a polyolefin bag from which gas infiltration was confirmed. The bag is already used for the self-storage of blood and for blood transfusions in the medical field, and confirmed to prevent bacterial and viral infection. Finally, we used a serum-free medium while performing cyclic hydrostatic pressure loading because serum contains many factors that affect chondrocyte metabolism. The aim of this study was to investigate the effect of gas-controlled cyclic hydrostatic pressure alone on 2-dimensionally seeded dedifferentiated articular chondrocytes. A novel experimental system was developed to apply gas-controlled cyclic hydrostatic pressure to 2-dimensionally cultured chondrocytes.

2 Materials and Methods

2.1 Cartilage harvest and cell culture

Cartilage was harvested under sterile conditions from bovine (12 weeks old) knee joints, dissected from the underlying bone, and minced into 1- to 2-mm^3 pieces. After being rinsed twice in cold Dulbecco's phosphate-buffered saline (PBS), the minced cartilage was digested with 0.2% collagenase CI (Worthington Biomedical, Freehold, NJ) in Ham's F-12 medium (GIBCO BRL, Rockville, MD) supplemented with antibiotics (100U/mL of penicillin, and 100 mg/mL of streptomycin, and 0.2 mg/mL of amphotericin B) under shaking overnight at 37°C. The digestion solution was filtered through a sterile 70-mm nylon mesh to remove any undigested fragments, and the chondrocytes were subsequently collected by centrifugation and washed twice with PBS. The cell number and viability were determined via a hemocytometer and the trypan blue exclusion dye test. The collected cells were

suspended in Ham's F-12 medium containing 10% fetal bovine serum (GIBCO BRL), 50 mg/mL of ascorbic acid (Wako, Osaka, Japan), and antibiotics (100U/mL of penicillin and 100 mg/mL of streptomycin, and 0.2 mg/mL of amphotericin B) solution (GIBCO BRL In). Initial seeding densities were approximately 1.6×10^4 cells/cm^2. Seeded cells were cultured under a 5% CO_2 atmosphere at 37°C. Near confluence (5×10^4 cells/cm^2), cells were passaged by trypsinization via standard procedures.

2.2 Chondrocyte seeding on the chamber slides for hydrostatic pressure loading

After 3 passages, 2.5×10^5 dedifferentiated cells were seeded on chamber slides (9.6 cm^2, NUNC 177372) with 0.5mL of serum-free medium. Our serum-free medium was a modification of the protocol outlined by Mackay et al. [24]. The main difference was exclusion of dexamethasone and transforming growth factor-b (TGF-b). These two elements have been reported to affect chondrogenic differentiation in vitro [25, 26] This medium consisted of high-glucose Dulbecco's modified Eagle's medium (GIBCO) supplemented with ITS Premix (BD Bioscience; final concentrations: 6.25 mg/mL of insulin, 6.25 mg/mL of transferrin, 6.25 ng/mL of selenous acid, 5.35 mg/mL of linoleic acid, 1.25mg/mL of bovine serum albumin), 50 mg/mL ofascorbic acid 2-phosphate (Sigma-Aldrich), 100 mg/mL of sodium pyruvate (Sigma-Aldrich), 40 mg/mL of proline (Sigma-Aldrich), and 2% antibiotics (100 U/mL of penicillin and 100 mg/mL of streptomycin, and 0.2 mg/mL of amphotericin B,) solution (GIBCO BRL). The cells were centrifuged at 500 g for 5 min and cultured in an incubator with 5% CO_2 atmosphere at 37°C for 3 days.

2.3 Application of hydrostatic pressure to seeded chondrocytes

A new system was constructed for the application of hydrostatic pressure to the pellet cultured in bags. The system was composed of a cylinder pump for high-performance liquid chromatography (SSC-3471; Senshu Scientific), a gas exchange tray, a pressure sensor (Yokohama System Laboratory), a PC-controlled air valve, and a pressure chamber. After 3 days culture, the chamber slides were stuffed in a polyolefin bag (Figure 1).

The bag was filled with serum-free medium (15mL). These 8 bags were placed into a pressure chamber and filled with the RO water that had finished a gas exchange in an incubator with a 5% CO_2 atmosphere at 37°C beforehand. The pressure chamber was placed in an incubator to maintain the culture temperature at 37°C. 3.5 MPa cyclic hydrostatic pressure was applied at 0.5 Hz for 4 h per day for 4 days. The frequency and magnitude of the hydrostatic pressure were manipulated via the PC-controlled air valve and the flowing quantity of the pump. A pressure sensor was installed in the line to continuously monitor the internal pressure of the chamber. An identical chamber placed in the same incubator was used for the control, but no loading was applied.

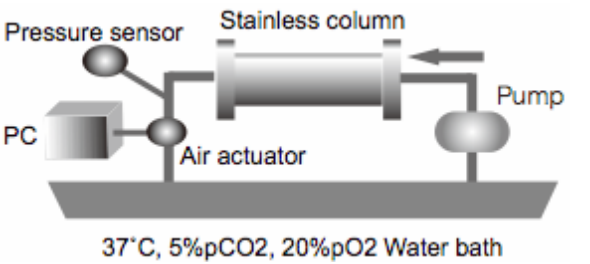

Figure 1. Schematic drawing of the system for cyclic hydrostatic pressure application with a polyolefin bag containing seeded dedifferentiated chondrocytes.

2.4 Gas analysis

In this experiment, we used the polyolefin bag from which the gas infiltration was confirmed. The partial oxygen pressure (PO_2) and partial carbon dioxide pressure (PCO_2) of the culture medium in the bags containing the pellets were measured via a blood gas analyzer (Rapidlab 348; Bayer). The samples were collected in 2.5-mL syringes with 23-gauge needles, which were inserted in a rubber block to seal them until the measurements were taken. Measurements were carried out immediately after the bags were heat-sealed and then at 24, 48, 72, and 96 h during the culture. The PO_2 and PCO_2 of the RO water in a gas exchange tray were also carried out in the same manner.

2.5 Analysis of messenger RNA (mRNA) levels

At the end of cyclic loading under 3.5 MPa of hydrostatic pressure, the chondrocytes were dissolved in guanidine isothiocyanate+ phenol (TRIzol Reagent; Invitrogen). The total RNA was extracted with chloroform (Sigma-Aldrich), precipitated with isopropanol (Wako), and washed with 70% ethanol (Wako). After recovery in diethylpyrocarbonate (DEPC)-treated water, the total RNA was determined and stored at -80°C. The RNA pellet was further purified with a GenElute Mammalian Total RNA Isolation Kit (Sigma-Aldrich) and then treated with 2U of DNase I (DNA-free; Ambion, Austin, TX). Total RNA was reverse transcribed (RT) with oligo dT (Invitrogen) and 2.5 mM dNTP (Takara) and 200 U of SuperScript III Reverse Transcriptase (Invitrogen) in a 20-mL reaction mixture for 50 min at 50°C and for 15 min at 70°C. A 1-mL aliquot of RT product was then used for a polymerase chain reaction (PCR) in a 19-mL reaction mixture containing 2.5 mM dNTP Mixture (TaKaRa), 0.5 U of Ex Taq (TaKaRa), and 1 mM primer (Table 1).

Co-amplification of the GAPDH gene was performed in the same PCR tubes as the internal standard to facilitate semi-quantitative determination of aggrecan, type I

Table 1. Sequences of primers for RT-PCR.

Gene	Primer	Sequence(50–30)
Aggrecan	Forward	CACTGTTACCGCCACTTCCC
	Reverse	GACATCGTTCCACTCGCCCT
Type I collagen	Forward	ATGCTCAGCTTTGTGGATACGCGG
	Reverse	AGGAAAGCCACGAGCACCCTGTGG
Type II collagen	Forward	AGCGTCCCCAAGAAGAACTGGTGG
	Reverse	GTCCACACCGAATTCCTGCTCGGG
GAPDH	Forward	ACCACAGTCCATGCCATCAC
	Reverse	TCCACCACCCTGTTGCTGTA

collagen, and type II collagen mRNA levels. The thermocycle included 1 cycle at 94°C for 5 min of initial denaturation, and 28 cycles at 94°C for 30 s, at 67°C for 30 s, and at 72°C for 2 min, followed by a final extension at 72°C for 7 min for GAPDH and aggrecan. The PCR conditions for type I collagen and type II collagen consisted of 1 cycle at 94°C for 5 min of initial denaturation, and 25 cycles at 94°C for 30 s, at 55°C for 1 min, and at 72°C for 2 min, followed by a final extension at 72°C for 7 min. The PCR products were electrophoresed on a 2% agarose gel and stained with 0.25 mg/mL of ethidium bromide, and the intensity of the bands was analyzed via an NIH Image. The signal levels for the aggrecan and type I and type II mRNA were expressed as ratios to the signal levels for GAPDH mRNA.

2.6 Statistical analysis

All the data from at least the duplicated experiments were expressed as ratios to the mean values of the control group (under no loading conditions). Values are shown as SEM. Statistical analysis was carried out using an unpaired t-test. P values less than 0.05 were considered significant.

3 Results

At the beginning of the experiment, the average PCO_2 of the medium in the bag was 32.3 mmHg (4.3%). The mean PO_2 of the medium in the bag was 159.8 mmHg (21%). These values were thought to be affected by the pellet movement operation time in the hood. Twenty-four hours after the sealing, the PCO_2 was 33.5 mmHg (4.4%), and PO_2 was 140.5 mmHg (18.5%). The mean PO_2 and PCO_2 of the medium in the bag reached equilibrium in 24 h, and no significant change was observed for 3 days afterwards. PO_2 and PCO_2 were controlled very carefully. Effect of hydrostatic pressure on expressions of matrices mRNA of 2-dimensionally seeded chondrocytes. The semi-quantitative RT-PCR showed that the expression of aggrecan mRNA levels increased to 3-fold ($p < 0.15$) (Fig. 2(A) and (B)). Type II collagen mRNA

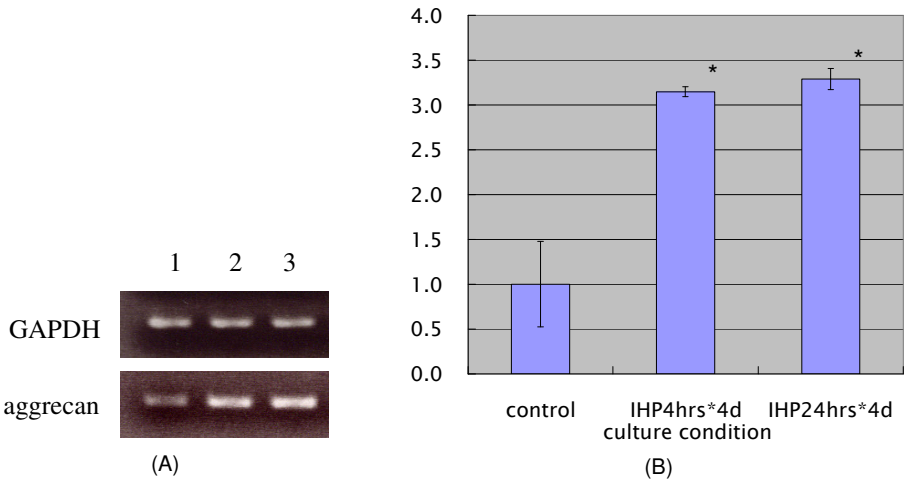

Figure 2. Effect of cyclic hydrostatic pressure on aggrecan mRNA levels. (A) Ethidium bromide–stained agarose analysis of RT-PCR samples in each group. 1. control, 2. four days' intermittent hydrostatic pressure loading (3.5 MPa, 0.5 Hz) during 4 hours/day, 3. four days' intermittent hydrostatic pressure loading (3.5 MPa, 0.5 Hz) during 24 hours/day. (B) Ratios of PCR products of aggrecan to those of GADPH, normalized to the control mean in each group. Values are the means ± SEM (n = 3), *p < 0.15.

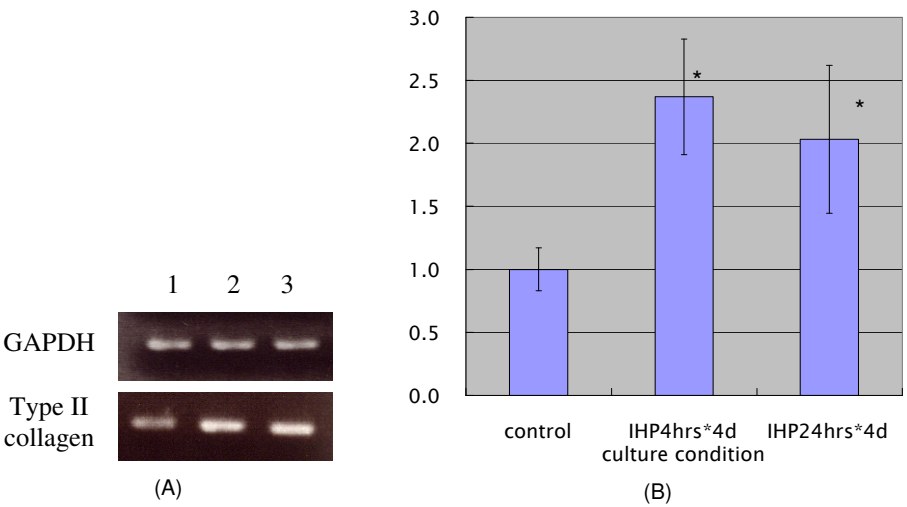

Figure 3. Effect of cyclic hydrostatic pressure on type II collagen mRNA levels. (A) Ethidium bromide–stained agarose analysis of RT-PCR samples in each group. 1. control, 2. four days' intermittent hydrostatic pressure loading (3.5 MPa, 0.5 Hz) during 4 hours/day, 3. four days' intermittent hydrostatic pressure loading (3.5 MPa, 0.5 Hz) during 24 hours/day. (B) Ratios of PCR products of type II collagen to those of GADPH, normalized to the control mean in each group. Values are the means ± SEM (n = 3), *p < 0.15.

levels also up-regulated to 2-fold as a result of the cyclic hydrostatic pressure load ($p < 0.15$) (Fig. 3(A) and (B)). Type I collagen mRNA levels were reduced by the cyclic hydrostatic pressure loading in a statistically significant manner (Fig. 4(A) and (B)).

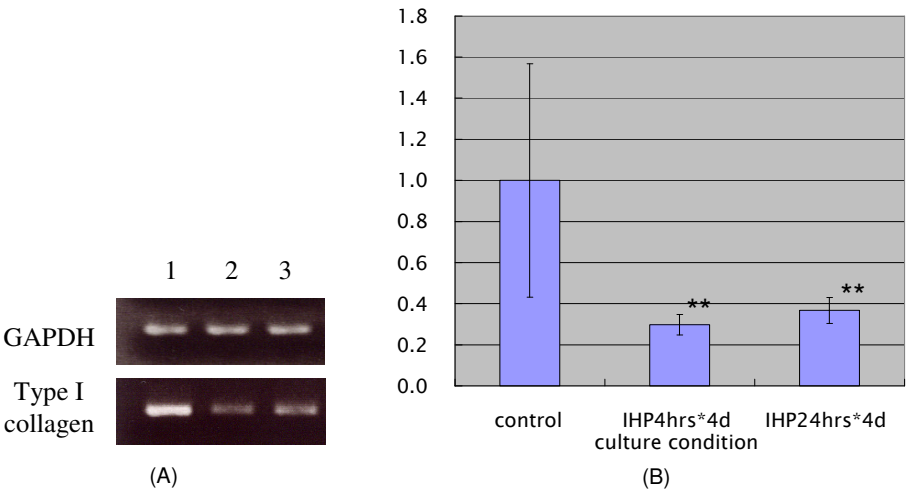

Figure 4. Effect of cyclic hydrostatic pressure on type I collagen mRNA levels. (A) Ethidium bromide–stained agarose analysis of RT-PCR samples in each group. 1. control, 2. four days' intermittent hydrostatic pressure loading (3.5 MPa, 0.5 Hz) during 4 hours/day, 3. four days' intermittent hydrostatic pressure loading (3.5 MPa, 0.5 Hz) during 24 hours/day. (B) Ratios of PCR products of type I collagen to those of GADPH, normalized to the control mean in each group. Values are the means ± SEM (n = 3), $^{**}p < 0.05$.

4 Discussion

The aim of this study was to investigate the effect of gas-controlled cyclic hydrostatic pressure alone on 2-dimensionally seeded dedifferentiated articular chondrocytes. We first developed a gas-controlled cyclic hydrostatic pressure loading system as gas control of the culture medium is important for cell culture. However, Parkkinen et al. reported PO_2 decreases of about 50% within 3 days in sealed systems [16]. Toyoda et al. also reported the difficulty of gas control under a pressure load [21]. Hansen et al. had a gas controlled system, but their peak load was very slight than that of physiological range normally occurring in the hip joint during daily activity [18,20]. Therefore, in this experiment we used a polyolefin bag from which gas infiltration as well as prevention of bacterial and viral infection were confirmed. The bag is already used for the self-storage of blood and for blood transfusions in the medical field. Medium exchange is possible in a part of the

nozzle also. The PO_2 and PCO_2 of the medium in the bag reached equilibrium in 24 h, and there was no significant change for 3 days afterwards. The PO_2 and PCO_2 gas pressure were very carefully controlled. Second, we used a serum-free medium under cyclic hydrostatic pressure loading because serum has many factors that affect chondrocyte metabolism. Thyroxine, one of the hormones in serum, has wide-ranging effects, including involvement in the processes of hypertrophy and endochondral ossification at the growth plate [27], which is undesirable for chondrogenic differentiation. Hence we used serum only at the dedifferentiation phase. Our serum-free medium was a modification of the protocol outlined by Mackay et al. [24]. The main difference was exclusion of dexamethasone and TGF-b. These 2 elements have been reported to affect chondrogenic differentiation in vitro [25,26]. In this experiment, we used 3-passage bovine chondrocytes. As described previously [11], the gene expression of type I collagen, type II collagen, and aggrecan of bovine chondrocytes cultured in monolayer was examined via Northern blot analysis. When cultured in a monolayer, the expression of the genes encoding type II collagen and aggrecan was weakened as the number of passages increased, and decreased dramatically after 2 passages. Meanwhile, the gene encoding type I collagen was detectable and strongly expressed after 2 passages, which indicated that bovine chondrocytes dedifferentiated after 2 passages. Hence we used 3-passage bovine chondrocytes as further dedifferentiated cells. In the present study, when cultured in monolayer, the expression of the type II collagen and aggrecan mRNA dramatically decreased after 3 passages. Meanwhile, the type I collagen mRNA was strongly expressed after 3 passages. These results indicated that the bovine chondrocytes dedifferentiated sufficiently after 3 passages. Hence we used 3-passage bovine chondrocytes as the dedifferentiated cells. After the 3 passages, dedifferentiated chondrocytes were seeded and cultured in chemically defined serum-free medium with ITS Premix for 3 days. A 3.5MPa cyclic hydrostatic pressure was then applied at 0.5Hz for 4 hours or 24 hours per day for 4 days. The magnitude and frequency of the applied pressure were chosen to be within the physiological range normally occurring in the hip joint during daily activity [20]. When dedifferentiated chondrocytes were cultured in serum-free medium under a cyclic hydrostatic pressure loading, semi-quantitative RT-PCR showed that the expression of aggrecan mRNA levels increased to 3-fold as a result of the cyclic hydrostatic pressure load ($p < 0.15$). Type II collagen mRNA levels also up-regulated to 2-fold as a result of the cyclic hydrostatic pressure load ($p < 0.15$). On the other hand, type I collagen mRNA levels were reduced by the cyclic hydrostatic pressure loading in a statistically significant manner ($p < 0.05$). Redifferentiation of dedifferentiated bovine articular chondrocytes was thought to be enhanced by the cyclic hydrostatic pressure load. The sensitivity of chondrocytes to hydrostatic pressure is well established [15,16,19,23,28]. However, there has been no report of a hydrostatic pressure effect on 2-dimensionally seeded dedifferentiated articular chondrocytes. Our results suggest that gas-controlled cyclic hydrostatic pressure

within the physiological range enhances the cartilaginous matrix formation of dedifferentiated chondrocytes in vitro. In the field of cell-based therapy, autologous chondrocyte transplantation is most commonly used for joint cartilage defects. In autologous chondrocyte transplantation, culture-expanded chondrocytes are transplanted under a cover of periosteum [1]. However, culture-expanded cells lead to dedifferentiation. Therefore this therapy can be used only to treat focal defects. Many more cells are required to treat a large defect, which is one of the limitations of autologous chondrocyte transplantation. P. Angele et al. showed that cyclic hydrostatic pressure enhances the cartilaginous matrix formation of mesenchymal progenitor cells differentiated in vitro [30]. These kinds of cell sources and our gas-controlled cyclic hydrostatic pressure loading system may resolve this limitation of autologous chondrocyte transplantation.

Acknowledgments

This work was supported by Grant-in-Aid for Scientific Research on Priority Areas 15086202 from the Ministry of Education, Cultures, Sports, Science and Technology of Japan.

References

1. Brittberg, M., Lindahl, A., Nilsson, A., Ohlsson, C., Isaksson, O., Peterson, L., 1994. Treatment of deep cartilage defects in the knee with autologous chondrocyte transplantation. N. Engl. J. Med. 331, 889-895.
2. Ochi, M., Uchio, Y., Kawasaki, K., Wakitani, S., Iwasa, J., 2002. Transplantation of cartilage-like tissue made by tissue engineering in the treatment of cartilage defects of the knee. J. Bone Joint Surg. Br. 84, 571-578.
3. Peterson, L., Minas, T., Brittberg, M., Lindahl, A., 2003. Treatment of osteochondritis dissecans of the knee with autologous chondrocyte transplantation: results at two to ten years. J. Bone Joint Surg. Am. 85-A Suppl 2, 17-24.
4. von der Mark, K., Gauss, V., von der Mark, H., Muller, P., 1977. Relationship between cell shape and type of collagen synthesized as chondrocytes lose their cartilage phenotype in culture. Nature 267, 531-531.
5. Benya, P.D., Shaffer, J.D. 1982. Dedifferentiated chondrocytes reexpress the differentiated collagen phenotype when cultured in agarose gels. Cell 30, 215-224.
6. Hauselmann, H.J., Fernandes, R.J., Mok, S.S., Schmid, T.M., Block, J.A., Aydelotte, M.B., Kuettner, K.E., Thonar, E.J., 1994. Phenotypic stability of bovine articular chondrocytes after longterm culture in alginate beads. J. Cell Sci. 107 (Pt 1), 17-27.

7. Yaeger, P.C., Masi, T.L., de Ortiz, J.L., Binette, F., Tubo, R., McPherson, J.M., 1997. Synergistic action of transforming growth factor-beta and insulin-like growth factor-I induces expression of type II collagen and aggrecan genes in adult human articular chondrocytes. Exp. Cell Res. 237, 318-325.
8. Martin, I., Vunjak-Novakovic, G., Yang, J., Langer, R., Freed, L.E., 1999. Mammalian chondrocytes expanded in the presence of fibroblast growth factor 2 maintain the ability to differentiate and regenerate three-dimensional cartilaginous tissue. Exp. Cell Res. 253, 681-688.
9. Jakob, M., Demarteau, O., Schafer, D., Hintermann, B., Dick, W., Heberer, M., Martin, I., 2001. Specific growth factors during the expansion and redifferentiation of adult human articular chondrocytes enhance chondrogenesis and cartilaginous tissue formation in vitro. J. Cell Biochem. 81, 368-377.
10. Grigolo, B., Lisignoli, G., Piacentini, A., Fiorini, M., Gobbi, P., Mazzotti, G., Duca, M., Pavesio, A., Facchini, A., 2002. Evidence or redifferentiation of human chondrocytes grown on a hyaluronan-based biomaterial (HYAff 11): molecular, immunohistochemical and ultrastructural analysis. Biomaterials 23, 1187-1195.
11. Chen, G., Sato, T., Ushida, T., Hirochika, R., Tateishi, T., 2003 Redifferentiation of dedifferentiated bovine chondrocytes when cultured in vitro in a PLGA-collagen hybrid mesh. FEBS Lett. 542, 95-99.
12. Malda, J., van Blitterswijk, C.A., Grojec, M., Martens, D.E., Tramper, J., Riesle, J., 2003. Expansion of bovine chondrocytes on microcarriers enhances redifferentiation. Tissue Eng. 9, 939-948.
13. Smith, R.L., Carter, D.R., Schurman, D.J., 2004. Pressure and shear differentially alter human articular chondrocyte metabolism: a review. Clin. Orthop. Relat. Res. S89-95.
14. Lippiello, L., Kaye, C., Neumata, T., Mankin, H.J., 1985. In vitro metabolic response of articular cartilage segments to low levels of hydrostatic pressure. Connect. Tissue Res. 13, 99-107.
15. Hall, A.C., Urban, J.P., Gehl, K.A., 1991. The effects of hydrostatic pressure on matrix synthesis in articular cartilage. J. Orthop. Res. 9, 1-10.
16. Parkkinen, J.J., Ikonen, J., Lammi, M.J., Laakkonen, J., Tammi, M., and Helminen, H.J., 1993. Effects of cyclic hydrostatic pressure on proteoglycan synthesis in cultured chondrocytes and articular cartilage explants. Arch. Biochem. Biophys. 300, 458-465.
17. Smith, R.L., Rusk, S.F., Ellison, B.E., Wessells, P., Tsuchiya, K., Carter, D.R., Caler, W.E., Sandell, L.J., Schurman, D.J., 1996. In vitro stimulation of articular chondrocyte mRNA and extracellular matrix synthesis by hydrostatic pressure. J. Orthop. Res.14, 53-60.
18. Hansen, U., Schunke, M., Domm, C., Ioannidis, N., Hassenpflug, J., Gehrke, T., Kurz, B., 2001. Combination of reduced oxygen tension and intermittent

hydrostatic pressure: a useful tool in articular cartilage tissue engineering. J. Biomech. 34, 941-949.
19. Toyoda, T., Seedhom, B.B., Kirkham, J., Bonass, W.A., 2003. Upregulation of aggrecan and type II collagen mRNA expression in bovine chondrocytes by the application of hydrostatic pressure. Biorheology 40, 79-85.
20. Hodge, W.A., Fijan, R.S., Carlson, K.L., Burgess, R.G., Harris, W.H., Mann, R.W., 1986. Contact pressures in the human hip joint measured in vivo. Proc. Natl. Acad. Sci. USA 83, 2879-2883.
21. Toyoda, T., Seedhom, B.B., Yao, J.Q., Kirkham, J., Brookes, S., Bonass, W.A., 2003. Hydrostatic pressure modulates proteoglycan metabolism in chondrocytes seeded in agarose. Arthritis Rheum. 48, 2865-2872.
22. Carver, S.E., Heath, C.A., 1999. Semi-continuous perfusion system for delivering intermittent physiological pressure to regenerating cartilage. Tissue Eng. 5, 1-11.
23. Mizuno, S., Tateishi, T., Ushida, T., Glowacki, J., 2002. Hydrostatic fluid pressure enhances matrix synthesis and accumulation by bovine chondrocytes in three-dimensional culture. J. Cell Physiol. 193, 319-327.
24. Mackay, A.M., Beck, S.C., Murphy, J.M., Barry, F.P., Chichester, C.O., Pittenger, M.F., 1998. Chondrogenic differentiation of cultured human mesenchymal stem cells from marrow. Tissue Eng. 4, 415-428.
25. Quarto, R., Campanile, G., Cancedda, R., Dozin, B., 1992. Thyroid hormone, insulin, and glucocorticoids are sufficient to support chondrocyte differentiation to hypertrophy: a serumfree analysis. J. Cell Biol. 119, 989-995.
26. Johnstone, B., Hering, T.M., Caplan, A.I., Goldberg, V.M., Yoo, J.U., 1998. In vitro chondrogenesis of bone marrowderived mesenchymal progenitor cells. Exp. Cell Res. 238, 265-272.
27. Ballock, R.T., Reddi, A.H., 1994. Thyroxine is the serum factor that regulates morphogenesis of columnar cartilage from isolated chondrocytes in chemically defined medium. J. Cell Biol. 126, 1311-1318.
28. Ikenoue, T., Trindade, M.C., Lee, M.S., Lin, E.Y., Schurman, D.J., Goodman, S.B., Smith, R.L., 2003. Mechanoregulation of human articular chondrocyte aggrecan and type II collagen expression by intermittent hydrostatic pressure in vitro. J. Orthop. Res. 21, 110-116.
29. Tallheden, T., Bengtsson, C., Brantsing, C., Sjogren-Jansson, E., Carlsson, L., Peterson, L., Brittberg, M., Lindahl, A., 2005. Proliferation and differentiation potential of chondrocytes from osteoarthritic patients. Arthritis Res. Ther. 7, R560-568.
30. Angele, P., Yoo, J.U., Smith, C., Mansour, J., Jepsen, K.J., Nerlich, M., Johnstone, B., 2003. Cyclic hydrostatic pressure enhances the chondrogenic phenotype of human mesenchymal progenitor cells differentiated in vitro. J. Orthop. Res. 21, 451-457.

EFFECTS OF A SHEAR FLOW AND WATER FILTRATION ON THE CELL LAYER OF A HYBRID VASCULAR GRAFT

X. HE AND T. KARINO

Research Institute for Electronic Science, Hokkaido University,
North 12, West 6, North District, Sapporo 060-0812, Japan
E-mail: karino@es.hokudai.ac.jp

It has been shown that in humans, atherosclerotic lesions and intimal hyperplasia develop preferentially in regions where flow is disturbed by the formation of slow secondary and recirculation flows, and where wall shear stress is low. However, the precise mechanisms of localization of these vascular diseases still remain unelucidated. With respect to this, we have previously proposed a hypothesis, that is, flow-dependent concentration polarization theory, to explain the localization of vascular diseases including atherosclerosis, anastomotic intimal hyperplasia, and formation of cerebral aneurysms. The present study was carried out to substantiate the hypothesis. To do so, we prepared a hybrid vascular graft as a model of an artery and subjected the cells to a laminar shear flow for 28 days and tested how the proliferation of the cells forming an arterial wall is affected by a shear flow and water filtration that cause concentration polarization of macromolecules including low density lipoproteins (LDLs). The results indicate that slow flows that impose low wall shear stresses on endothelial cells promote the growth and proliferation of smooth muscle cells located right underneath of them as it occurs in vivo. Addition of water filtration flow that causes concentration polarization of macromolecules such as LDL and VLDL at the luminal surface of endothelium and also facilitates transport of substances dissolved in blood including some nutiment further enhances the growth and proliferation of smooth muscle cells.

1 Introduction

Atherosclerotic lesions develop as a result of accumulation of an excessive amount of low-density lipoproteins (LDL: a carrier of cholesterol) between the endothelium, the innermost layer of a blood vessel wall, and the internal elastic lamina that lies underneath of it. As the results of extensive flow studies carried out hitherto, it was shown that in humans the vascular disease develops preferentially in regions where flow is slow and wall shear stress is low [1-3]. However, the precise mechanism of the pathogenesis and localization of the disease is still not well understood. With respect to this, we have previously proposed a hypothesis (flow-dependent concentration polarization theory) for the localization of vascular diseases including atherosclerosis, anastomotic intimal hyperplasia, and formation of cerebral aneurysms in which we explained that due to the particular nature of an arterial wall which allows the filtration of water but not macromolecules such as lipoproteins including LDL, enrichment of LDL occurs at the luminal surface of the vessel wall, and the surface concentration of LDL varies as a function of the velocity of flowing blood [4-5]. Since then, to substantiate the hypothesis, we have been carrying on further studies both theoretically by means of Computational Fluid Dynamics [6-7]

and experimentally by using cultured vascular endothelial cells [8-9]. We confirmed experimentally that, in the presence of water filtration flow, and only in the presence of it, the surface concentration of LDL increases and decreases, respectively, with decreasing and increasing the flow velocity hence wall shear rate (shear stress) as predicted by our theory [8]. However, it is not known how the filtration of water itself that facilitates transport of substances dissolved in blood including some nutriment and the concentration or depletion of LDL that occurs as a result of water filtration affect the proliferation of cells constituting the vessel wall. Therefore we prepared a hybrid vascular graft as a model of an artery which allowed the filtration of water in the same manner as intact arteries in vivo, and by carrying out flow studies using it, we tested the effects of a laminar shear flow and water filtration on proliferation of the cells in the cell layer of the hybrid graft.

2 Materials and Methods

2.1 Materials

Bovine aortic endothelial cells (ECs) and smooth muscle cells (SMCs) were purchased from Cell Systems, Inc. (Kirkland, WA, USA) and Cell Applications, Inc. (San Diego, CA, USA), respectively. Fetal calf serum (FCS) was purchased from Trace Scientific Co. Ltd. (Melbourne, Australia). Ascorbic acid, fibronectin, penicillin, streptomycin, and Iscov's modified Dulbecco's medium (IMDM) were obtained from Sigma-Aldrich Co. (St. Louis, MO, USA). Expanded PTFE artificial vascular graft was purchased from IMPRA, Inc. (Tempe, AZ, USA).

2.2 Methods

2.2.1 Preparation of a hybrid vascular graft

At first, bovine aortic smooth muscle cells (SMCs) and endothelial cells (ECs) were cultivated separately in culture dishes with Iscove's modified Dulbecco's medium (IMDM) containing fetal calf serum (FCS) at 10% by volume, 100 IU/ml penicillin, 100 μg/ml streptomycin at 37°C in 5% CO_2 and 95% air humidified atmosphere, and the cells at passages of 5~11 were used to prepare a hybrid vascular graft.

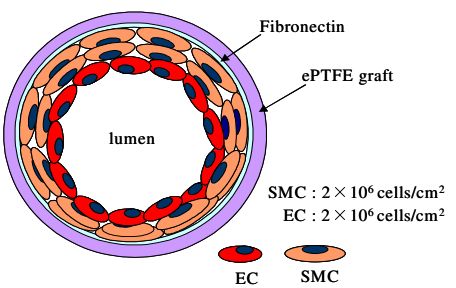

Figure 1. Schematic representation of a hybrid vascular graft showing the relative location and arrangement of smooth muscle cells (SMCs) and endothelial cells (ECs) within an water-permeable expanded PTFE artificial vascular graft.

After obtaining sufficient number of SMCs, the cells were released from the culture dish with a trypsin-EDTA solution, and after centrifugation, the cells were suspended in IMDM containing FCS at 20% by volume, 100 IU/ml penicillin, 100 μg/ml streptomycin, 2.5 mg/ml amphotericin B, and 50 μg/ml ascorbic acid. The SMCs were seeded onto the inner surface of a 3.0-mm i.d., 30-mm-long expanded PTFE graft which was treated with 70% ethanol and coated with an adhesive molecule, 0.01% fibronectin, at a cell density of 2×10^6 cells/cm^2 by means of a pressure infusion of a suspension of SMCs using a syringe and they were cultivated for 4 days in 40 ml of the same culture medium as that used to seed the SMCs at 37°C in 5% CO_2 and 95% air humidified atmosphere by changing the medium every other day. Then, ECs were seeded directly over the SMCs in the same manner as that of SMCs as shown schematically in Fig. 1, and they were co-cultivated for 5 days in the same culture medium by changing the medium every other day until the ECs became confluent and completely covered the SMCs, forming a hybrid vascular graft. The hybrid graft was then exposed to a hydrostatic pressure of 80 mmHg for 10 days to promote the proliferation of the cells since we knew from our experience that SMCs grew better under hydrostatic pressures of 80-100 mmHg.

2.2.2 *Perfusion culture of the cells of a hybrid graft*

The hybrid graft was installed as a part of a steady flow perfusion culture system shown in Fig. 2, filled with a culture medium the same as that used to prepare the hybrid graft, and cultivated the cells for 28 days exposing the ECs forming the innermost layer of the hybrid graft to a shear stress of either 2 or 14 or 30 dynes/cm^2

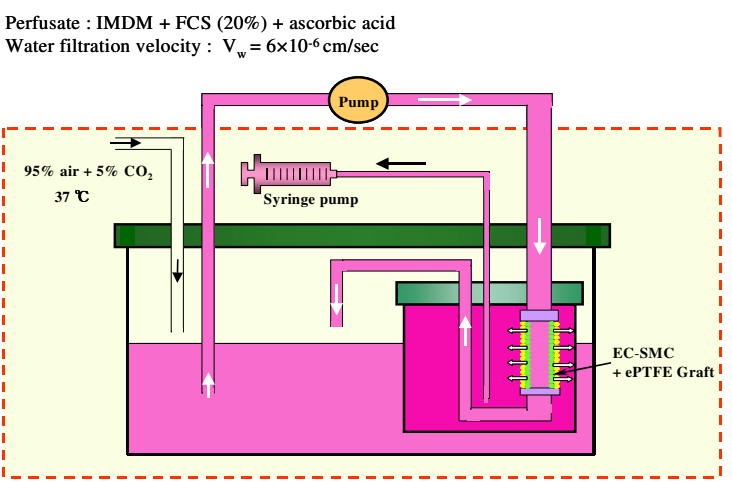

Figure 2. Schematic representation of a steady flow perfusion culture system used in the present study. A cell culture medium was re-circulated with a steady flow pump, and an water filtration flow was generated by using a syringe pump.

in the presence or absence of water filtration with a filtration velocity of 6×10^{-6} cm/sec generated by a syringe pump. Here the mean wall shear stress was calculated by the use of the Hagen-Poiseuille equation:

$$\tau_w = \frac{4}{\pi}\mu\frac{Q}{r^3}$$

where μ is the viscosity of the perfusate (culture medium, $\mu = 8.3 \times 10^{-3}$ Poise), Q is the volume flow rate of the perfusate [cm^3/sec], and r is the radius of the vessel [cm]. Water filtration velocity was calculated by dividing the filtration flow, Q_w, [cm^3/sec] by the inner surface area of the hybrid graft, $2\pi r_0 L$ [cm^2], where r_0 and L are, respectively, the inner radius and the length of the hybrid graft.

2.2.3 Measurements of the thickness of the cell layer and the number of the cells

After finishing the flow experiment, the graft was removed from the ferfusion culture system and it was fixed with a solution of 4% formaldehyde for 24 hours. The 30-mm-long graft was cut at locations 7, 15, and 23 mm from the inlet of the graft, and they were enbedded in paraffin. Then 5-μm thick histological specimens were cut out from these segments close to the above locations, stained with hematoxylin-eosin. These were referred proximal, middle, and distal sections, and observed with a transmission light microscope and photographed at six different locations along the inner circumference of the graft. From the photographs of the crosssections of the graft, the thickness of the cell layer and the number of cells per 10,000 μm^2 were measured by using a computer software for picture analyses (Adobe Photoshop Version 5) and mean values were obtained.

2.2.4 Statistical analysis

The results were expressed as a mean ± SD. The values of the thicknesses of the cell layer and the number of cells measured at 6 different locations along the inner circumference of the graft and from 3 sets of experiments were used to perform student's *t*-test to assess the significance of difference. Differences at $p < 0.05$ were considered to be statistically significant.

3 Results

3.1 Gross observation of harvested grafts

Figure 3 shows representative photographs of hematoxylin-eosin-stained histological specimens of the hybrid grafts obtained by cultivating the cells for 28 days in the presence of a steady shear flow which imposed shear stresses of 2, 14, and 30 dynes/cm^2 on ECs in the presence (A: upper panel) and absence (B: lower panel) of water filtration with a filtration velocity of 6×10^{-6} cm/sec. From these

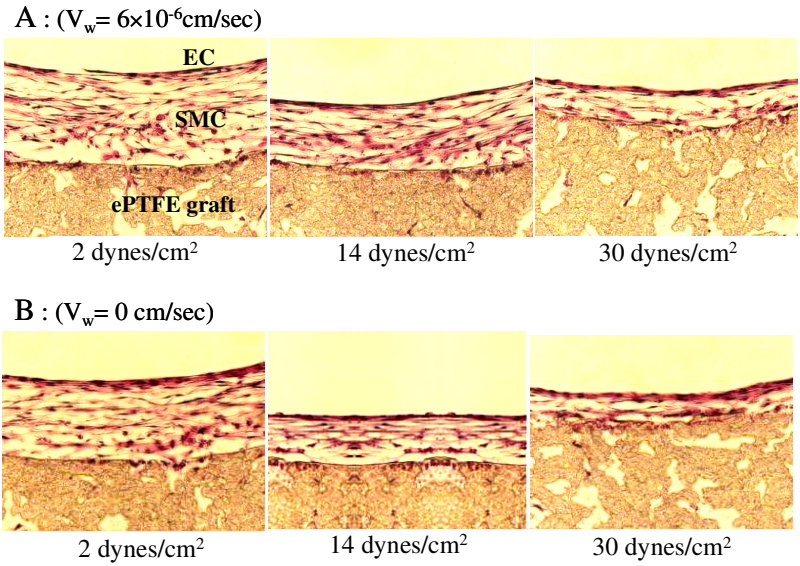

Figure 3. Representative photographs of histological specimens of hybrid vascular grafts exposed to 3 different levels of steady laminar shear flows for 28 days, showing gross structure and thickness of the cell layer that was composed of a monolayer of endothelial cells and a large number of smooth muscle cells and intercellular matrices. A: in the presence of water filtration with a physiologic filtration velocity of 6×10^{-6} cm/sec. B: in the absence of water filtration. Original magnification: ×200.

photographs, it was confirmed that it is possible to prepare a hybrid vascular graft with a fairly uniform thickness by seeding SMCs and ECs by means of pressure infusion of their suspensions using a syringe and co-cultivating them. It is also possible to maintain the cells viable in the presence of a shear flow as long as four weeks. As evident from the photographs, it was found that in all the cases the cell layer was composed of a monolayer of endothelial cells forming the innermost layer of the cell layer and a large number of smooth muscle cells under it. The structure of the cell layers was the same in all the vessels even though they were exposed to different levels of shear stress. However, as evident from the photographs, the cell layer exposed to a low shear flow (low shear stress) was markedly thicker than that exposed to a high shear flow (high shear stress).

3.2 Effects of a shear flow and water filtration on the thickness of the cell layer

From the photographs of histological specimens of three sets of hybrid grafts, measurements of the thickness of the cell layer were carried out at three locations along the axis of the graft, that is, proximal, middle, and distal sites. Figures 4 and 5 show, respectively, the results obtained in the presence and absence of water filtration. Comparisons of mean values are shown in Fig. 6. Calculated mean values

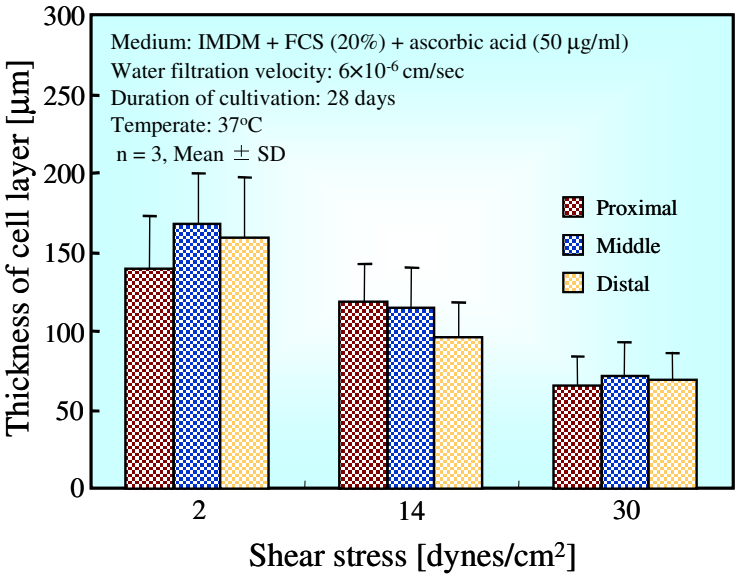

Figure 4. Measured thickness of the cell layer of hybrid vascular grafts cultivated by exposing the cells to 3 different levels of shear flow in the presence of water filtration.

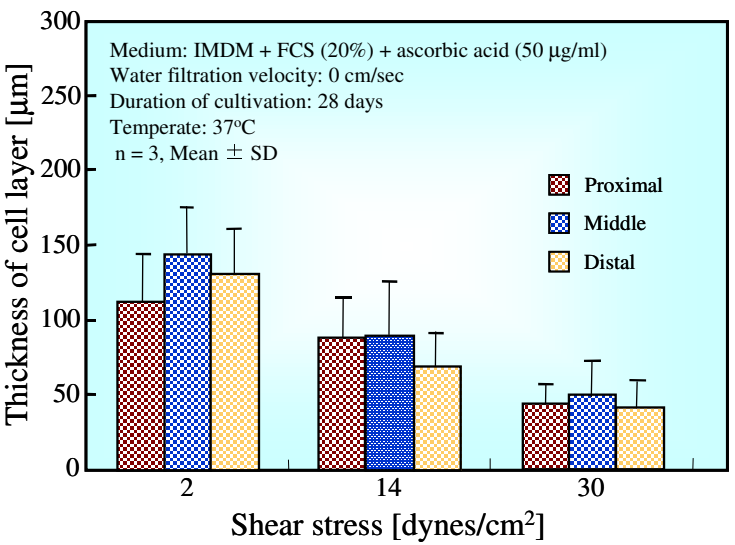

Figure 5. Measured thickness of the cell layer of hybrid vascular grafts cultivated by exposing the cells to 3 different levels of shear flow in the absence of water filtration.

of the thickness of the cell layer obtained from three grafts exposed to a shear flow in the presence of water filtration were 156, 110, and 68 μm, respectively, at a shear stress of 2, 14, and 30 dynes/cm^2. The corresponding values obtained from grafts exposed to a shear flow in the absence of water filtration were 130, 83, and 45 μm. The difference between the thickness of the cell layer obtained in the presence and absence of water filtration was found to be statistically significant ($p < 0.01$) at all the three levels of shear stresses.

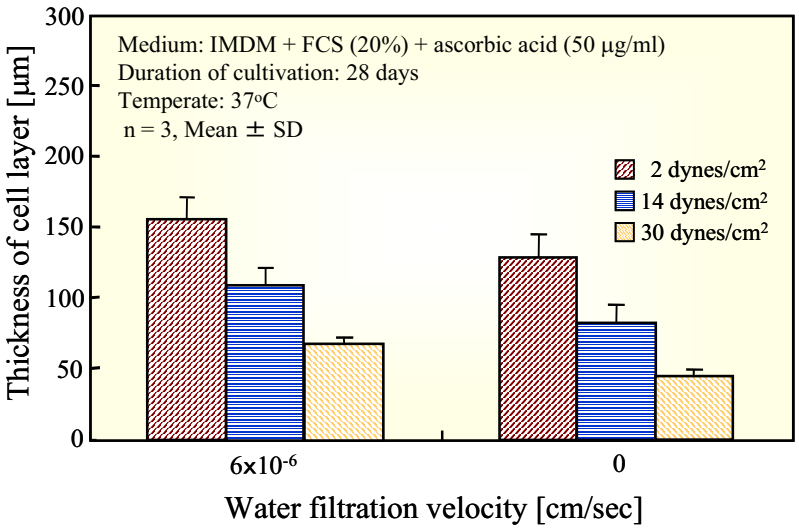

Figure 6. Comparison of mean values of measured thickness of the cell layer of hybrid vascular grafts cultivated by exposing the cells to 3 different levels of shear flows in the presence and absence of water filtration.

3.3 Effects of a shear flow and water filtration on the number of cells

Figure 7 shows the effect of a shear flow and water filtration on the number of the cells in the cell layer exposed to a shear flow for 28 days in the presence and absence of water filtration. The mean numbers of the cells were 43, 36, and 25 per 10,000 μm^2, respectively, at a shear stress of 2, 4, and 30 dynes/cm^2 in the presence of water filtration. The corresponding values in the absence of water filtration were 33, 28, and 22 per 10,000 μm^2. Comparison of the values at each level of shear stress showed that the number of cells in the cell layer of the graft exposed to a shear flow in the presence of water filtration was greater than that of the cell layer exposed to a shear flow in the absence of water filtration. However, statistically speaking, there was no significant difference between them at any level of shear stress.

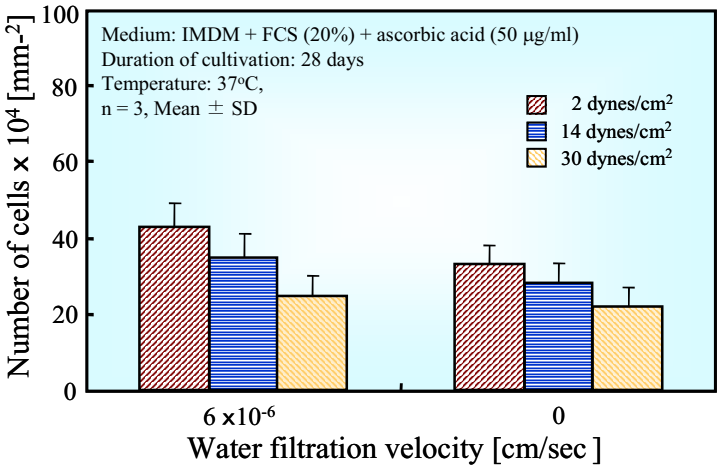

Figure 7. Comparison of mean values of the number of the cells in the cell layer of hybrid vascular grafts cultivated by exposing the cells to 3 different levels of shear flows in the presence and absence of water filtration.

4 Discussion

The effect of blood flow on the development of intimal hyperplasia has been studied by many investigators by carrying out vein graft interpositions in animals and creating poor distal runoff by ligating several distal arteries. They showed that intimal hyperplasia develops the slower the flow velocity (the lower the shear rate) [10-14] and the higher the concentration of lipoproteins in blood [15]. They also reported that the degree of intimal thickening that occurs in autologous vein grafts is lower than that occurs in artificial grafts [16], and in the case of autologous arterial grafts such as the internal mammary artery, gastric artery, and radial artery, intimal thickening hardly occurs [17, 18]. Furthermore, with regard to artificial grafts, it has been reported that the lower the porosity, the lower the degree of intimal thickening [19], and in the case of nonporous grafts, intimal thickening does not occur at all [20]. From our point of view, all these phenomena mentioned above indicate that the lower the permeability of the wall of a graft to water, the lower the degree of intimal thickening formed in the graft.

In our present paper, we attempted to do similar study by carrying out *ex vivo* perfusion culture of the cells of a hybrid vascular graft. As the results, we found almost the same phenomena that slow flows (low shear stress) and water filtration promote the proliferation of the cells forming a hybrid vascular graft. The results strongly support our hypothesis that, in our arterial system, due to the presence of a filtration flow of water, concentration of LDL occurs at the luminal surface in regions of slow flow (low wall shear stress), thus augmenting the uptake of LDL by

the cells located at such sites, leading to its accumulation in subendothelial spaces and eventual localized genesis and development of intimal hyperplasia and atherosclerosis at such sites.

As described above, the results we obtained were quite the same as those obtained by others in animal studies. This means that the hybrid vascular graft we prepared can be used as a good model of an artery, and together with the flow system we set up, it could be used to study the effects of flow and water filtration on various biological and biochemical functions of the cells forming the vessel wall. The advantages of such an *ex vivo* perfusion study are that the vessels are kept under well-controlled and reproducible hemodynamic and environmental conditions such as the flow rate, pressure, oxygen and carbon dioxide tensions, and temperature. However, there is one big problem in carrying out long-term perfusion culture experiments successfully that it is very difficult to avoid contaminations by bacteria and fungi.

5 Conclusions

In the present study, we attempted first to construct a hybrid vascular graft by seeding bovine aortic smooth muscle cells and endothelial cells on the luminal surface of an expanded PTFE graft and co-cultivating them. Then by exposing the hybrid graft to 3 different levels of shear flows for a duration of 28 days in the presence and absence of water filtration, we tested the effects of a shear flow and water filtration on the structure and thickness of the cell layer. The following conclusions were drawn from this study:

1. It is possible to construct a hybrid vascular graft with a cell layer very much similar to that of an artificial graft implanted in vivo, that is, a pseudo intima composed of a monolayer of endothelial cells and a thick layer of smooth muscle cells and intercellular matrices.
2. It is possible to maintain the cells of the hybrid graft viable in the presence of a shear flow and water filtration for a duration of 4 weeks, and study the effects of these factors on various biological and biochemical functions of the cells including their proliferation observed in the present study.
3. Slow flows and water filtration promote the growth and proliferation of smooth muscle cells located right underneath of the endothelium, resulting in the formation of a thick layer of cells in the graft.

Acknowledgments

This work was supported by Grant-in-Aid for Scientific Research on Priority Areas 15086201 from the Ministry of Education, Culture, Sports, Science and Technology of Japan.

References

1. Caro, C.G., Fitz-Gerald, J.M., Schroter, R.C., 1971. Atheroma and arterial wall shear. Observation, correlation and proposal of a shear dependent mass transfer mechanism for atherogenesis. Proc. Roy. Soc. Lond. B177, 109-159.
2. Zarins, C.K., Giddens, D.P., Bharadvaj, B.K., Sottiurai, V.S., Mabon, R.F., Glagov, S., 1983. Carotid bifurcation atherosclerosis. Quantitative correlation of plaque localization with flow velocity profiles and wall shear stress. Circ. Res. 53, 502-514.
3. Asakura, T., Karino, T., 1990. Flow patterns and spatial distribution of atherosclerotic lesions in human coronary arteries. Circ. Res. 66, 1045-1066.
4. Wada, S., Karino, T., 1999. Theoretical study on flow-dependent concentration polarization of low density lipoproteins at the luminal surface of a straight artery. Biorheology 36, 207-23.
5. Wada, S., Karino, T., 2002. Prediction of LDL concentration at the luminal surface of a vascular endothelium. Biorheology 39, 331-36.
6. Wada, S., Karino, T., 2002. Theoretical prediction of low-density lipoproteins concentration at the luminal surface of an artery with a multiple bend. Ann. Biomed. Eng. 30, 778-791.
7. Wada, S., Koujiya, M., Karino, T., 2002. Theoretical study of the effect of local flow disturbances on the concentration of low-density lipoproteins at the luminal surface of end-to-end anastomosed vessels. Med. Biol. Eng. Comput. 40, 576-87.
8. Naiki, T., Sugiyama, H., Tashiro, R., Karino, T., 1999. Flow-dependent concentration polarization of plasma proteins at the luminal surface of a cultured endothelial cell monolayer. Biorheology 36, 225-241.
9. Naiki, T., Karino, T., 2000. Visualization of flow-dependent concentration polarization of macromolecules at the surface of a cultured endothelial cell monolayer by means of fluorescence microscopy. Biorheology 37, 371-384.
10. Morinaga, K., Eguchi, H., Miyazaki, T., Okadome, K., Sugimachi, K., 1987. Development and regression of intimal thickening of arterially transplanted autologous vein grafts in dogs. J. Vasc. Surg. 5, 719-730.
11. Kraiss, L.W., Kirkman, T.R., Kohler, T.R., Zieler, B., Clowes, A.W., 1991. Shear stress regulates smooth muscle proliferation and neointimal thickening in porous polytetrafluoroethylene grafts. Arterioscler. Thromb. 11, 1844-1852.
12. Mattsson, E.J.R., Kohler, T.R., Vergel, S.M., Clowes, A.W., 1997. Increased blood flow induces regression of intimal hyperplasia. Arterioscler. Thromb. Vasc. Biol. 17, 2245-2249.
13. Meyerson, S.R., Skelly, C.R., Curi, M.A., Shakur, U.M., Vosicky, J.E, Glagov, S., Schwartz, L.B., 2001. The effects of extremely low shear stress on cellular proliferation and neointimal thickening in the failing bypass graft. J. Vasc. Surg. 34, 90-97.

14. Verceli, S.A., Devies, M.G., Kenagy, R.D., Clowes, A.W., 2002. Flow-induced neointimal regression in baboon polytetrafluoroethylene grafts is associated with decreased cell proliferation and increased apoptosis. J. Vasc. Surg. 36, 1248-1255.
15. Hoff, H.F., Beck, G.J., Skibinski, C.I., Jürgens, G., O'Neil, J., Kramer, J., Lytle, B., 1988. Serum Lp(a) level as a predictor of vein graft stenosis after coronary artery bypass surgery in patients. Circulation 77, 1238-1244.
16. DeWeese, J.A., 1978. Anastomotic intimal hyperplasia. In: Sawyer, P.N., Kaplitt, M.J. (Eds.), Vascular grafts. Appleton-Century-Crofts, New York, pp. 147-152.
17. Cameron, A., Kemp, H.G., Green, G.E., 1986. Bypass surgery with the internal mammary artery graft: 15 year follow-up. Circulation 74 (Suppl III), 111-130.
18. Grondin, C.M., Campeau, L., Lesperance, J., Enjalbert, M., Bourassa, M.G., 1984. Comparison of late changes in internal mammary artery and saphenous vein grafts in two consecutive series of patients 10 years after operation. Circulation 70 (Suppl. 1), I-208-212.
19. Campbell, C.D., Goldfarb, D., Roe, R., 1975. A small arterial substitute: Expanded microporous polytetrafluoroethylene: patency versus porosity. Ann. Surg. 182, 138-143.
20. Hunter, G.C., Carson, S.N., Wong, H.N., French, S., 1980. Experimental small-diameter graft patency: Effect of compliance, porosity and graft healing potential. Curr. Surg. 37, 439-441.

TISSUE RECONSTRUCTIONS FOR MOTOR ORGANS WITH MECHANICALLY STRUCTURED GRAFTS

K. TAKAKUDA

Institute of Biomaterials and Bioengineering, Tokyo Medical and Dental University, 2-12-1 Kanda-Surugadai,Chiyoda-ku, Tokyo 101-0062, Japan
E-mail: takakuda.mech@tmd.ac.jp

Regeneration of tissue is a challenging problem in many current investigations but common strategy of cell transplantations has not yet yielded meaningful achievement in the fields of locomotory organs. This would be attributed to the fact that these tissue required suitable biomechanical stimuli for regeneration and maturation. In this study, therefore, various micro-structured devices or grafts for guided tissue regeneration in motor organs were investigated. The first one was the device for the reconstruction of Sharpey's fibers. The mesh structure was placed on the surface of the device, and which structure enabled the collagen fibers from surrounding tissues to be anchored on the device. Similarly the technique for anchoring the fibrous materials to bones was studied. The bone tissues were induced within the spaces between the fibrous materials and the mechanical anchoring to tissues was realized. For the reconstruction of small arteries, compliance mismatch is the major cause of early obstruction. Hence acellular scaffolds from rat's abdominal aorta was developed and implanted to reconstruct rat's carotid artery. Without any cell seeding, the grafts were patent and their inner lumen was covered with endothelial cells after implantation. The fourth grafts were for the regeneration of peripheral nerves. The bioabsorbable nerve guides was developed. Bellows shape was adopted which enables the tubes to flex and keep the inner cavity for the space of nerve regeneration. Combining the filling of fibrin gel for cell adhesion, enhanced regeneration of nerves was demonstrated.

1 Introduction

Regeneration of tissue has been attracting many interests recently. Commonly adopted strategy in them is that of cell transplantations with suitable scaffolds. Such strategy has been successful in certain fields, however, has not yet yielded successful achievement in the fields of locomotory organs. This difference should be attributed to the fact that the tissue in locomotory organs requires suitable biomechanical stimuli for regeneration and maturation. In this study, therefore, the micro-structured grafts or devices for guided tissue regeneration in motor organs were investigated. These grafts would provide the suitable environments for cells and guide them to regenerate the tissues.

In the investigation, animal study was carried out to elucidate the validity of the developed grafts. All animal experiments were conducted in accordance with the guidelines set by the Animal Experiment Committee of the Tokyo Medical and Dental University. Among the many attempts experimented, here reported were four representative cases of trials. They were, (1) reconstruction of Sharpey's fibers - attachment of soft fibrous tissues to hard artificial materials, (2) reconstruction of

insertion sites for ligaments - attachment of soft fibrous artificial materials to bone tissues, (3) reconstruction of small diameter arteries - supply of nutrient required for regeneration of bone tissues, and (4) regeneration of peripheral nerves - recovery of motor control.

2 Reconstruction of Sharpey's Fibers — Attachment of Soft Fibrous Tissues to Hard Artificial Materials

2.1 Materials and methods

Attachment of soft fibrous tissues to artificial materials is most desirable in such clinical applications as percutaneous devices and dental implants [1]; however, it still remains as one of the most difficult tasks to achieve, whereas the attachment of bone tissues to artificial materials is already possible with the use of such materials as hydroxyapatite [2]. Mesh structure, instead of structure using simple porous materials, would be a possible candidate to realize the thin interface for the attachment of fibrous tissues as shown in Fig. 1.

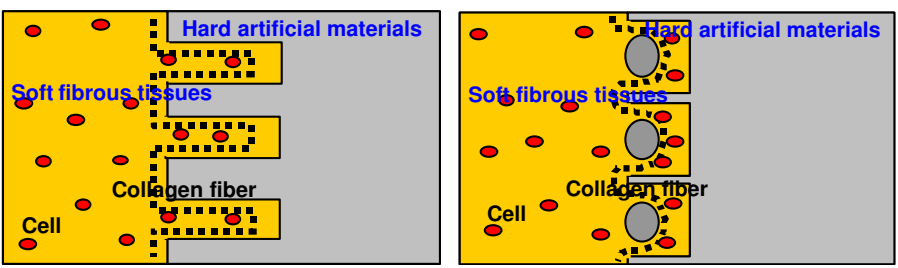

Figure 1. Left: Utilization of a simple porous surface of hard materials does not provide anchoring points for collagen fibers from surrounding soft fibrous tissues and cannot realize the mechanical attachment. Right: Mesh structure placed on the surface of the hard materials provides the anchoring points for the collagen fibers and mechanical attachment is realized.

A PMMA cylinder of 12-mm external diameter, 8-mm internal diameter, and 5-mm height was prepared, and on which lateral surface the 2-mm depth and 3-mm width groove was machined. Over the groove, one of 5 kinds of nylon mesh, the mesh spacing ranged from 28 to 523 μm was adhered as to cover the groove. Male SD rats of 8 weeks old were used for animal experiment. The cylinder specimen was implanted into the subcutaneous tissues of rats as shown in Fig. 2. The specimens were retrieved with surrounding tissues 4 weeks after surgery, and they were evaluated by mechanical test and histological observation.

Figure 2. Implantation of the specimen equipped with mesh structure on its lateral surface. The specimen was implanted into the subcutaneous tissues of the rat's back where the specimen was placed so as the mesh surface was perpendicular to the alignment of collagen fibers of surrounding subcutaneous tissues.

2.2 Results and discussion

The attachment strengths of the cylinder specimens to the surrounding tissues are measured and shown in Fig. 3. The attachment strength took the greatest value in the 200-µm mesh spacing group, and the smallest in the 28-µm mesh spacing group. The tendency of increase in the strength was observed accompanying the increase of mesh spacing till it reached 200 µm, whereas the strength decrease as the mesh spacing increased to 500 µm.

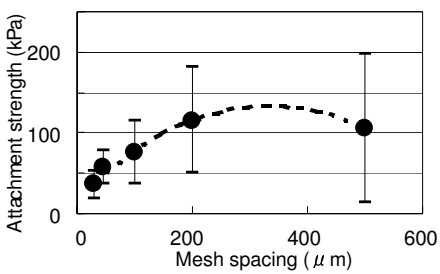

Figure 3. The attachment strength of cylinder specimens to the surrounding tissues. One-way ANOVA demonstrated the statistically significant effect of mesh spacing on the mean attachment strength ($p < 0.01$). Multiple comparison based on Scheffe's test demonstrated the statistically significant difference ($p < 0.01$) between the 200-µm and 28-µm spacing groups, while no difference between other pairs.

Typical histological observations of the cylinder specimens are shown in Fig. 4. In the case of 100-µm mesh spacing (left), mature collagen fibers were either capsulating a mesh fiber or align parallel to the mesh surfaces, and no fibers entering between the mesh fibers were observed. However, in the cases of 200-µm mesh spacing (right), collagen fibers coming from surrounding soft tissues and entering into the spacing between the mesh fibers were observed. Furthermore, in the cases of 200-µm mesh spacing, collagen fibers coming from surrounding soft tissues, entering the space between the mesh fibers, turning around a fiber and going back to the surrounding soft tissues were observed. In the cases of 500-µm mesh spacing, although collagen fibers entering between mesh fibers were observed, they are rather poor compared to the 100-µm and 200-µm mesh spacing specimens.

Thus the possibility of the mechanical attachment of soft fibrous tissues to artificial devices was suggested with the use of the mesh structure constructed on the surface of the device. The mesh structure would suitably be utilized for the

anchorage of the collagen fibers from the soft tissues. Within the scope of the present experiment, the mesh spacing about 200 µm was favorable for the anchorage of collagen fibers. Although further improvement in the structure and the verification of long term performance are necessary, the technology for mechanical attachment developed here might be advantageously utilized in the applications of the various kinds of medical and dental devices.

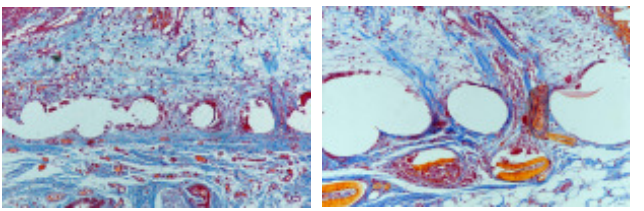

Figure 4. Histological observation around the mesh structure placed on the surface of the specimens. Azan staining. Mesh spacing was 100 µm (left), and 200 µm (right) respectively.

3 Reconstruction of Insertion sites for Ligaments — Attachment of Soft Fibrous Artificial Materials to Bone Tissues

3.1 Materials and methods

One of the most difficult problems to be solved for the development of artificial ligaments is the realization of the biological fixation of the ligament to the bone [3]. Although the natural ligament is attached to the bone with a structure composed of ligament/cartilage/bone tissues and tensile stresses are transmitted by the Sharpey's fibers, artificial ligament do not have such structure and fixed by the mechanical devices such as the screws and staples. Hence the biological fixation in which fibrous materials were fixed to bone by the induction of bone between the fibers as shown in Fig. 5 was desirable.

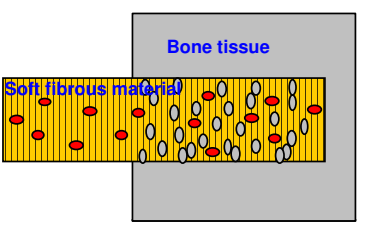

Figure 5. Fixation of soft fibrous artificial materials to bone tissue. The soft fibrous material for artificial ligament was inserted into the bone tunnel for the fixation. The biological fixation between them will be realized if bone tissues were induced in the space among the fibers.

The specimens prepared were 40-mm in length, 5-mm width, 0.6-mm thickness, and made of polyester nonwoven fabrics. Those in the experimental group were coated with chitin/chitosan. (1.4 mg/cm^2), and those in the control group were bare fabrics. These fabrics were generous gifts from Meiji Seika, LTD. Animal

experiments were carried out with 8-weeks old male SD rats. The specimen was implanted as shown in Fig. 6, and retrieved for the mechnical and histological evaluation 2 or 4 weeks after syrgery.

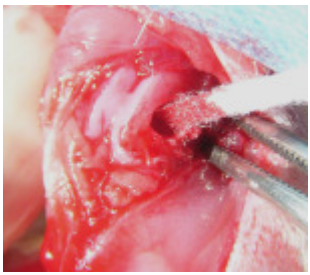

Figure 6. Implantation of the specimens. The hole of 3.5-mm diameter and 5-mm depth was created at the distal part of rat's femur. One end of the specimen of nonwoven fabrics was inserted into the hole and the other end was fixed to the soft tissue around the hole.

3.2 Results and discussion

The attachment strength of specimen to bone after implantation of 2 weeks is shown in Fig. 7. *t*-test demonstrated statistically significant difference between the experimental and control groups. Histological observation of tissues after 2-weeks implantation was shown in Fig. 8. The chitin/chitosan-coated specimens had more bone tissues between the fibers than control specimen. The structure of sparse fibers combining chitin/chitosan coating was effectively induced the bone tissue between the fibers, and increased the attachment strength.

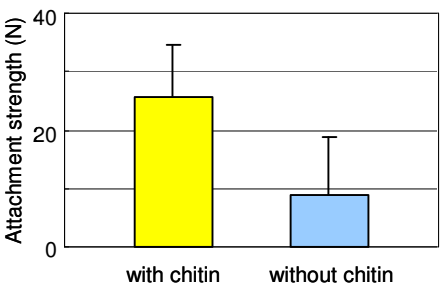

Figure 7. The attachment strength of specimens to bone after 2 weeks implantation. *t*-test revealed that the chitin/chitosan coated fabrics had greater strength than bare fabrics ($p < 0.01$).

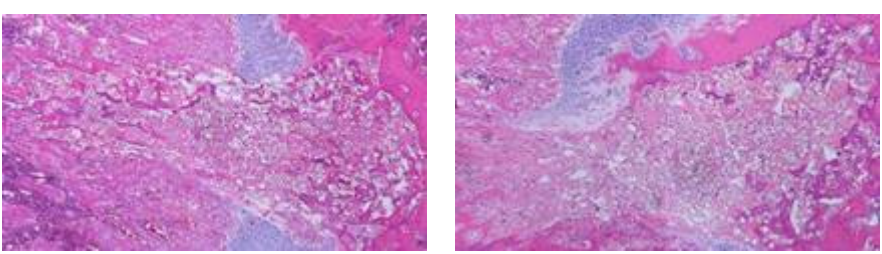

Figure 8. Histological observation of the chitin/chitosan coated (left) and bare (right) fabrics in the drill hole created in rat's femur after 2 weeks implantation. Enhanced bone formation was observed in the chitin/chitosan coated fabrics. HE staining.

4 Reconstruction of Small Diameter Arteries — Supply of Nutrient Required for Regeneration of Bone Tissues

4.1 Materials and methods

Arteries are necessary for the supply of nutrient in the process of bone regeneration. Hence transplantations of autologous bone with vessels are commonly utilized in clinical practices although many drawbacks would accompany them. However artificial vessels for the arteries of small diameter had not yet been successfully developed. The mismatch in compliance as shown in Fig. 9 is believed to be responsible to the early obstruction [4], hence the acellular scaffold of biological origin was utilized in this experiment.

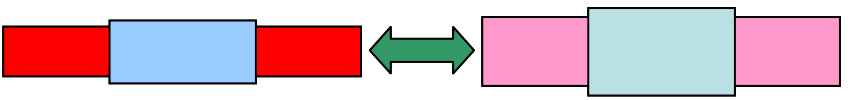

Figure 9. Arteries change their diameter according to the internal blood pressure; their diameter takes smallest value under diastolic blood pressure (left) but the arteries enlarges and takes largest value under systolic blood pressure (right). Compliance mismatch between arteries (red/pink) and grafts (blue/sky blue) causes geometrical irregularities with arterial pulsation and generate disturbance in blood flow, which induces formation of fibrin clot and early obstruction. Hence scaffolds with biomechanical compatibility are necessary to reconstruct arteries.

The acellular scaffolds [5] for arterial reconstruction were utilized in this investigation as the collaborative work with Prof. A. Kishida of Tokyo Medical and Dental University. Briefly, they were prepared from the abdominal aorta of isogenetic rats through the hydrostatic process utilizing high pressure of 10,000 atm. The mechanical properties of these scaffolds were evaluated by the internal pressure test in which pressure-diameter relations were measured. This part of investigation was carried out as the collaborative research work with Assoc. Prof. H. Yamda of Kyusyu Institutes of Technology. The reconstruction of arteries was carried out in the male 9-weeks old SD rats. The defect of 10-mm length was made at the carotid artery, and the graft made from acellular scaffolds of the same size was anatomized. The control grafts, the silicone tubes were also implanted in the same manner. The grafts were retrieved 4 weeks after surgery and macroscopically and histologically evaluated.

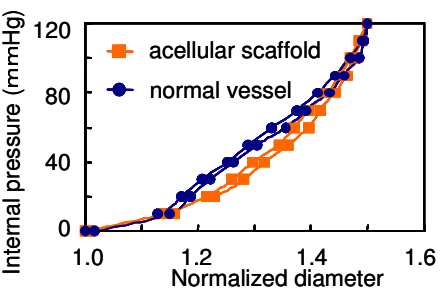

Figure 10. Internal pressure-Normalized diamater relations of acellular scaffolds and normal vessels. The acellular acaffold had similar mechanical properties as the normal vessels.

4.2 Results and discussion

Figure 10 shows the typical pressure-diameter relations of the acellular scaffolds and the normal vessels. The acellular grafts demonstrated the similar compliance as the normal arteries. The patency rates of respective grafts were presented in Table 1. The acellular scaffolds demonstrated superior patency of 83% than silicone tubes. Typical immuno-histological observations were shown in Fig. 11. The smooth muscle cells were infiltrating the whole length of the scaffolds, and the endothelial cells were covering the whole surface of the inner cavity of the scaffolds.

Table 1. Patency of acellular scaffolds and silicone tubes (control). The patent ratio of acellular scaffolds was greater than that of control (χ^2 test, $p < 0.10$).

grafts	patent	occluded	graft patency
Acellular scaffolds	5	1	83%
Silicone tubes	0	5	0%

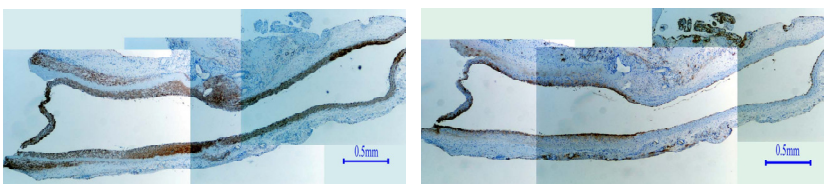

Figure 11. Histological observations of the acellular scaffolds implanted for 4 weeks. Immunological staining; smooth muscle actins (left), and factor VIII (right). Left half part of each specimen was the scaffold. The infiltration of smooth muscle cells and endothelial cells into the acellular scaffolds was observed.

The matching of compliance would decrease the disturbance in the blood flow and reduce the thrombus formation. Thus early obstruction might be suppressed. The structure of the scaffolds was suitable for infiltration of endothelial cells and smooth muscle cells. Furthermore, the suitable compliance would favorable for the immigration and proliferation of these cells since repeated stretching accompanying pulsation in vascular wall enhance the cell activity. These contributed to the good patency in the chronic stage. Thus acellular scaffolds might be useful in the reconstruction of small diameter arteries.

5 Regeneration of Peripheral Nerves — Recovery of Motor Control

5.1 Materials and methods

Regeneration of peripheral nerves is another field in which biomechanical considerations are very important in designing the grafts for regeneration. The

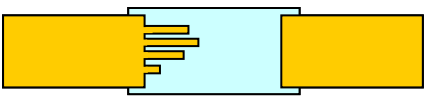

Figure 12. Peripheral nerve regeneration in the nerve conduit. Bioabsorbable tube was inserted as the nerve conduit (central) between proximal end (left) and the distal end (right) of peripheral nerve. The nerve conduits create the space necessary for the nerve regeneration.

Figure 13. A bioabsorbable nerve conduit (bellow tube) was implanted across the 13-mm gap created in the sciatic nerve of rat.

necessity of nerve conduits is illustrated in Fig. 12. A triple copolymer (PLGC) from L-lactide, glycolide, and ε-caprolactone (75:8:1; MW, 300,000) was synthesized in the collaborative work with Kawasumi Lab. Inc. The PLGC membrane of thickness 0.2 mm was used to construct two types of nerve conduits tubes. One was a straight tube with 1.5-mm inner diameter and 15-mm length, and the other was a bellows tube with 1.5-mm inner diameter, 2.4-mm outer diameter and 15-mm length [6].

8-weeks-old male SD rats were used for the animal study. The right sciatic nerve was exposed, and a 10-mm long section was excised from the center of the thigh. Bridge grafting was performed at the nerve gap. Approximately 1 mm of the transected nerve, both at the proximal and distal ends, was inserted into the tube to create a 13-mm gap as shown in Fig. 13. The animals were divided into five groups. They were empty straight tube graft group, fibrin-filled straight tube graft group, empty bellows tube graft group, fibrin-filled bellows tube graft group, and control group. The fibrin gel was derived from isogenic rat plasma. As a control, the isogenic nerve transplantation, in which a 15-mm sciatic nerve was transplanted.

5.2 Results and discussion

All groups showed myelinated nerve regeneration at 12 weeks post-implantation as shown in Fig. 14. In the straight tubes, nerve regeneration occurred at the center of the tube, and regenerated tissues were not in contact with the tube wall. In these groups, the cross-section of regenerated nerves was small and always circular regardless of whether the tube had been deformed over time after implantation. On the other hand, in the bellows tubes, the cross-section of the regenerated nerves was large and had an oval shape as the tube had flattened over time after implantation, and these nerves in bellows tubes were surrounded by layers of tissues that had partially fused with the regenerated tissues underlying the inner surface of the tube. Such a regeneration pattern was noticeable, particularly in fibrin-filled bellows tube graft group.

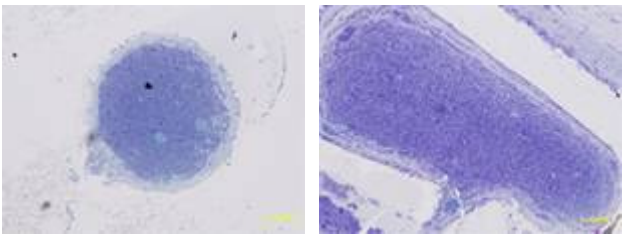

Figure 14. Histological sections at 12 weeks after surgery. Empty straight tube (left) and Fibrin filled bellows tube (right). In bellows tube groups, nerve regeneration occurred along the inner cavity of the tube, and some of the regenerated nerves were attached to the tubes.

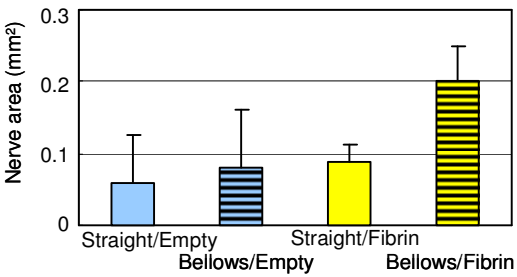

Figure 15. Sectional areas of nerve tissues observed in respective conduits 12 weeks after surgery. Two-way ANOVA showed that the fibrin gel filling had a significant influence on the total area of myelinated axons ($p < 0.05$), while the influence of the tube shape was not significant. The multiple comparison test of Bonferroni/Dunn showed no significant difference only between the case of Bellows/fibrin group and the control group.

The measured area of nerve tissues was presented in Fig. 15. Fibrin-filled bellows tubes had the largest total area of myelinated axons at 12 weeks among all the experimental groups and were comparable to isogenic nerve grafts. Thus we found that the bellows shape and fibrin filling enhances the nerve regenerative performance of nerve guide tubes constructed from bioabsorbable materials.

6 Conclusions

In this study, various attempts were carried out to regenerate tissues for locomotory organs. The devices were designed as with which suitable environment for cells was realized. In such environment prepared, the cells were guided to regenerate tissues through the self-organization process. The animal experiments demonstrated the promising results and the concept of guided tissue regeneration presented here would be useful for regeneration of locomotory organs, although further study was necessary for clinical applications.

Acknowledgments

This work was supported by Grant-in-Aid for Scientific Research on Priority Areas 15086202 from the Ministry of Education, Cultures, Sports, Science and Technology of Japan.

References

1. Berglundh T., Lindhe J., Ericsson I., Marinello CP., Liljenberg B., Thomsen P., 1991. The soft tissue barrier at implants and teeth. Clin. Oral Implants Res. 2, 81-90.
2. Paquay Y.C., de Ruijter J.E., van der Waerden J.P., Jansen J.A., 1997. Wound healing phenomena in titanium fibre mesh: the influence of the length of implantation. Biomaterials 18, 161-166.
3. Yamada T., Koyama Y., Kawai T., Muneta T., Takakuda K., 2007. Bone-demineralized bone-bone grafts for ligament reconstruction. J. Biomech. Sci. Engng. 2, 23-33.
4. Abbott, W. MD Megerman J., Hasson J.E., L'Italien G., Warnock D.F., 1987. Effect of compliance mismatch on vascular graft patency. J. Vasc. Surg. 5, 376-382.
5. Fujisato T., Terada D., Sawada K., Minatoya K., Niwaya K., Kishida A., Nakatani T., Kitamura S., Acellular vascular grafts processed by the supercritical fluid extraction. 2006. ASAIO J. 52, 14A.
6. Nakayama K., Takakuda K., Koyama Y., Itoh S., Wang W., Mukai T., Shirahama N., Enhancement of peripheral nerve regeneration by using bioabsorbable polymer tubes packed with fibrin gel. 2007. Artificial Organs, in press.

IV. COMPUTATIONAL BIOMECHANICS

This page intentionally left blank

MICROSCOPIC ANALYSIS OF BONE

M. TANAKA AND T. MATSUMOTO

Department of Mechanical Science and Bioengineering,
Osaka University Graduate School of Engineering Science,
1-3 Machikaneyama-machi, Toyonaka 560-8531, Japan
E-mail: tanaka@me.es.osaka-u.ac.jp

M. TODOH

Department of Human Mechanical Systems and Design Research,
Hokkaido University Guraduate School of Engineering,
N13 W8, Kita-ku, Sapporo 060-8628, Japan

Bone is a heterogeneous material with a complex hierarchical microstructure, which undergoes continual changes during growth and remodeling. Thus the microcopic analysis of bone structure and material properties will be crucial for the understanding of the overall bone strength and adaptation to its mechanical environment. Using microscopic indentation test, high-resolution X-ray CT, microspectroscopy, and video-microscopic imaging, we demonstrated the close relationship between local material and mechanical properties in trabecular bone and their possible contribution to the overall mechanical properties of cancellous bone, the micro-regional effect of unloading or osteoporosis on trabecular and cortical bone, and the involvement of the regulatory capacity of bone microcirculation in unloading-induced bone atrophy. These observations based on the microscopic point of view could be prerequisites for deeper understanding of bone growth and remodeling.

1 Introduction

Living bone is continually undergoing processes of remodeling. These so-called strain adaptation processes of bone are the mechanism by which bone adapts its structure according to changes in the mechanical environment. The recent advancement of assessment technology for microscopic bone properties [1-3] has significantly promoted a better understanding of the strain adaptation processes of bone. In particular, as indispensable determinants of bone strength, there is growing emphasis on the quality of bone such as the anisotropic microstructure, collagen cross-linking, and mineral crystallinity [4]. The quantification of structural, material, and mechanical characteristics at microscopic levels is also of great use for developing a predictive, dynamical, multiscale mathematical model of bone remodeling, which serve as an in silico platform for testing pharmaceutical and clinical interventions on metabolic bone disease [5]. In this report, the microscopic views of trabecular and cortical bone based on the recent measurement techniques are presented. The following topics are discussed: (1) anisotropic properties of trabecular bone and local remodeling (resorption/formation) of trabecular bone

network; (2) porous microstructure of cortical bone with relating to bone blood perfusion and cortical bone quality; (3) periosteal microvascular flows. Some effects of unloading (sciatic neurectomy) or osteoporosis (ovariectomy) on microscopic properties are also provided.

2 Microscopic View of Trabecular Bone

2.1 Trabecular hardness, mineral content, and their orientation-dependency

Cancellous bone shows three-dimensional anisotropic mechanical properties, which may depend on the trabecular network structure and the material properties of single trabeculae. Therefore, to understand the macroscopic mechanical properties of cancellous bone, it is important to evaluate the microstructural and mechanical properties of single trabeculae and their network geometry. Thus we evaluated the mechanical property and the content of hydroxyapatite of single trabeculae, and these microscopic data were analyzed in relation to the trabecular orientation. Then, the relationship of these microscopic properties to the stiffness of a cancellous bone was evaluated.

From cancellous bone of bovine femur, cubic specimens of 10 mm on each side were cut out for microfocus X-ray CT (NXHCP-C80I, Nittetsu Elex, Japan) and compression test (EZ-test, Shimadzu, Japan), and single trabeculae were removed from the cubic specimen for Vickers hardness test (HMV-1, Shimadzu, Japan) and X-ray diffraction analysis (XRD-6100, Shimadzu, Japan) (Fig. 1). Figure 2 shows the relationship between diffracted X-ray intensity over the range of hydroxyapatite profile and Vickers hardness for single trabeculae. The directions x, y, and z are, respectively, anterior, medial/lateral, and proximal directions and nearly identical to the principal directions of trabecular alignment. The trabecular orientations in the y- and z-directions were equally dominant (data not shown), implying larger mechanical loading in those directions than in the x-direction (*Wolff's law*). Thus, the higher Vickers hardness in the y- and z-directions could be considered the well-adapted property of trabeculae. In addition, three point bending test of single trabeculae showed the highest and smallest stiffness in the z- and x-directions, respectively (data not shown). The hydroxyapatite content will be involved in these anisotropic mechanical properties. These structural as well as

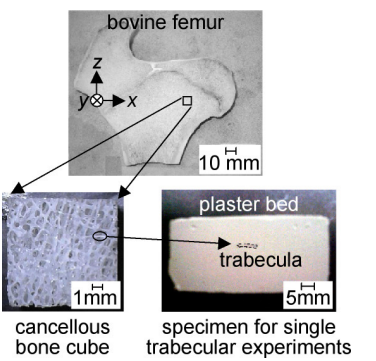

Figure 1. Definition of the directions and the preparation of single trabecular specimen. Reproduced from [6].

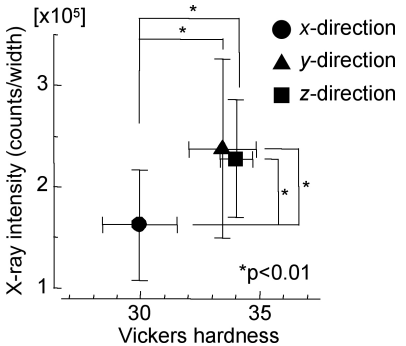

Figure 2. Plot (mean ± SD, n = 5) of diffracted X-ray intensity vs. Vickers hardness. Reproduced from [6].

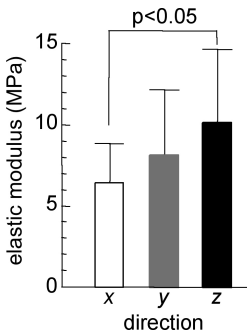

Figure 3. Elastic moduli (mean ± SD) of cubic bone specimens (n = 12). Reproduced from [6].

mechanical anisotropic properties of trabeculae are responsible in part for the macroscopic mechanical properties as shown in the direction-dependent elasticity of the cubic cancellous bone specimen (Fig. 3).

These results indicate that the anisotropic mechanical property of the cancellous bone will be attributed to the structural anisotropy of trabecular network as well as mechanical properties of single trabeculae, which also depend on its orientation and/or local mechanical environment. Other factors such as micro-architecture, tissue properties, and levels of microdamage [7] should be also considered for a better understanding of anisotropic mechanical properties of cancellous bone.

2.2 Local trabecular resorption and formation: Synchrotron radiation μCT study

In the study of structural functions of the trabecular network, it is also important to evaluate the effect of mechanical environmental changes on local trabecular structure. The use of synchrotron radiation (SR) in μCT provides substantial advantages for this purpose because it allows quantitative imaging of bone structure with high spatial resolutions [8]. Using SRμCT system developed at SPring-8 (Japan large-scale synchrotron radiation facility), we carried out in-vivo imaging of structural changes of the tibial metaphyseal trabecular network in mice subjected to unloading in one hindlimb induced by unilateral sciatic neurectomy at 13 weeks of age. The thee-deimensional image was reconstructed with a two-dimensional filtered backward projection algorithm based on radiographic images acquired with 25-keV X-ray over an angular range of 0°-180° with 0.2° steps, providing contiguous images comprised of 1000x1000 cubic voxels of 11.6 μm in size. One CT scan took five minutes.

Trabecular structural changes over time can be detected by overlaying two reconstructed three-dimensional images, provided that the images have equal

orientations. The orientation matching of the images of different time points was achieved with our developed registration algorithm, in which one image A is rotated and translated with respect to the other B to maximize mutual information *MI* [9] given by:

$$MI(\mathrm{A},\mathrm{B}) = \sum_{a,b} P_{\mathrm{AB}}(a,b) \cdot \ln \frac{P_{\mathrm{AB}}(a,b)}{P_{\mathrm{A}}(a) \cdot P_{\mathrm{B}}(b)}$$

$$P_{\mathrm{AB}}(a,b) = \frac{\#\left(\{(x,y,z) \mid LAC_{\mathrm{A}}(x,y,z) = a \text{ and } LAC_{\mathrm{B}}(x,y,z) = b\}\right)}{X \cdot Y \cdot Z}$$

$$P_{\mathrm{A}}(a) = \sum_{b} P_{\mathrm{AB}}(a,b), \quad P_{\mathrm{B}}(a) = \sum_{a} P_{\mathrm{AB}}(a,b),$$

where $LAC_{\mathrm{A}}(x,y,z)$ and $LAC_{\mathrm{B}}(x,y,z)$ are the linear absorption coefficients in images A and B at the space-fixed coordinates x, y, z. Figure 4 presented the superimpose display of transverse sectional images of trabeculae at 7 and 17 days after neurectomy, which were binarized by simple thresholding, setting a threshold value to the hydroxyapatite density of 0.82 g/cm^3.

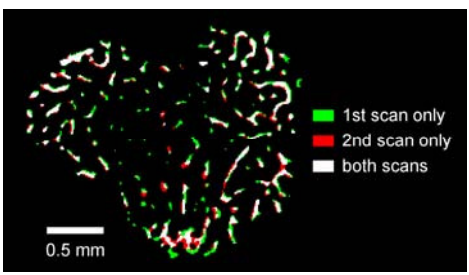

Figure 4. Transverse section of mouse tibiae, segmented and overlaid using the registration algorithm. Green indicates bone that was only present in the 1st scan, and red indicates bone only present in the 2nd scan (10 days later the 1st scan).

This image processing allows to quantitate the volumes of trabecular resorption and formation and their distribution. The comparison of those volumes between intact and neurectomized hindlimbs is shown in Fig. 5, suggesting that mechanical unloading reduces the rate of trabecular bone formation but has an insignificant effect on the rate of bone resorption. In both hindlimbs, the densities of segments and nodes in the trabecular network were reduced whereas the trabeculae were thickened, possibly in compensation for the regression

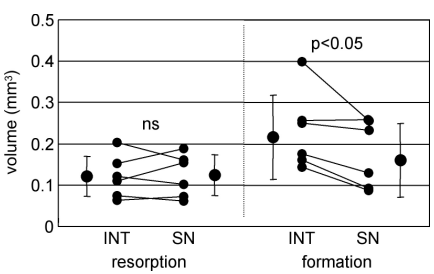

Figure 5. Mechanical-unloading effect on the volumes (mean ± SD) of trabecular resorption and formation in tibiae. SN and INT are sciatic neurectomized and contralateral intact hindlimbs, respectively.

of trabecular network (data not shown). However, the decrease in densities of segments and nodes was enhanced in neurectomized hindlimbs.

Thus, in-vivo SRμCT allows the analysis of the time history of trabecular network structure. What remains to be solved is how to reduce the high X-ray dosage although there were no apparent damages on mice. New developments in detector technology allow to expect a gain in sensitivity, the reduction of scan time, and thus a lowered dose.

3 Microscopic View of Cortical Bone

3.1 Microstructure of porous canal network in cortical bone

In cortical bone, microvessels are running through an interconnected network of porous canals, facilitating bone perfusion indispensable for bone growth, remodeling, and repair [10]. Therefore, we can speculate about the state of cortical bone perfusion on the basis of canal network structure. Although the canal network structure has been less well understood because of the methodological difficulties, the availability of SRμCT has opened up new possibilities in the three-dimensional analysis of cortical bone microstructure. Its availability of monochromatic X-rays with extremely high light intensity are beneficial in obtaining metric properties of cortical canals such as diameters and volumes as well as topological properties of the canal network structure.

Mechanical unloading induces bone atrophy; however, its effect on the canal network structure in cortical bone has been less understood. In Fig. 6, the volume-

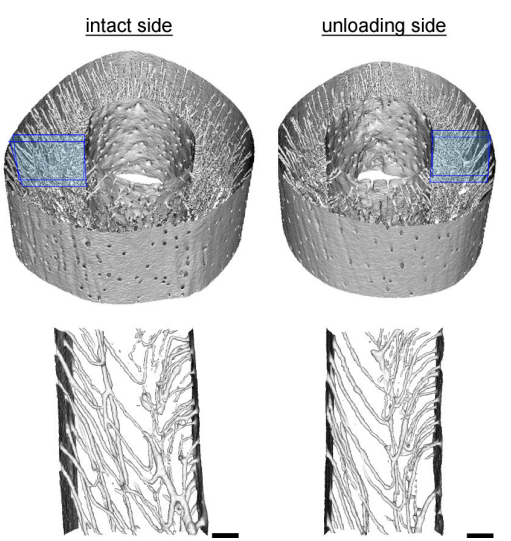

Figure 6. Top, a pair of rat tibial diaphyses, generated by 3D isosurface rendering of reconstructed 2D images. Bone mineral density on the isosurface is 0.82 g/cm^3. Bottom, enlarged views of the boxed regions in top. Bar: 150 μm. Reproduced from [11].

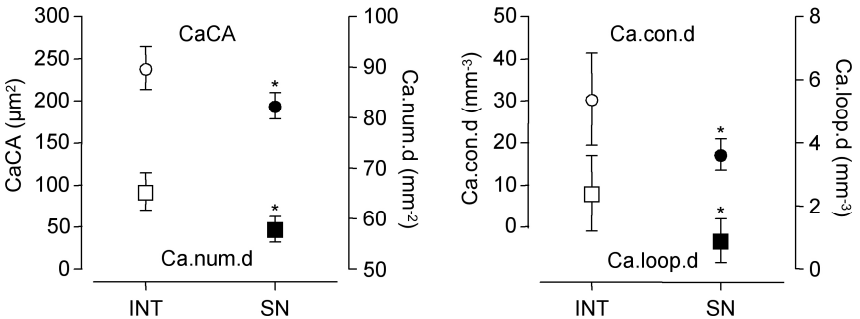

Figure 7. Plots (mean ± SD, n = 8) of canal cross-sectional area (CaCA, μm^2), the density of canals running longitudinally (Ca.num.d, mm^{-2}), the density of canal connections (Ca.con.d, mm^{-3}), and the density of canal loops (Ca.loop.d, mm^{-3}). *$p < 0.05$ vs. intact (Wilcoxon matched-pairs signed-rank test). INT, intact, SN, sciatic neurectomy. Reproduced from [11].

rendered three-dimensional display of a pair of tibial diaphyses and close-up views of the boxed regions are shown. System parameters for SRμCT were set to the same values as described in the preceding section except for the projection angular step (0.5°), the scan time (90 min), and the voxel size (5.83 μm). These tibiae were harvested from a 14-week rat treated with unilateral sciatic neurectomy of the left hindlimbs at 6 weeks of age. Neurectomy-induced unloading lead to canal network regression as well as bone atrophy. The indexes characterizing the canal network structure are shown in Fig. 7, indicating that bone atrophy is accompanied by the changes of cortical canals, i.e., the decrease in canal cross-section and the regression of the canal network characterized by the tree-like connection. Considering that canals possibly contain a single vessel of capillary structure, this canal network regression could be translated as the regression of the vascular network, leading to lower perfusion, higher flow heterogeneity, and smaller surface area for oxygen and nutrients requisite for cortical bone cells.

3.2 Transport in cortical bone through porous network: A model study

Bone structural adaptation to its mechanical environment requires the activation of bone forming cells, which will be regulated by osteocytes according to the magnitude, pattern, and frequency of mechanical stimuli. Osteocytes are embedded and networked in bone, and they are nourished through bone canaliculi connected to vascular canals constituted of Haversian and Volkman's canals, in which blood vessels run through. Osteogenic and osteoclastogenic factors derived from blood are also delivered to osteocytes through the canaliculi. Therefore, the transport analysis of physiological substances from circulating blood to osteocytes based on canalicular and vascular canal networks is important for a better understanding of the physiological significance of the porous network structure in cortical bone. Thus,

we modeled transport phenomena of physiological substances in cortical bone by considering the advection-diffusion problem in vascular canals and canaliculi.

The transport by the vascular canal network was formulated using the one-dimensional advection-diffusion equation. On the other hand, the transport by the canalicular network was assumed to be diffiusive and formulated using the three-dimensional diffusion equation, in which the diffusivity was assumed to be one hundredth of the difusivity of blood. These equations were coupled with each other by taking the substance exchange between the vascular canals and canaliculi into account. Computational analysis using the finite difference method showed that in every region the concentrations of substances (e.g., oxygen and glucose) were far from critical situation even with hypoperfused or high metabolic conditions (data not shown), suggesting that the substance transport in cortical bone was limited by the vascular and/or canalicular canal network structures.

3.3 Local material and mechanical properties in cortical bone

One of the recent focuses in bone research is the relationship between the mechanical and material properties at microscopic level. Along with the bone density, the latter, what is termed bone quality, may be essential determinants of bone strength. Thus, using the recently established technique [12], we evaluated the relationship between the mechanical and material characteristics of cortical bone from the microscopic point of view.

Tibial cortical bone specimens harvested from the ovariectomized osteoporotic (OVX) and the sham-operated (SHAM) female rats of 14-to-28-week old, which were both operated at 12 weeks of age. Combining the nanoindentation technique (DUH-W201S, Shimadzu, Japan) with the Fourier transform infrared microspectroscopy (FTIR-MS; IRPrestige-21, Shimadzu, Japan), measurements were carried out for 50x50-μm^2 regions at the anterior, lateral, medial and posterior portions of diaphyseal shaft. The indentation elastic modulus (E_{ind}) and the dynamic hardness (DH) were evaluated by Oliver-Pharr method [13]. The mineral to matrix ratio (Min/M) as the bone quantity, and the hydroxyapatite crystallinity (HA_{cry}) and the collagen cross-link (Col_{crl}) as the bone quality were evaluated by FTIR-MS. The test regions for the FTIR-MS were precisely the same regions for the nanoindentation test.

No correlation was found between Min/M and E_{ind} nor DH for both SHAM and OVX (data not shown). On the other hand, HA_{cry} was correlated significantly with both E_{ind} and DH in SHAM; E_{ind} and DH increased with HA_{cry}, but not in OVX (Fig. 8). Significant positive correlation was found between Col_{crl} and E_{ind} in both SHAM and OVX, whereas no correlation was found between Col_{crl} and DH in both groups (Fig. 9). Furthermore, the high positive correlation was found between HA_{cry} and Col_{crl} in SHAM. These results suggests that Col_{crl} contributes to bone elasticity, irrespective of the ovariectomy-induced disorders. On the other hand, HA_{cry} is

crucial for the bone hardness but not in ovariectomy-induced osteoporosis. Regarding Min/M, it is unlikely to influence the local bone elasticity and hardness.

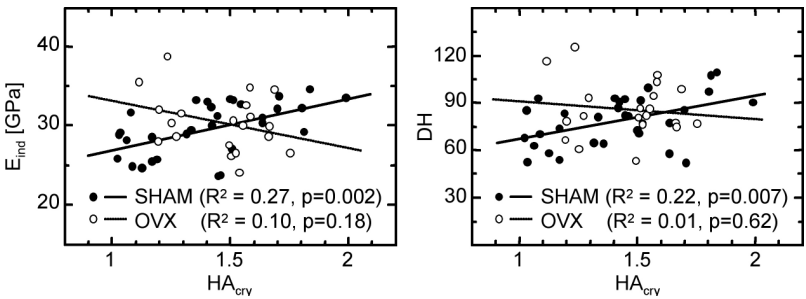

Figure 8. Plots of indentation elastic modulus (E_{ind}) and dynamic hardness (DH) vs. hydroxyapatite crystallinity (HA_{cry}).

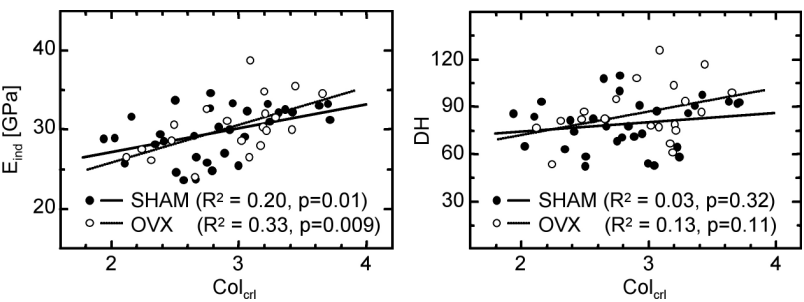

Figure 9. Plots of indentation elastic modulus (E_{ind}) and dynamic hardness (DH) vs. collagen cross-link (Col_{crl}).

4 Periosteal Microcirculation: Study of the Effect of Mechanical Unloading

Blood flow plays an important role in bone growth, remodeling, and repair by supplying with oxygen, nutrients, and humoral regulators. Currently available techniques to measure blood flow in bone are the microsphere technique [14] and laser Doppler flowmetry [15]. These techniques, although a better assessment of tissue blood flow than a single point, do not allow the flow measurements at a single point. In contrast, a video-microscopic technique is appropriate to measure the flow dynamics in a single vessel by visualizing erythrocytes flowing through the vessel. Thus, using a pencil lens-probe CCD intravital video-microscopic system (Scalar, Japan), we acquired real-time images of periosteal microvessels and assessed the effect of mechanical unloading on periosteal microvascular functions by monitoring dynamic responses to vasoactive agents.

Figure 10 shows the image of periosteal venules of a rat tibia and the time histories of light intensity at two slits. The blood (red cell) velocity was determined by finding τ, which maximize the correlation between light intensity waveforms $f_A(t+\tau)$ and $f_B(t)$ at upstream and downstream slits, respectively [16]. Prior to the analysis of video sequences on a pixel-by-pixel basis, each image was corrected for motion artifacts due to the animal body motion.

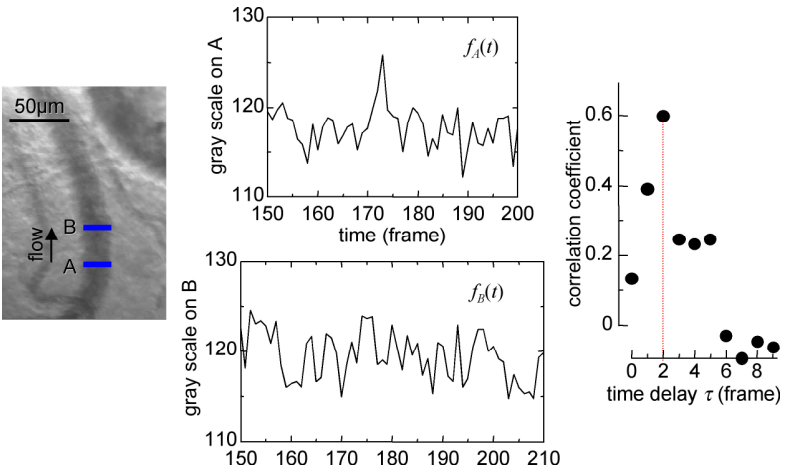

Figure 10. Periosteal microvessel image (left), time histories of light intensity on the slits A and B (middle), and the plot of the correlation coefficient between $f_A(t+\tau)$ and $f_B(t)$ vs. τ (right).

The effect of unloading on the endothelium-dependent vascular function was evaluated by the flow response to the superperfusion of acetylcholine (ACh) and sodium nitroprusside (SNP) on the neurectomized and the contralateral intact hindlimbs. Both Ach and SNP increased red cell velocity to a similar extent on the intact hindlimb (44.4 vs. 52.6%), but the ACh-induced increase was lower under neurectomy (14.5 vs. 42.7%), implying the impaired endothelium function due to unloading.

5 Conclusions

A mechanistic understanding of bone growth and remodeling processes at a microscopic level was limited to postulations with little experimental insight. With current technology, however, it has become possible to acquire new information on anatomical, material, and mechanical microscopic properties. The microscopic views of trabecular and cortical bone presented here demonstrated (1) the close relationship between local material and mechanical properties in trabecular bone and

their possible contribution to the overall mechanical properties of cancellous bone, (2) the micro-regional effect of unloading or osteoporosis on trabecular and cortical bone, and (3) the involvement of the regulatory capacity of bone microcirculation in unloading-induced bone atrophy. These observations from the microscopic point of view could be prerequisites for deeper understanding of bone growth and remodeling

Acknowledgments

The synchrotron radiation experiments were performed at SPring-8 with the approval of the Japan Synchrotron Radiation Institute. This work was supported by Grant-in-Aids for Scientific Research on Priority Areas 15086210 and for Exploratory Research 17650138 from the Ministry of Education, Cultures, Sports, Science and Technology of Japan, and Grant-in-Aid for Scientific Research (B) 17300152 from the Japan Society for the Promotion of Science.

References

1. Genant, H.K., Jiang, Y., 2006. Advanced imaging assessment of bone quality. Ann. N. Y. Acad. Sci. 1068, 410-428.
2. Boskey, A.L., Assessment of bone mineral and matrix using backscatter electron imaging and FTIR imaging. Curr. Osteoporos. Rep. 4, 71-75.
3. Siffert, R.S., Kaufman, J.J., 2007. Ultrasonic bone assessment: “the time has come”. Bone 40, 5-8.
4. Hernandez, C.J., Keaveny, T.M., 2006. A biomechanical perspective on bone quality. Bone 30, 1173-1181.
5. Defranoux, N.A., Stokes, C.L., Young, D.L., Kahn, A.J., 2005. In silico modeling and simulation of bone biology: a proposal. J. Bone Miner. Res. 20, 1079-1084.
6. Todoh, M., Ihara, M., Matsumoto, T., Tanaka, M., 2004. Relationship between mechanical property of cancellous bone and hardness of trabeculae. JSME Int. J. 47C, 1075-1078.
7. McDonnell, P., McHugh, P.E., O’Mahoney, D., 2007. Vertebral osteoporosis and trabecular bone quality. Ann. Biomed. Eng. 35, 170-189.
8. Bonse, U., Busch, F., 1996. X-ray computed microtomography (μCT) using synchrotron radiation (SR). Prog. Biophys. Mol. Biol. 65, 133-169.
9. Maes, F., Collignon, A., Vandermeulen, D., Marchal, G., Suetens, P., 1997. Multimodality image registration by maximization of mutual information. IEEE Trans. Med. Imaging 16, 187-198.
10. Brandi, M.L., Collin-Osdoby, P., 2006. Vascular biology and the skeleton. J. Bone Miner. Res. 21, 183-192.

11. Matsumoto, T., Yoshino, M., Asano, T., Uesugi, K., Todoh, M., Tanaka, M., 2006. Monochromatic synchrotron radiation μCT reveals disuse-mediated canal network rarefaction in cortical bone of growing rat tibiae. J, Appl. Physiol. 100, 274-280.
12. Busa, B., Miller, L.M., Rubin, C.T., Qin, Y.X., Judex, S., 2005. Rapid establishment of chemical and mechanical properties during lamellar bone formation. Calcif. Tissue Int. 77, 386-394.
13. Oliver, W.C., Pharr, G.M., 1992. An improved technique for determining hardness and elastic modulus using load and displacement sensing indentation experiments. J. Mater. Res. 7, 1564-1583.
14. Anetzberger, H., Thein, E., Becker, M., Walli, A.K., Messmer, K., 2003. Validity of fluorescent microspheres method for bone blood flow measurement during intentional arterial hypotension. J. Appl. Physiol. 95, 1153-1158.
15. Shymkiw, R.C., Zernicke, R.F., Forrester, K.R., Bray, R.C., 2001. Evaluation of laser-Doppler perfusion imaging for measurement of blood flow in cortical bone. J. Appl. Physiol. 90, 1314-1318.
16. Wayland, H., Johnson, P.C., 1967. Erythrocyte velocity measurement in microvessels by a two-slit photometric method. J. Appl. Physiol. 22, 333-337.

COMPUTATIONAL BIOMECHANICS OF BLOOD FLOW IN CARDIOVASCULAR DISEASES

T. YAMAGUCHI, T. ISHIKAWA, K. TSUBOTA,
Y. IMAI, D. MORI AND N. MATSUKI

Department of Bioengineering and Robotics, Tohoku University,
6-6-01 Aoba-yama, Sendai 980-8579, Japan
E-mail: takami@pfsl.mech.tohoku.ac.jp

Variations in both spatial and temporal scales must be considered to fully understand cardiovascular diseases. Given these considerations, we investigated the cardiovascular system from the micro- to macroscale using computational biomechanics. This paper presents our findings on mass transport in cerebral aneurysms, platelet aggregation in blood flow, and a particle method for computing microcirculation. Ultimately, these models will help to clarify the biological phenomena surrounding disease processes and will provide a framework for integrating future developments in understanding macro- and microscale biomechanics.

1 Introduction

In the past decade, computational biomechanics have been intensely used to further our understanding of the human cardiovascular system. Most modern analyses of the cardiovascular system are strongly motivated by a desire to understand the associated pathological processes. Among the pathologies studied, atherosclerosis remains the most important disease in terms of biomechanical analysis. Atherosclerosis is typically a chronic disease that develops over decades, generally becoming problematic in the latter stages of life. Although numerous computational biomechanics studies have been performed, the mechanisms of initiation and development remain unclear. These mechanisms remain convoluted because many of the studies conducted to date have not considered biological complexities, such as the transport of proteins in blood flow, the response of cells to hemodynamic factors, and the function of receptors on a cell. The spatial domains of these biological complexities are broad, ranging from micro- to macroscale, under time constants that range from nanoseconds to decades. Understanding and incorporating these variations in spatial and temporal scales is essential to fully understand and model cardiovascular diseases.

To begin to incorporate these parameters, we investigated the cardiovascular system using computational biomechanics. This paper presents research on three separate areas of investigation. Section 2 discusses mass transport in cerebral aneurysms. Mass transport of biochemical species, such as low density lipoprotein (LDL), oxygen, and adenosine tri-phosphate (ATP), has been postulated to be a link in the initiation and development of cardiovascular diseases [1,2]. Specifically, we investigated the mass transport of biochemical species to the vessel walls in arterial

bend aneurysms. Section 3 presents work on platelet aggregation in blood flow, since thrombus formation is a critical phenomenon both physiologically and pathologically. Although thrombus formation is regulated by a series of physiological and biochemical processes, various mechanical factors are involved. A novel numerical method is presented that incorporates the mechanical interactions of biological receptors on platelets. Finally, Section 4 presents a particle method for computing microcirculation. In microcirculation, the mechanical behavior of blood cells has direct effects on blood flow properties. In using a particle method, the developed simulation analyzes blood flow by considering deformable red blood cells (RBCs), which constitute up to 45% of whole blood. This method can be applied to investigate microcirculation disorders induced by blood diseases.

2 Mass Transport in Cerebral Aneurysms

2.1 Methods

We assumed blood was an incompressible Newtonian fluid. In human cerebral arteries, the Reynolds number is approximately 200 and the Womersley number is 2.0. In such cases, the effects of pulsatile flow are relatively small, allowing calculations to be made under steady-state conditions. The governing constraints are the Navier-Stokes equation and a divergence free condition:

$$\mathbf{u} \cdot \nabla \mathbf{u} = -\nabla p + \frac{1}{\mathrm{Re}} \nabla^2 \mathbf{u} \tag{1}$$

$$\nabla \cdot \mathbf{u} = 0 . \tag{2}$$

where $\mathbf{u}$ refers to the velocity vector, p is pressure, and Re is the Reynolds number. Mass transport of biochemical species are governed by the following advection-diffusion equation:

$$\mathbf{u} \cdot \nabla c = \frac{1}{\mathrm{Pe}} \nabla^2 c , \tag{3}$$

where c is an arbitrary species concentration, and Pe is the Peclet number.

Five models were examined as illustrated in Fig. 1. All models employed the same aneurysm shape; aneurysm height was 4.5 mm, the fundus diameter was 4.8 mm, and the neck diameter was 2.8 mm. The diameter of the parent artery was 3.5 mm, and the radius of curvature was 6.0 mm in models II and IV, and 12.0 mm in models I and V. Model III employed a straight vessel using the same parent artery diameter.

Boundary conditions were specified to provide a no-slip condition at the walls, a steady Poiseuille velocity profile with Re = 200 at the inlet, and free outflow at the outlet for Eqs. (1) and (2). For mass transport governed by Eq. (3), a constant

concentration was specified at the inlet boundary, and free outflow was applied to the outlet boundary. The wall boundary condition was:

$$\frac{\partial c}{\partial \mathbf{n}} = Kc\,, \tag{4}$$

where **n** is the normal vector to the wall surface, and K is a constant. The Peclet number and K were set to 3.0×10^5 and 5.0×10^{-1}, respectively, based on published values [3,4].

The governing equations were solved as coupled equations using a finite volume method, where pressure-velocity coupling was handled by the SIMPLE method using a commercial finite-volume computational fluid dynamics (CFD) package (FLUENT, Fluent Inc., Lebanon, NH, USA).

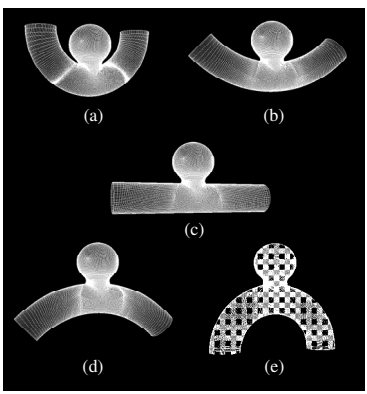

Figure 1. Surface meshes for the various computational models: (a) model I; (b) model II; (c) model III; (d) model IV; (e) model V.

2.2 Results and discussion

Figure 2 illustrates concentration profiles of an arbitrary species at the inner walls of aneurysms for the various geometries modeled, with flow direction from left to right. High species concentrations appeared at the distal regions of aneurysm necks, where fluid particles either entered the aneurysm or were diverted downstream into the artery. Concentrations at the aneurysm walls were relatively small compared to their parent arterial walls. Although these models had the same aneurysm geometry, concentrations varied. Figure 3(a) shows the averaged concentrations at the aneurysm walls, with values normalized to model III. Model II resulted in the lowest concentration, while model V demonstrated the highest concentration, corroborating clinical observations [5]. Figure 3(b) shows mass influx through the aneurysm necks, again normalized against model III. A strong correlation between the

concentration at the aneurysm walls and the influx into aneurysms was observed. Differences in the influx due to parent arterial geometry resulted in a range of concentrations, even for models having the same aneurysm shape. Most clinical studies investigating aneurysm development have focused on size and shape [6,7]. Our results suggest that the parent arterial geometry also plays a critical role in the distribution of thrombus-forming species within aneurysms.

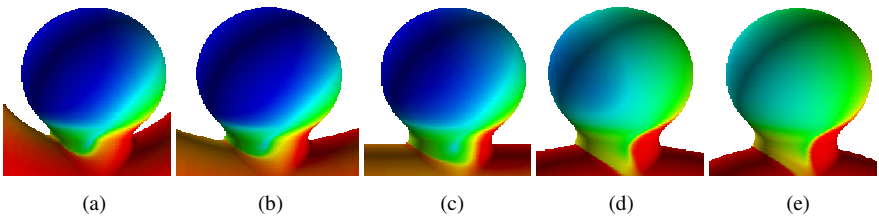

Figure 2. Concentration at aneurysm walls: (a) model I; (b) model II; (c) model III; (d) model IV; (e) model V.

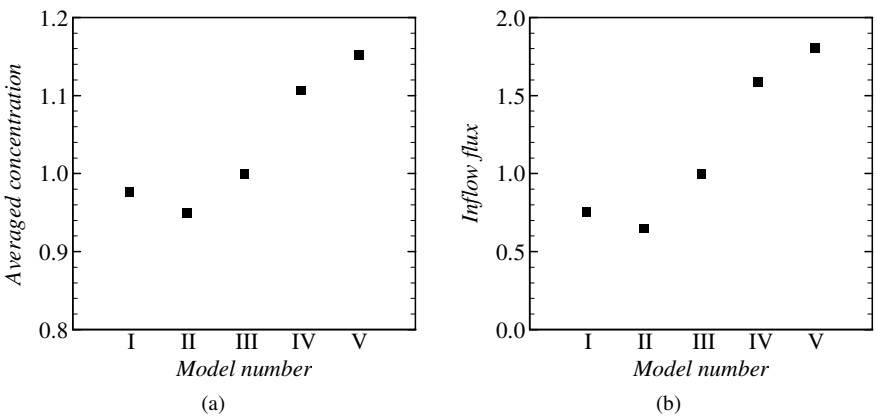

Figure 3. Relationship between concentration at aneurysm walls and aneurysm influx: (a) averaged concentration at aneurysm walls; (b) influx through aneurysm necks. In both cases, values are normalized based on model III.

3 Platelet Aggregation in Blood Flow

3.1 Methods

The general framework used follows Stokesian dynamics, based on the approximation of velocity additivity, which was used by Satoh et al. [8,9] to

examine ferromagnetic colloidal dispersions. The method has been modified to simulate platelet adhesion and aggregation processes by modeling binding forces mediated by plasma proteins in place of magnetic force.

The developed model considers the motion of platelets near the blood vessel wall boundary, where a simple shear background flow is imposed. Platelets were idealized as solid spheres with a diameter of 2 μm. Plasma was assumed to be an incompressible Newtonian fluid, with the flow field around platelets being governed by the Stokes equation.

Based on the additivity of velocities caused by the force exerted on a particle, Stokesian dynamics yields a particle velocity as follows:

$$\boldsymbol{v}_\alpha = \mathbf{U}(\mathbf{r}_\alpha) + \frac{1}{\eta}\left\{\frac{1}{6\pi a}\boldsymbol{F}_\alpha + \sum_{\beta=1(\neq\alpha)}^{N}\left(\boldsymbol{a}_{\alpha\alpha} - \frac{1}{6\pi a}\boldsymbol{I}\right)\cdot\boldsymbol{F}_\alpha + \sum_{\beta=1(\neq\alpha)}^{N}\boldsymbol{a}_{\alpha\beta}\cdot\boldsymbol{F}_\beta\right\} + \sum_{\beta=1(\neq\alpha)}^{N}\tilde{\boldsymbol{g}}_\alpha : \boldsymbol{E}, \quad (5)$$

where $\mathbf{U}(\mathbf{r}_\alpha)$ is the velocity of the background flow field at the position of particle α, $\boldsymbol{F}_i$ ($i = \alpha, \beta$) is the force acting on particle i, a is the particle radius, $\boldsymbol{E}$ is the background rate-of-strain tensor, $\boldsymbol{I}$ is the unit tensor, $\boldsymbol{a}_{ij}$ and $\tilde{\boldsymbol{g}}_i$ are the mobility tensors, and N is the number of particles in the system [8,9]. Values for the mobility tensors can be found in standard texts (see [10]).

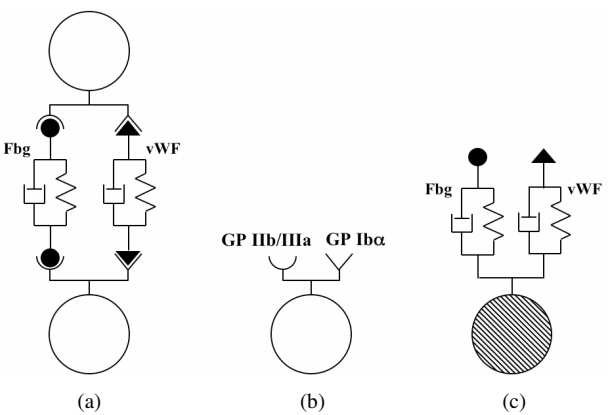

Figure 4. Schematic representation of platelet–platelet aggregation and platelet–surface adhesion via plasma proteins and GPs. (a) The force mediated by two plasma protein couplings, i.e., vWF and Fbg, were modeled using two distinct Voigt models, each composed of a parallel spring and dashpot. (b) Model for GP receptors on a particle. (c) As with platelet-platelet interaction, the binding force between platelets and blood vessel walls was modeled with vWF and Fbg.

In considering the binding force induced between particles by plasma proteins, the external force $\boldsymbol{F}_i$ exerted on the particles, we assumed that the force is induced exclusively by two plasma proteins, fibrinogen (Fbg) and von Willebrand factor (vWF), the main participants in platelet adhesion and aggregation. To express the distinct properties of these two proteins [11,12], we prepared two Voigt models, each possessing different parameters (Fig. 4). Glycoproteins (GP) IIb/IIIa and Ibα, which are the main receptors for Fbg and vWF, respectively, were modeled on the platelet particle to reproduce the selective association of plasma proteins with their respective receptors.

To reproduce their function as long-chain molecules, a binding force between two particles was assumed to occur when the two particles are within a specific separation distance of 0.5 μm. In addition, the following distinctive rules were set for Fbg-GP IIb/IIIa and vWF-GP Ibα associations. To reproduce the efficiency of the Fbg-GP IIb/IIIa association at low shear rates, we assumed that the Fbg–GP IIb/IIIa association forms only when the relative velocity between two particles becomes less than a specific value of 5.5×10^{-2} m/s [11]. In contrast, to reproduce the reversibility of vWF-GP Ibα associations, we assumed that the vWF-GP Ibα association exists only for a specific time of 0.5 s [11].

3.2 Results and discussion

The present method modeled the process of platelet thrombus development on injured vessel walls under a simple shear flow, including RBCs, as shown in Fig. 5. Platelets flowing near the vessel wall initially adhere to the injured wall by interacting with wall-bound vWF and Fbg. Subsequently, adhered platelets recruit additional flowing platelets to begin aggregation (Fig. 5a). This aggregation process leads to an increase in thrombus size (Fig. 5b). However, once the thrombus height reaches a level where RBCs flow, thrombus development is constrained in height by direct interaction with RBCs (Fig. 5c).

Additional simulations were also conducted, including a simulation in which either vWF or Fbg model was inhibited, and a simulation in which RBCs were removed. The former simulation indicated that significant development of

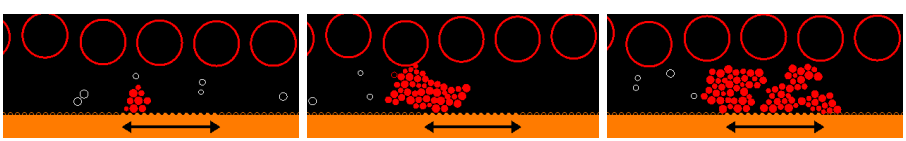

(a) (b) (c)

Figure 5. Simulated thrombus formation on an injured vessel wall under simple shear flow (1000 s^{-1}). Arrows indicate the region of the injured vessel wall where vWF and Fbg models are set. (a) t = 2 s. (b) t = 6 s. (c) t = 10 s.

thrombus height required the presence of both vWF and Fbg. The latter demonstrated that thrombus development was not constrained in the absence of RBCs, indicating that RBC shear restricts thrombus development. These results suggest that plasma proteins vWF and Fbg, as well as RBCs, play important roles in the process of primary thrombus formation.

4 Particle Method for Computing Microcirculation

4.1 Methods

As a two-dimensional blood flow simulation using a particle method [13-16], the blood region was discretized using particles assumed to have the characteristics of RBCs and plasma, as shown in Fig. 6; RBCs were assumed to consist of a surface membrane and inner fluid particles. A spring network model was applied to RBC membrane particles to incorporate the elastic behavior of deformable RBCs, with membrane particles connected to neighboring membrane particles by springs for stretch/compression (L) and bending (B) [17]. Based on the elastic energy E stored in the stretch/compression and bending springs, the spring force $\mathbf{F}_i$ on the membrane particle was calculated from the position vector $\mathbf{r}_i$ as $\mathbf{F}_i = -\partial E / \partial \mathbf{r}_i$.

Assuming incompressible viscous flow, the motion of all particles was determined under specified boundary conditions using the moving particle semi-implicit (MPS) method [18]. In the MPS method, particle motion is modeled based on the continuity equation and the Navier-Stokes (NS) equations using a semi-implicit time-marching algorithm. The gradient vectors and Laplacian of the scalar quantity of particles, which appear in the NS equations, are expressed by considering the interaction with their neighboring particles. With respect to RBC membrane particles, the elastic spring force was substituted in the NS equations as the external force term and solved explicitly, enabling a coupled analysis of viscous fluid (plasma and inner fluid of RBCs) and an elastic membrane (RBC membrane) to be performed [16].

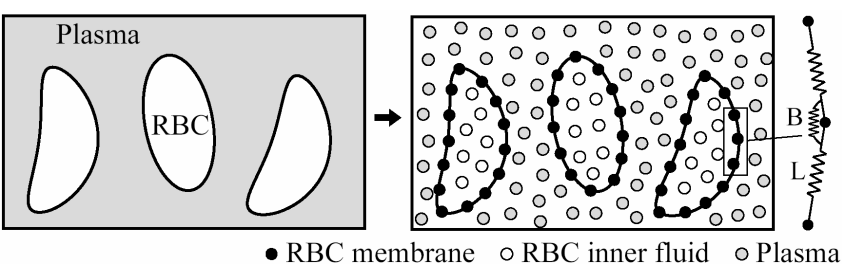

Figure 6. Two-dimensional simulation model of blood using discrete particles.

A two-dimensional model was constructed to simulate blood flow between parallel plates [16], as shown in Fig. 7. The model consisted of RBCs, plasma, and rigid plates. The length of the flow channel (L) and the distance between plates (D) were $L = 90.0$ μm and $D = 9.0$ μm, respectively. Biconcave RBCs were arranged at equal distances with their long axes set perpendicular to the flow direction; this shape was obtained as the final state of a shape change simulation based on the spring network model [16,17]. As boundary conditions, a constant and uniform velocity $u_0 = 1.1 \times 10^{-2}$ m/s was applied to the inlet, where the Reynolds number with respect to the plate separation distance was 0.10. A zero-pressure condition was applied to the outlet. Non-slip conditions were assumed between the plasma and RBCs, and between the plasma and the plates. The viscosity and density were set to be the same as those of water. The mean distance between two neighboring discrete particles was set to 0.25 μm. Spring constants of the RBC membrane were set as 5.0×10^{-8} N · m for stretch/compression and 5.0×10^{-10} N · m for bending [16].

4.2 Results and discussion

The dynamic behavior of elastic RBCs in blood flowing between parallel plates was investigated by computer simulation [16]. Figure 7 shows the characteristic movement and deformation of RBCs in blood flow for a hematocrit value (Hct) of 0.49, with simulation time normalized to $T_0 = L/u_0$. RBCs moved downstream in the flowing plasma at a constant velocity. At flow onset, RBCs maintained their concave shape near the inlet but deformed into a convex shape as they progressed downstream, similar to the parachute shape observed in experiments. From $t/T_0 =$ 0.3 to 0.6, RBCs retained their deformed parachute shape, as blood flow reached a steady state.

A parametric study on Hct demonstrated that at higher Hct, RBCs were less deformed [16]. The degree of RBC deformation was quantified by a deformation index $\varepsilon = |(h - h_0)/h_0|$, where h and h_0 are the projection length of an RBC against the cross section of the flow channel and its initial value. Figure 8 shows the mean value of the deformation index (ε_M) from $t/T_0 =$ 1-3 as a function of Hct. ε_M remained constant when Hct was less than 0.20, and monotonically decreased with increasing Hct. For Hct of 0.49, the deformation index ε_M was 37% less than for an Hct of 0.1. This result agrees with the suppressing effects of Hct on RBC deformation observed in *in vitro* experiments [19].

Our simulation method has been extended to analysis of platelet aggregation [20] and coupled problem between RBCs and platelets [21]. In these studies, we analyzed motion of a single and multiple blood cells in blood flow, and clarified that the mechanical behaviors of blood cells play a pivotal role in both normal function of microcirculation and cardiovascular disease such as thrombogenesis. This means that the particle method is potentially an important and useful approach for investigating the mechanical behavior of blood cells in microscale blood flow.

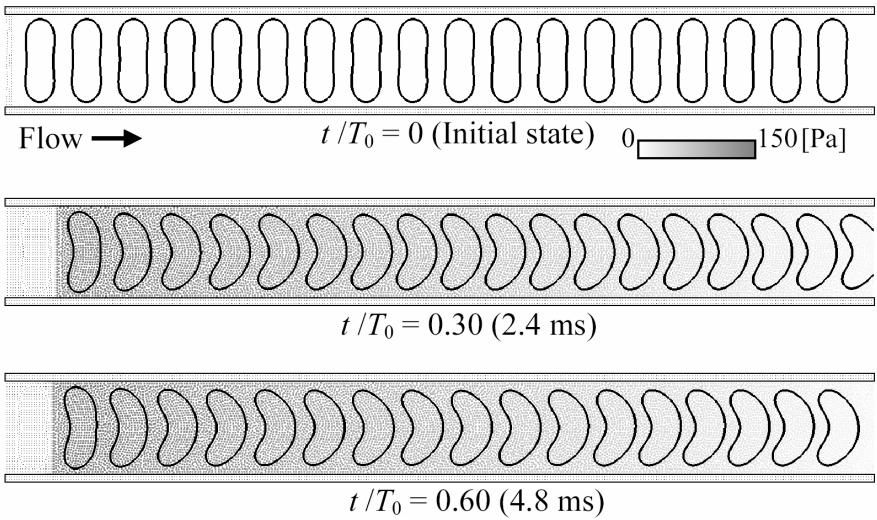

Figure 7. Blood flow simulation with multiple RBCs (Hct = 0.49).

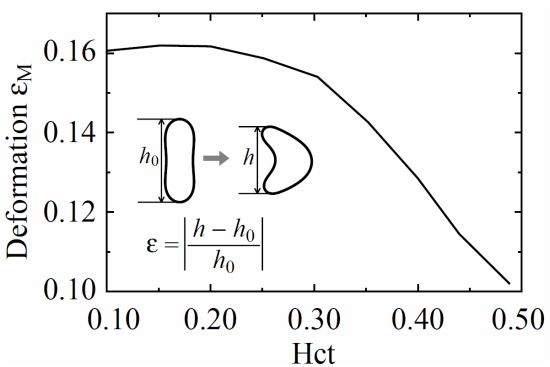

Figure 8. Deformation of RBCs as a function of hematocrit level (Hct).

5 Conclusions

This paper introduces recent cardiovascular research from micro- to macroscales using computational biomechanics. The goals of these investigations were to incorporate biological complexities into biomechanical simulations. The findings contained herein indicate that incorporating these complexities, such as thrombus geometry, protein binding, and the mechanical properties of participating cells, is crucial for developing an accurate and biologically representative model of

thrombus development. In considering clinical applications, however, one needs to consider more about biological complexities, especially with respect to disease processes. A disease is not just a failure of machine. It is an outcome of complex interactions among multi-layered systems and subsystems. We expect that biological phenomena, including disease processes, will be clarified in the future by integrating new understandings of macroscale and microscale hemodynamics.

Acknowledgments

This work was supported by Grant-in-Aid for Scientific Research on Priority Areas 15086204 from the Ministry of Education, Cultures, Sports, Science and Technology of Japan. This research was also supported by the "Revolutionary Simulation Software" (RSS21) project, funded by the next-generation IT program of the Ministry of Education, Culture, Sports, Science, and Technology (MEXT), and Grant-in-Aid for Scientific Research (S) by the Japan Society for the Promotion of Science No. 19100008.

References

1. Caro, C.G., Fitz-Gerald, J.M., Schroter, R.C., 1971. Atheroma and arterial wall shear observation, correlation and proposal of a shear dependent mass transfer mechanism for atherogenesis. Proc. R. Soc. Lond. B 177, 109-133.
2. Ethier, C.R., 2002. Computational modeling of mass transfer and links to atherosclerosis. Ann. Biomed. Eng. 30, 461-471.
3. David, T., 2003. Wall shear stress modulation of ATP/ADP concentration at the endothelium. Ann. Biomed. Eng. 31, 1231-1237.
4. Comerford, A., David, T., Plank, M., 2006. Effects of arterial bifurcation geometry on nucleotide concentration at the endothelium. Ann. Biomed. Eng. 34, 605-617.
5. Weir, B., 2002. Unruptured intracranial aneurysms: a review. J. Neurosurg. 96, 3-42.
6. Parlea, L., Fahrig, R., Holdsworth, D.W., Lownie, S.P., 1999. An analysis of the geometry of saccular intracranial aneurysms. Am. J. Neuroradiol. 20, 1079-1089.
7. Ujiie, H., Tamano, S., Sasaki, K., Hori, T., 2001. Is the aspect ratio a reliable index for predicting the rupture of saccular aneurysm? Neurosurg. 48, 495-503.
8. Satoh, A., Chantrell, R.W., Coverdale, G.N., Kamiyama, S., 1998. Stokesian dynamics simulations of ferromagnetic colloidal dispersions in a simple shear flow. J. Coll. Interf. Sci. 203, 233-248.
9. Satoh, A., 2001. Comparison of approximations between additivity of velocities and additivity of forces for Stokesian dynamics methods. J. Coll. Interf. Sci. 243, 342-350.

10. Kim, S., Karrila, S.J., Microhydrodynamics: Principles and Selected Applications, Butterworth-Heinemann, Stoneham, 1991.
11. Savage, B., Saldivar, E., Ruggeri, Z.M., 1996. Initiation of platelet adhesion by arrest onto fibrinogen or translocation on von Willebrand factor. Cell 84, 289-297.
12. Goto, S., Ikeda, Y., Saldivar, E., Ruggeri, Z.M., 1998. Distinct mechanisms of platelet aggregation as a consequence of different shearing flow conditions. J Clin. Invest. 101, 479-486.
13. Tsubota, K., Wada, S., Kamada, H., Kitagawa, Y., Lima, R., Yamaguchi, T., 2006. A particle method for blood flow simulation, application to flowing red blood cells and platelets. J. Earth Sim. 5, 2-7.
14. Tsubota, K., Wada, S., Yamaguchi, T., 2006. Particle method for computer simulation of red blood cell motion in blood flow. Comp. Meth. Prog. Biomed. 83, 139-146.
15. Tsubota, K., Wada, S., Yamaguchi, T., 2006. Simulation study on effects of deformabilities of red blood cells on blood flow using particle method. Trans. Jap. Soc. Mech. Eng. 72B, 1483-1489.
16. Tsubota, K., Wada, S., Yamaguchi, T., 2006. Simulation study on effects of hematocrit on blood flow properties using particle method. J. Biomech. Sci. Eng. 1, 159-170.
17. Wada, S., Kobayashi, R., 2003. Numerical simulation of various shape changes of a swollen red blood cell by decrease of its volume. Trans. Jap. Soc. Mech. Eng. 69A, 14-21.
18. Koshizuka, S., Oka, Y., 1996. Moving-particle semi-implicit method for fragmentation of incompressible fluid. Nucl. Sci. Eng. 123, 421-434.
19. Kon, K., Maeda, N., Shiga, T., 1987. Erythrocyte deformation in shear flow: influences of internal viscosity, membrane stiffness, and hematocrit. Blood 69, 727-734.
20. Kamada, H., Tsubota, K., Wada, S., Yamaguchi, T., 2006. Computer simulation of formation and collapse of primary thrombus due to platelet aggregation using particle method. Trans. Jap. Soc. Mech. Eng. 72B, 1109-1115.
21. Tsubota, K., Kamada, H., Wada, S., Yamaguchi, T., 2006. Simulation study on effects of elastic red blood cells on primary thrombogenesis using particle method. J. Biomech. 39, 430-431.

MICROSTRUCTURAL MECHANISM OF SKELETAL MUSCLE INJURY AND A NEW CONSTITUTIVE MODEL OF SKELETAL MUSCLE

E. TANAKA, D. ITO, S. YAMAMOTO AND K. MIZUNO

Department of Mechanical Science and Engineering, Nagoya University,
Furo-cho, Chikusa-ku, Nagoya 464-8603, Japan
E-mail: e_tanaka@nagoya-u.jp

This paper concerns with the prediction of mechanical behavior and damage of skeletal muscle. To clarify the mechanism of muscle injury, we conducted biomechanical and pathological evaluations for muscle contusion and strain injury. The results showed correlations between severity of pathological damage and functional disability on contraction. The results also suggested that microscopic damage of muscle fibers, peripheral circulation or motor units has significant effects on the change of macroscopic function. Thus we also performed tensile tests for the microstructure of skeletal muscle and found mechanical properties of muscle fascicle were independent of strain-rate and muscle activation. Based on these experimental evaluations, we developed a new constitutive model of skeletal muscle taking into account viscoelasticity, anisotropy of deformation and damage evolution.

1 Introduction

Soft tissue injury, especially skeletal muscle injury is one of the most important topics in the field of injury prevention. Skeletal muscle injuries are frequently observed in traffic and sports accidents and classified into several injury types depending on the cause of injury. Muscle contusion is caused by impact compression normal to the muscle fiber while strain injury is caused by sudden stretch. It is important to clarify the mechanism of such injuries by considering microstructure of muscle tissue because skeletal muscle has a hierarchical structure of fibrous microstructures. For this purpose, it is also needed to evaluate the mechanical properties of the microstructures of skeletal muscle.

One-dimensional Hill type model has been commonly used for simulations to predict body motion or muscle force. To predict muscle injury by a finite element analysis, however, we need a three-dimensional constitutive model of skeletal muscle to simulate muscle and related injuries. Such a constitutive model will be formulated by considering the hierarchical structure of skeletal muscle and the muscle injury mechanism.

In this paper, we first performed macroscopic muscle injury tests to clarify the injury mechanism. Then we discussed the mechanical properties of the microstructural element of skeletal muscle. Moreover we developed a new constitutive model of skeletal muscle taking into account viscoelastisity, anisotropy of deformation and damage evolution.

2 Mechanical Properties of Skeletal Muscle and Injury Mechanism

We performed macroscopic impact tests for rabbit tibialis anterior muscle to simulate muscle contusion and strain injury. Pathological and mechanical evaluations for such muscle injuries were conducted.

We used tibialis anterior (TA) muscle of female Japanese white rabbit. Twelve rabbits (2.92 ± 0.12 kg, mean ± S.D.) were used for muscle contusion tests, 21 (2.94 ± 0.17 kg) were for strain injury tests and the other 7 (2.88 ± 0.20 kg) were used as the control. This study was approved by Nagoya University Animal Ethics Committee.

2.1 Muscle injury test system and procedure

Firstly, we developed a muscle injury test system for muscle contusion and strain injury tests shown in Figure 1(a) and (b), respectively.

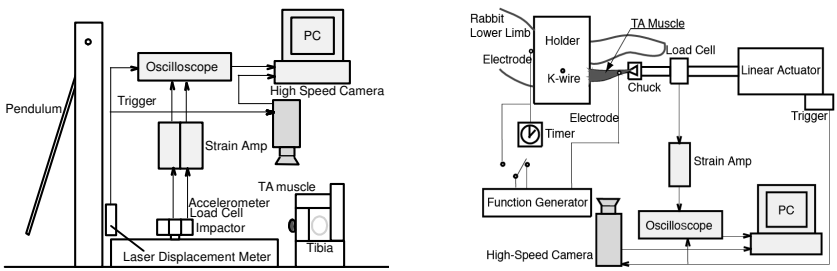

(a) (b)

Figure 1. Schematic diagram of muscle injury test system. (a) Impact test system for muscle contusion. (b) Strain injury test system.

The animals were anesthetized by pentobarbital sodium (30 mg/kg) or isoflurane, after which the TA muscle and deep peroneal nerve were exposed. Two nigrosin markers were added on the surface of the proximal end of the muscle belly and distal tendon to determine the muscle length. The *in situ* length was defined as the distance between two markers at a 90-degree angle to the ankle joint. Next we drilled into the tibial condyle, and a Kirschner's wire (ϕ = 7 mm) was inserted into the hole. Finally, the distal tendon of the TA muscle was cut. The wire in the tibial condyle was fixed on the holder, and the distal tendon was directly gripped by a tooth-like jig.

The muscle was cyclically stretched with 7 mm amplitude (less than 13% strain) at the velocity of 7 mm/s as a preconditioning. Next we performed an isometric contraction test to evaluate the initial contraction force of the specimen. The specimen was activated by an electric pulse with a frequency of 50 Hz during 10 seconds. The voltage of the pulse required for maximum contraction was

determined as tenfold the threshold for twitching. A thin wire electrode for EMG (ST. Steel 7 Strand, Teflon, A-M Systems) was inserted into the distal end of the muscle belly, and another electrode was directly clipped onto the deep peroneal nerve. Then the muscle was damaged by the impact with an impactor (250 g weight, 5 mm width of impact surface) for mucle contusion test, or by applying loading/unloading process of stretching at 200 mm/s for strain injury test in the maximally activated condition.

For a pathological evaluation, the muscle was sliced and stained with hematoxylin and eosin after soaking in formalin more than 1 week. Then we examined severity of muscle contusion microscopically. As mechanical evaluation, we conducted isometric and tensile tests of injured muscles. The injured muscle was elongated at 200 mm/s tensile velocity until break in the activated condition.

2.2 Results of muscle injury tests

Results of the pathological evaluations showed typical three types of injury severity named as Grade I, II and III. Grade I is the case in which no blood bleeding and failure of muscle fiber are observed. Grade II is the case in which sporadic bleeding is observed. In Grade III we observe severe damage spread to whole tissue. Based on these injury grades, the relation between the impact energy and injury severity was evaluated as shown in Figure 2(a). We observe that the two thresholds may exist between Grade I and II and between Grade II and III. Figure 2(b) shows the relation between the changes of the isometric contraction force and the impact energy. The isometric contraction force drops suddenly at the impact energy of about 0.13 J. According to Figure 2(a), this sudden drop is induced in the region of Grade II. The results of the tensile tests, furthermore, showed that the muscles broke at the muscle belly at the energy above 0.13 J, while the muscles applied at less than 0.13 J broke at the muscle-tendon junction (MTJ).

Next we discuss the results of muscle strain injury tests. Results of the pathological evaluations were also divided into 3 grades of severity named as Grade 1, 2 and 3. Grade 1 means no injury. Grade 2 is the case in which some small

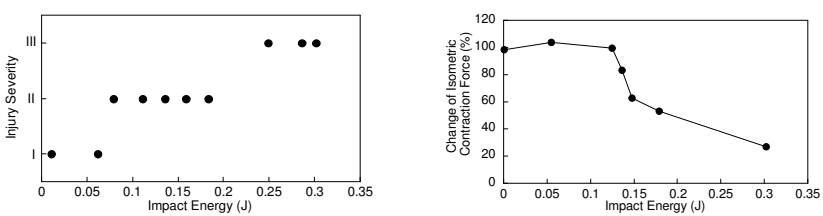

(a) (b)

Figure 2. Results of muscle contusion tests. (a) Relationship between impact energy and injury severity for muscle contusion, (b) Relationship between impact energy and change of isometric contraction force. The threshold of impact energy for decrease of isometric contraction force can be observed around 0.13 J.

inter-fiber blood bleeding is observed. In case of Grade III, blood bleeding and failure of muscle fibers spread over whole tissue. The relationship between the injury severity and absorbed energy during damaging process was shown in Figure 3(a). We can say that the pathological threshold of strain injury exists around 0.25 J, and Grade 2 injury is a transient state between Grade 1 and 3. The isometric contraction force tended to decrease with the increase of the absorbed energy as shown in Figure 3(b). The threshold of decrease of contraction force also existed around 0.25 J. We will continue to discuss the correlation between the pathological and the biomechanical definitions of strain injury.

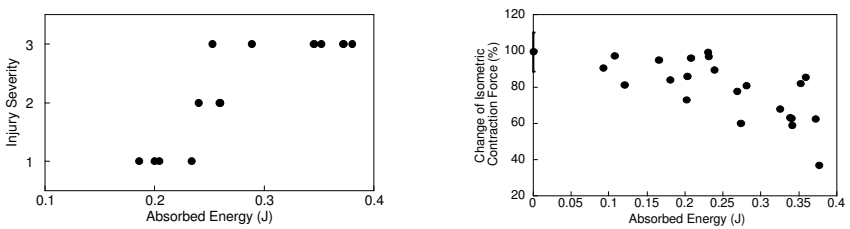

(a) (b)

Figure 3. Results of strain injury tests. (a) Relationship between the applied energy during the induction process of injury and injury severity for strain injury, (b) Relationship between absorbed energy during the induction process of injury and change of isometric contraction force.

The results of tensile tests for damaged muscle, on the other hand, did not show any significant differences against the control group in their failure load and elongation. Therefore strain injury does not cause any significant damage on the mechanical properties of the passive structural elements, because the failure properties of muscle mainly reflects the passive mechanical properties of muscle.

3 Mechanical Properties of Microstructure of Skeletal Muscle

A skeletal muscle has a hierarchical structure that consists of sub-scale fibrous structures such as muscle fascicles or muscle fibers. A muscle fascicle is a bundle of dozens of muscle fibers surrounded by perimysium. A muscle fiber is a myocyte, which is the fundamental system of active contraction and composes of a motor unit combining with a motor neuron.

The results of the muscle injury tests suggested that microscopic damage of muscle fibers, peripheral circulation or motor units has significant effects on the change of macroscopic function. Thus we should discuss the mechanical properties of the microstructures of skeletal muscle to clarify the mechanisms of muscle damage. For this purpose, we developed a micro mechanical test system for the microstructure of skeletal muscle and performed tensile tests for muscle fascicle.

We used muscle fascicles dissected from tibialis anterior (TA) muscle of seven female Japanese white rabbits (2.85 ± 0.18 kg, mean ± S.D.). This study was approved by Nagoya University Animal Ethics Committee.

3.1 Micro mechanical test system and procedure

The developed test system consists of a linear stage driven by a DC micromotor, a micro scale load cell, a high speed camera and a function generator for muscle stimulation. A schematic diagram of the system is shown in Figure 4.

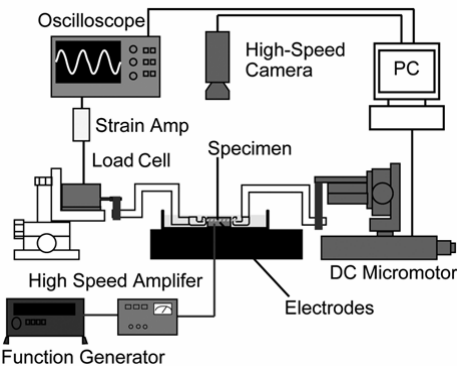

Figure 4. Micro tensile test system. This apparatus consists of a linear stage with DC micromotor (2224-012SR, Faulhaber), a couple of specimen holder, a load cell (LTS-100GA, Kyowa), a digital high-speed camera (FASTCAM-PCI R2, Photoron) and a digital oscilloscope (TDS420A, Sony Tektronix). The load cell detects the load on the muscle fascicle and the data were acquisitioned on the digital oscilloscope. The elongation of the muscle fascicle was calculated from the distance between the nigrosin markers on the surface of the muscle recorded by the digital high-speed camera.

A muscle fascicle was taken from TA muscle carefully and added two markers to define its length. Both ends of the fascicle were attatched to carbon lods by urethan regin, then these carbon lods were held by the specimen holder. The specimen was tensiled in a dish filled with 36°C physiological saline solution. A pair of platinum electrodes were embeded in the dish to apply electrical signal for muscle activation.

Tensile tests were performed with strain-rate 100, 40 or 4%/s in active or passive condition.

3.2 Results of micro mechanical tests of muscle fascicle

Stress-strain curves of muscle fascicle for activated and deactivated conditions were shown in Figure 5(a) and (b), respectively. The results showed that mechanical properties of muscle fascicle are independent of strain-rate and muscle activation.

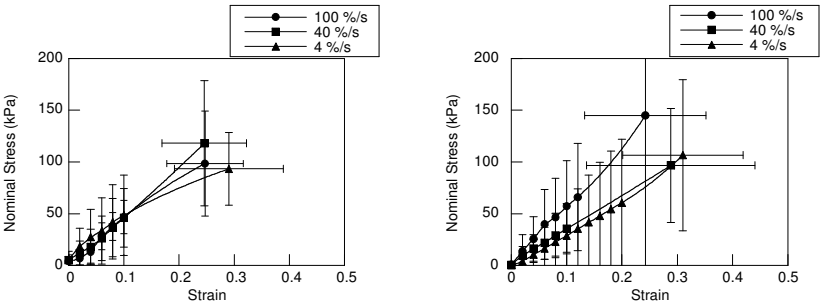

Figure 5. Results of micro mechanical tests of muscle fascicle. (a) Stress-strain curves in active condition, (b) Stress-strain curves in passive condition.

4 Formulation of a Constitutive Model

In this section we develop a three-dimensional constitutive model of skeletal muscle taking into account the microstructures of muscle. Viscoelastisity, anisotropy of deformation and damage evolution are also taken into account.

4.1 Free energy function and hypothesis of total energy equivalence

To take into account material anisotropy, viscoelasticity and damage of muscle tissue, we referred to the approach used previously to represent arterial walls (Holzapfel et al. [1][2]). Since the muscle tissue can be assumed an incompressible material, we divide the deformation gradient tensor into a volume-changing part and a volume-preserving part referring to Flory [3];

$$\mathbf{F} = J^{1/3}\bar{\mathbf{F}}, \quad \mathbf{C} = J^{2/3}\bar{\mathbf{C}} \tag{1}$$

where J is $\sqrt{\det \mathbf{C}}$ and denotes the relative change in volume. We have defined the modified deformation gradient $\bar{\mathbf{F}}$ and the modified right Cauchy-Green tensor $\bar{\mathbf{C}}$, with the conditions $\det \bar{\mathbf{F}} = (\det \bar{\mathbf{C}})^{1/2} = 1$. Thus the free energy function is described as the sum of volumetric $\Psi^{\infty}_{\mathrm{vol}}$, isochoric elastic $\Psi^{\infty}_{\mathrm{iso}}$ and isochoric viscoelastic parts Υ:

$$\begin{aligned}&\Psi\left(\mathbf{C}, \mathbf{A}, \boldsymbol{\Gamma}_1 \cdots \boldsymbol{\Gamma}_m, \mathbf{D}; \alpha\right) \\ &\quad = \Psi^{\infty}_{\mathrm{vol}}\left(J\right) + \Psi^{\infty}_{\mathrm{iso}}\left(\bar{\mathbf{C}}, \mathbf{A}, \mathbf{D}; \alpha\right) + \Upsilon\left(\bar{\mathbf{C}}, \mathbf{A}, \bar{\boldsymbol{\Gamma}}_1, \cdots, \bar{\boldsymbol{\Gamma}}_m, \mathbf{D}\right)\end{aligned} \tag{2}$$

where $\mathbf{A}$ is a structural tensor of order two to describe transverse isotropy. The (second-order) tensorial variables $\bar{\boldsymbol{\Gamma}}_i \ (i = 1, \ldots, m)$ are akin to $\bar{\mathbf{C}}$ and characterize the isochoric viscoelastic response of the material. In addition the parameter α denotes the activation level of muscle fiber.

Based on the framework of continuum damage mechanics, the anisotropic damage of muscle tissue is expressed by a second–order damage tensor **D**. As the first step, we assume that the damage tensor **D** also possesses transversely isotropic properties, and has the same principal axes with those of **A**. Thus the damage tensor **D** is represented by

$$\mathbf{D} = D_1\mathbf{A} + D_2(\mathbf{I} - \mathbf{A}) \tag{3}$$

where D_1 and D_2 are the principal values of damage tensor **D**. The D_1 represents the damage of cross-sectional area perpendicular to the fiber direction and expresses fiber failure. The D_2 represents damage in the plain including fiber and expresses detachment among fibers. According to the hypothesis of total energy equivalence [4] (Figure 6), the free energy of damaged tissue can be obtained as

$$\Psi(\mathbf{C}, \mathbf{A}, \boldsymbol{\Gamma}_1 \cdots \boldsymbol{\Gamma}_m, \mathbf{D}; \alpha) = \Psi\left(\tilde{\mathbf{C}}, \mathbf{A}, \tilde{\boldsymbol{\Gamma}}_1 \cdots \tilde{\boldsymbol{\Gamma}}_m, \mathbf{D} = \mathbf{0}; \alpha\right) \tag{4}$$

where $\tilde{\mathbf{C}}$ and $\tilde{\boldsymbol{\Gamma}}_i$ are the effective Cauchy-Green tensor and the effective internal variables defined by;

$$\tilde{\mathbf{C}} = \mathbf{M}(\mathbf{D})^{-1} : \mathbf{C}, \quad \tilde{\boldsymbol{\Gamma}}_i = \mathbf{M}(\mathbf{D})^{-1} : \boldsymbol{\Gamma}_i \tag{5}$$

Here

$$\mathbf{M}(\mathbf{D}) = \frac{1}{2}\left[\boldsymbol{\Phi} \underline{\otimes} \boldsymbol{\Phi} + \boldsymbol{\Phi} \overline{\otimes} \boldsymbol{\Phi}\right], \quad \boldsymbol{\Phi} = (\mathbf{I} - \mathbf{D})^{-1/2} \tag{6}$$

is a fourth-order damage effective tensor to translate strain and stress tensor to effective tensor variables [5]. Note that symbols $\underline{\otimes}$ and $\overline{\otimes}$ express the following:

$$\mathbf{A} \underline{\otimes} \mathbf{B} = A_{ik}B_{jl}\mathbf{e}_i \otimes \mathbf{e}_j \otimes \mathbf{e}_k \otimes \mathbf{e}_l, \quad \mathbf{A} \overline{\otimes} \mathbf{B} = A_{il}B_{jk}\mathbf{e}_i \otimes \mathbf{e}_j \otimes \mathbf{e}_k \otimes \mathbf{e}_l \tag{7}$$

The volumetric part in Equation (2) or (4) is described with volumetric change J (Holzapfel et al. [6]):

$$\Psi_{\text{vol}}^{\infty}(\tilde{J}) = \kappa \mathsf{G}(\tilde{J}), \quad \mathsf{G}(\tilde{J}) = \frac{1}{\beta^2}\left[\beta \ln \tilde{J} + \frac{1}{\tilde{J}^{\beta}} - 1\right], \quad \beta > 0 \tag{8}$$

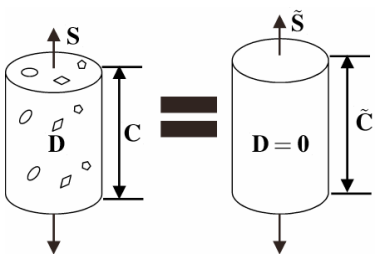

Figure 6. Schematic diagram of hypothesis of total energy equivalence.

The isochoric part is separated into response of shearing along fibers, shearing transverse to the fibers, and stretch in the muscle fibers, referring to Blemker et al. [7].

$$\Psi_{\text{iso}}^{\infty} = W_1\left(\tilde{\bar{I}}_4, \tilde{\bar{I}}_5\right) + W_2\left(\tilde{\bar{I}}_1, \tilde{\bar{I}}_4, \tilde{\bar{I}}_5\right) + W_3\left(\tilde{\bar{I}}_4, \alpha\right) \tag{9}$$

where $\tilde{\bar{I}}_1, \tilde{\bar{I}}_4, \tilde{\bar{I}}_5$ are basic and additional invariants of $\tilde{\bar{\mathbf{C}}}$ defined by

$$\tilde{\bar{I}}_1 = \operatorname{tr}\tilde{\bar{\mathbf{C}}}, \quad \tilde{\bar{I}}_4 = \tilde{\bar{\mathbf{C}}} : \mathbf{A}, \quad \tilde{\bar{I}}_5 = \tilde{\bar{\mathbf{C}}}^2 : \mathbf{A} \tag{10}$$

The functions W_1 and W_2 represent the along-fiber and cross-fiber strain energy, respectively. The functional forms adopted for our model are as follows:

$$W_1 = G_1(B_1)^2, \quad W_2 = G_2(B_2)^2 \tag{11}$$

where G_1 and G_2 represent the effective along-fiber and the effective cross-fiber shear modulus. Two new strain invariants B_1 and B_2 introduced by Criscione et al. [8] represent the intramuscular connective tissue's resistance to along-fiber shear and cross-fiber shear, respectively. The B_1 and B_2 are written in the form

$$B_1 = \sqrt{\frac{\tilde{\bar{I}}_5}{\tilde{\bar{I}}_4^{\,2}} - 1}, \quad B_2 = \cosh^{-1}\left(\frac{\tilde{\bar{I}}_1\tilde{\bar{I}}_4 - \tilde{\bar{I}}_5}{2\sqrt{\tilde{\bar{I}}_4}}\right) \tag{12}$$

The term W_3 defines the relationship between the fiber stress, the fiber stretch λ and the activation level α:

$$\lambda\frac{\partial W_3}{\partial \lambda} = \sigma_{\max} f_{\text{total}}^{\text{fiber}}(\lambda, \alpha)\frac{a(\lambda_{\text{ofl}})}{a(\lambda)} \tag{13}$$

where the normalized function $f_{\text{total}}^{\text{fiber}}$ is defined as the sum of the passive part and the active part, and represented by

$$f_{\text{total}}^{\text{fiber}}(\lambda, \alpha) = f_{\text{passive}}^{\text{fiber}}(\lambda) + \alpha f_{\text{active}}^{\text{fiber}}(\lambda) \tag{14}$$

The constant λ_{ofl} in Equation (13) is the optimal fiber length. Parameters of $a(\lambda)$ and $a(\lambda_{\text{ofl}})$ are the cross-sectional area of the fibers at the stretch λ and λ_{ofl}, respectively.

The viscoelastic part of Equation (2) is modeled as a three-dimensional viscoelastic model that is constructed by extending one-dimensional rheological model, as illustrated in Figure 7,

$$\Upsilon = \sum_{i=1}^{m}\Upsilon_i, \quad \Upsilon_i = \frac{1}{2}\tilde{\bar{\mathbf{\Gamma}}}_i : \mathbf{J}_i : \tilde{\bar{\mathbf{\Gamma}}}_i \quad (i; \textit{no sum}) \tag{15}$$

where $\mathbf{J}_i$ is a fourth-order positive definite symmetric tensor related to viscoelastic modulus.

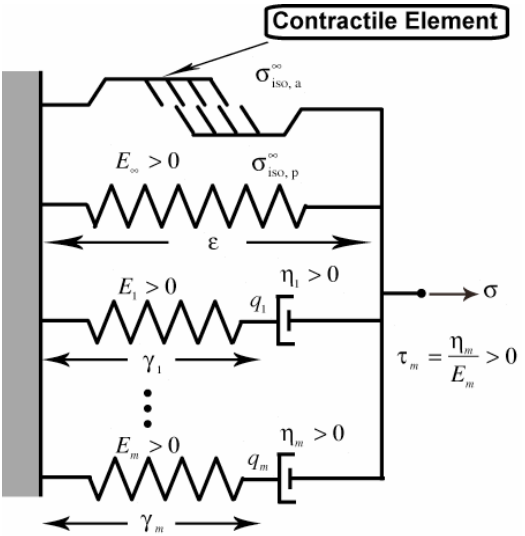

Figure 7. Rheological model with contractile element.

4.2 Damage evolution

Based on the assumption (3), the directions of the principal axes of damage tensor **D** is kept in the directions of those of **A**. When we further assume that the damage evolution is governed by the current states of Green's strain $\mathbf{E}$ $(=(1/2)(\mathbf{C}-\mathbf{I}))$, Green's strain-rate $\dot{\mathbf{E}}$ and damage **D**, by use of the representation theorem for tensor functions [9] we can derive the evolution equations for $\dot{\mathbf{D}}$ in the form:

$$\dot{\mathbf{D}} = \alpha_1 \mathbf{I} + \alpha_2 \mathbf{A} = (\alpha_1 + \alpha_2)\mathbf{A} + \alpha_1(\mathbf{I} - \mathbf{A}) \tag{16}$$

$$\alpha_1 = \alpha_1(\text{tr } \mathbf{D}, \text{tr } \mathbf{E}, \text{tr } \dot{\mathbf{E}}, \text{tr } \mathbf{AD}, \text{tr } \mathbf{AE}, \text{tr } \mathbf{A}\dot{\mathbf{E}}) \tag{17}$$

$$\alpha_2 = \alpha_2(\text{tr } \mathbf{D}, \text{tr } \mathbf{E}, \text{tr } \dot{\mathbf{E}}, \text{tr } \mathbf{AD}, \text{tr } \mathbf{AE}, \text{tr } \mathbf{A}\dot{\mathbf{E}}) \tag{18}$$

where α_1 and α_2 are scalar functions of the scalar invariants $\mathbf{A}, \mathbf{D}, \mathbf{E}, \dot{\mathbf{E}}$. The function α_1 represents the isotropic damage evolution and α_2 expresses the evolution of decrease of cross-sectional area perpendicular to the fiber direction. Thus we represent α_1 by isotropic invariants $\text{tr}\,\mathbf{D}$, $\text{tr}\,\mathbf{E}$, $\text{tr}\,\dot{\mathbf{E}}$, and α_2 by $\text{tr}\,\mathbf{AD}$, $\text{tr}\,\mathbf{AE}$, $\text{tr}\,\mathbf{A}\dot{\mathbf{E}}$. By examining the experimental data mentioned above, we formulated the following expressions for α_1 and α_2

$$\alpha_1 = a_1 \exp(b_1 \text{tr } \mathbf{D}) \cdot \langle \text{tr } \mathbf{E} \rangle \cdot \langle \text{tr } \dot{\mathbf{E}} \rangle \tag{19}$$

$$\alpha_2 = a_2 \exp(b_2 \text{tr } \mathbf{AD}) \cdot \langle \text{tr } \mathbf{AE} - \varepsilon_{yield} \rangle \cdot \langle \text{tr } \mathbf{A}\dot{\mathbf{E}} \rangle \tag{20}$$

where a_1, b_1, a_2 and b_2 are material constants, and ε_{yield} is the threshold value of the damage generation for fiber stretch. The symbol < > denotes Macaulay bracket defined by

$$\langle x \rangle = \begin{cases} x & \text{when} \quad x \geq 0 \\ 0 & \text{when} \quad x < 0 \end{cases} \tag{21}$$

These equations represent that muscle tissue damage evolves only if stretch exceeds the threshold.

4.3 Applicability of the proposed model

In order to examine the applicability of the proposed constitutive model, we reproduced our experimental results for tensile tests of muscle fascicle mentioned above by use of our model. In the calculation, muscle tissue was assumed to be fully incompressible, for simplicity. Figure 8 shows simulation results of the stress-strain curves at the strain-rate of 100, 40 or 4%/s in the active or in the passive condition together with the corresponding experimental results. The simulation results show good agreements with the experimental data. This means the model can represent the dependence of stress on the strain-rate and the muscle activation, especially at the region of low stretch ratio.

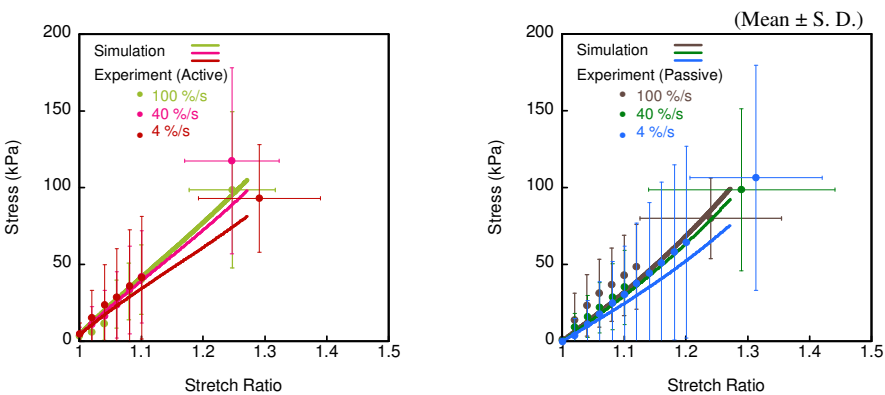

Figure 8. Comparison between the stress-strain curves of muscle fiber with and without damage evolution (left: active condition, right: passive (non-active) condition).

5 Conclusions

The biomechanical and pathological evaluations for muscle contusion and strain injury were conducted. The results showed significant correlations between injury severity and functional disability of muscle. The results also suggested that the

injury mechanism is closely related with microscopic damage. The tensile tests for microstructural elements of skeletal muscle were also performed and found the mechanical properties of muscle fascicle were independent of strain-rate and muscle activation. Finally we formulated a new constitutive model of skeletal muscle taking into account viscoelasticity, anisotropy of deformation and damage evolution and showed the proposed model can describe the stress-strain curves of muscule fascicle well.

Acknowledgments

We thank Drs. Shogo Tokudome and Masahito Hitosugi for their contributions and advices for pathological evaluations, and Biomechanics laboratory of Toyota Central R&D Labs., Inc. for their collaborations for the development of the experimental apparatus, and Mr. Atsushi Hayakawa, Tsuyoshi Taniguchi, Iku Nishizawa, Yuji Tokoro, Arata Kawakami for their great efforts for animal experiments. This work was supported in part by a Grant-in-Aid for Scientific Research on Priority Areas (No. 15086208) from the Ministry of Education, Culture, Sports, Science and Technology of Japan.

References

1. Holzapfel, G.A., Gasser, T.C., Stadler, M., 2002. A structural model for the viscoelastic behavior of arterial walls: Continuum formulation and finite element analysis. Eur. J. Mech. A/Sol. 21, 441-463.
2. Holzapfel, G.A., Gasser, T.C., 2001. A viscoelastic model for fiber-reinforced composites at finite strains. Comput. Methods Appl. Mech. Eng. 190, 4379-4403.
3. Flory, P.J., 1961. Thermodynamic relations for highly elastic materials. Trans. Faraday Soc. 57, 829-828.
4. Saanouni, K., Forster, Ch., Ben Hatira, F., 1994. On the anelastic flow with damage. Int. J. Damage Mech. 3, 140-169.
5. Chow, C.L., Wang, J., 1987. An anisotropic theory of continuum damage mechanics for ductile fracture. Eng. Fract. Mech. 27, 547-558.
6. Holzapfel, G.A., 1996. On large strain viscoelasticity: Continuum formulation and finite element application to elastomeric structures. Int. J. Numer. Methods Eng. 39, 3903-3926.
7. Blemker, S.S., Pinsky, P.M., Delp, S.L., 2005. A 3D model of muscle reveals the causes of nonuniform strains in the biceps brachii. J. Biomech. 38, 657-665.
8. Criscione, J.C., Douglas, A.S., Hunger, W.C., 2001. Physically based strain invariant set for materials exhibiting transversely isotropic behavior. J. Mech. Phys. Sol. 49, 871-897.
9. Zheng, Q.S., 1994. Theory of representations for tensor functions—A unified invariant approach to constitutive equations. Appl. Mech. Rev. 47, 544-587.

MECHANICAL CHARACTERISTICS OF VASCULAR CELLS AND TISSUES EXPOSED TO DEFORMATION, FREEZING AND SHOCK WAVES: MEASUREMENTS AND THEORETICAL PREDICTIONS

H. YAMADA, M. TAMAGAWA AND H. ISHIGURO

Department of Biological Functions and Engineering, Kyushu Institute of Technology, 2-4 Hibikino, Wakamatsu-ku, Kitakyushu 808-0196, Japan
E-mail: yamada@life.kyutech.ac.jp

In this paper, we describe experimental evidence and theoretical simulations related to the effects of mechanical changes on vascular tissues and endothelial cells. First, we examined the response to cyclic stretching and quasi-static stretching using confocal laser-scanning microscopy (CLSM) to measure the orientation of actin stress fibers, measured in the apical and basal regions of the cell. These results were compared with the predictions made using a strain-limit hypothesis, and CLSM image slices of a cell were used to reconstruct a finite-element model of a whole cell body. This model accurately predicted the cellular deformation under substrate stretching. Second, we measured the stress-strain relationship under tensile loading after freezing and thawing of the tissues. The stress-strain relationship was described by a mathematical model in which the total force is the sum of the forces of the elastic and collagen fibers and the pressure of a fluid phase. The tissue stiffening caused by freezing was described by a shift in the probability density distribution of the natural lengths of the collagen fibers. Also, we investigated microscopically the freezing behavior of vascular tissues and the subsequent histologicval change. Finally, we determined the endothelial cell population in suspension and used real-time PCR to quantify gene expression. Application of plane shock waves to suspended cells caused the cells to increase their growth rate.

1 Introduction

The mechanical properties of vascular tissues and cells can be informative measures of various changes associated with cell damage. Damage can occur not only under extraordinary circumstances (in an unusual environment), but also under normal physiological conditions. In this report, we demonstrate some approaches for modeling and measuring mechanical changes in cytoskeletal and cellular responses to substrate stretching (Section 2), in the response of tissue to freezing (Section 3), and in the response of suspended cells to shock waves (Section 4).

Because changes in the internal structure of cells or tissues change the mechanical properties of those cells or tissues, the mechanical behaviors of the cells and tissues also change, even when subjected to the same boundary conditions. Results from finite-element analysis using a strain energy-density function for an aortic endothelial cell are described below in Section 2, and theoretical freezing effects on the stress-strain relationship, microstructure, and histological characteristics of porcine aortic tissue are described in Section 3. Mathematical modeling and theoretical simulations for vascular tissues and cells might aid medical diagnosis and treatment or the design of industrial products for medical use.

2 Cellular Response to Substrate Stretching

2.1 Reorientation of actin stress fibers in response to cyclic stretching

Cells and their intracellular components respond to mechanical changes in their environment, such as cyclic stretching and fluid shear stress [1–3]. Takemasa et al. [1] previously showed experimental evidence that actin stress fibers (SFs), which are bundles of actin filaments, orient in the direction of least substrate strain. Under cyclic uniaxial stretch conditions, SFs are generally thought to be located in the basal region of the cell and not in other regions. An exception was reported by Wang et al. [4], who found that actin filaments form tent-like structures in which the filaments connect the apical and basal membranes.

Yamada and co-workers [5, 6] reproduced the off-plane orientation of SFs under various types of cyclic biaxial stretching using a numerical simulation based on the hypothesis that SFs orient so as not to exceed a strain limit (*e.g.*, 5%). Results from the numerical simulation of the three-dimensional (3D) orientation of SFs suggest that SFs may adopt off-plane orientations under various types of stretching.

Yamada and Ando [3] carried out experiments to elucidate the 3D location and orientation of SFs. They applied uniaxial cyclic stretching to a silicone chamber substrate on which porcine aortic endothelial cells were seeded. The cells adhered to the substrate by virtue of the fact that the substrate was coated with fibronectin. They prepared two cell populations, subconfluent cells (25,000 to 27,000 cells/cm^2) and isolated cells (5,000 to 8,000 cells/cm^2). Each cell population was further divided into one of two sub-populations, according to the distribution pattern of SFs; either the SFs were observed in the apical and basal regions or they were observed only in the basal region. For the isolated cell sub-population exhibiting both apical and basal SFs, the averaged angles of these fibers were 74.8 and 74.2 degrees, respectively, a difference that was not statistically significant ($p > 0.01$). For the isolated sub-population with basal SFs only, the averaged angle of the basal SFs was 86.8 degrees, which differed in a statistically significant manner ($p < 0.01$) from the basal SF angle found for the other isolated-cell sub-population above (74.2 degrees).

In the subconfluent cells with both apical and basal SFs, the averaged angles of these SFs were 73.0 and 70.5 degrees, respectively, and the difference between these angles was statistically significant. In the subconfluent cells with basal SFs only, the average angle of the basal SFs was 70.2 degrees, which was not statistically different from the average angle found for the basal SFs in the other subconfluent-cell sub-population above (70.5 degrees).

Deformation of the substrate allows us to estimate the SF orientation angles associated with various SF stretch values on a 15%-stretched substrate at the maximally stretched state of the substrate (See Fig. 1). A comparison of the experimental and theoretical results indicates that the orientation of SFs in the apical and basal regions of cells is modulated by the deformation of the substrate. The

deformation field in the cell is not the only factor that determines the orientation of SFs [6]. Other chemical and physical factors should be incorporated into the theoretical model if is to accurately describe actin cytoskeletal remodeling.

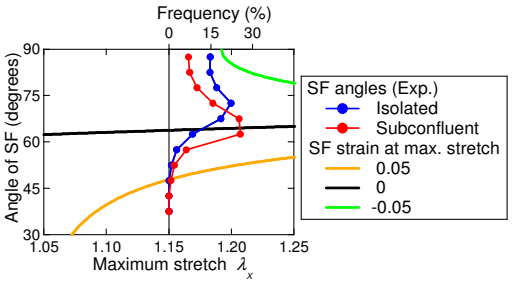

Figure 1. Theoretical estimation of the angles of a SF at strains 0, 0.05 and -0.05 when the substrate is stretched by 15% in the *X* direction with an associated 4% compressive strain in the *Y* direction. The SF orientations reported by Yamada and Ando [3] for isolated and subconfluent cells are also plotted.

2.2 *Finite-element modeling of an adherent endothelial cell*

Caille et al. [7] modeled a single endothelial cell as a neo-Hookean material based on their compression test results. Yamada and Matsumura [8] created an axisymmetric finite-element model with cytoplasm, nucleus, and substrate, and Yamada et al. [9] created a nucleus-free model with a solid cell membrane, fluid-filled cytoplasm, and substrate. Comparisons of these models are shown in [10].

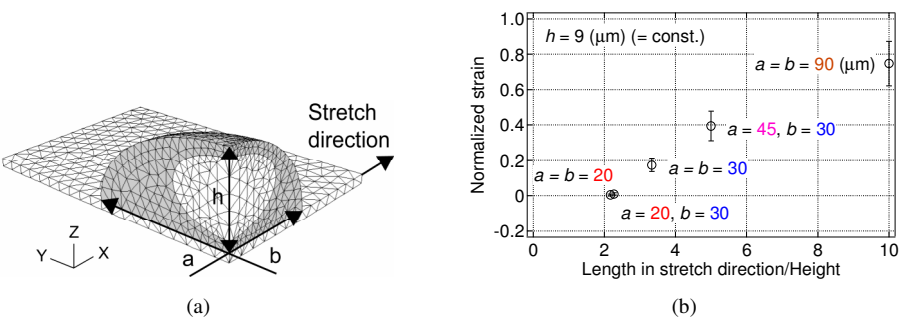

Figure 2. (a) Finite-element model of length (*a*, *b*) and height *h*. (b) Two-dimensional maximal principal strains normalized by the strain applied to the substrate for various pairs of cell lengths in the region of > 90% of cellular height under 10% pure uniaxial stretch of the substrate in the *X* direction [11].

Yamada and Kageyama [11] demonstrated the dependence of the cell models on geometry. Figure 2 shows the 2D maximal principal strains normalized by the strain applied to the substrate for various pairs of cell lengths (*a*, *b*) in the region of

> 90% of the cellular height under 10% pure uniaxial stretching of the substrate in the *X* direction. The results show that the length in the stretch direction, *a*, affects the cellular strain, whereas the length in the transverse direction, *b*, does not.

Yamada and co-workers [12, 13] reconstructed the three-dimensional geometry of substrate-adhered endothelial cells using slice images obtained by CLSM (See Fig. 3). By comparing the experimentally determined contours of the cell on a 15%-stretched substrate with the deformed shape of the finite-element model, they showed that the incompressible isotropic hyperelastic model describes the cellular deformation under the deformation of the substrate with sufficient accuracy. Yamada and Nobuhara [14] have produced a finite-element model of a whole cell body, which consists of the cytoplasm and the nucleus. This technique will lead to an image-based finite-element analysis of the cell body with the nucleus.

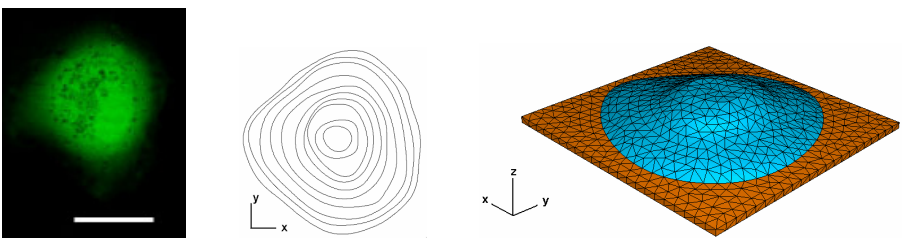

(a) (b) (c)

Figure 3. Process for modeling a three-dimensional cell [12]. (a) Image of the cellular bottom. The cell is stained with Calcein-AM. Bar: 50 μm. (b) Contour map of the cell. The interval is 0.5 μm. (c) Finite-element model.

3 Tissue Response to Freezing

3.1 Freezing-induced changes in the stress-strain relationship of vascular tissue

Freezing of living tissues is one of the fundamental techniques used to prolong the viability of their biological functions. However, freezing and thawing alter the mechanical properties of vascular tissues [15, 16]. Using an uniaxial cyclic-loading test, Venkatasubramanian et al. [15] obtained the stress-strain relationship of ring-shaped specimens excised from porcine femoral arteries after freezing (–80°C) and thawing. They found that freezing had a stiffening effect on the vascular tissue.

Yamada and co-workers [16] carried out cyclic uniaxial-loading tests on ring-shaped specimens excised from porcine thoracic aortas. Whereas the femoral artery, which is categorized as a muscular artery, exhibits significant hysteresis under cyclic loading, the thoracic aorta is categorized as an elastic artery and exhibits negligible hysteresis under cyclic loading. In the experiment of Yamada et al., each specimen was load-tested three times: first, before the process of freezing and thawing; second,

after the process of freezing and thawing; and third, while stretched almost to the breaking point. The deformations of the tissue before and after freezing were similar at low stress levels, *i.e.*, in the toe region of the stress-strain curve, and freezing and thawing caused stiffening to appear at the transient phase of the stress-strain curve (Fig. 4).

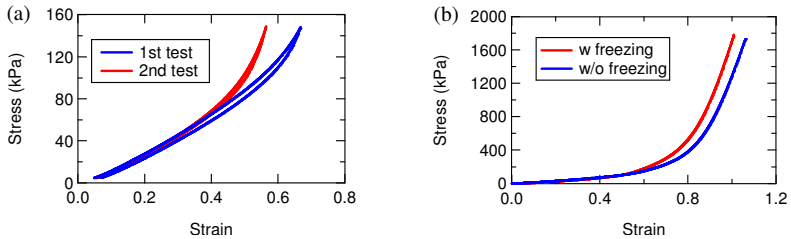

Figure 4. (a) Typical example of the nominal stress-strain relationships of the aorta under uniaxial cyclic loadings with a constant strain rate (1%/sec) before (first test) and after (second test) the process of freezing and thawing (cooling rate: –1°C/min) [16]. The strain in the second test was calculated using the reference length in the first test. (b) Following the second test, each specimen (one but not the other processed with freezing) was stretched almost to the breaking point in a third test [16].

3.2 Mathematical description of the stress-strain relationship of the vascular tissue

Yasuno and Yamada [17] have produced a mathematical model that takes the fibrous structure of the aortic wall into account in describing its stress-strain relationship. In the model, the natural lengths of the elastic and collagen fibers are assumed to be distributed symmetrically (See Fig. 5). The compressive elastic modulus is assumed to be much lower than the tensile modulus for the elastic fibers and to be zero for the collagen fibers. They also assume that all the collagen fibers remain relaxed until all the elastic fibers are stretched, and that the tensile elasticity

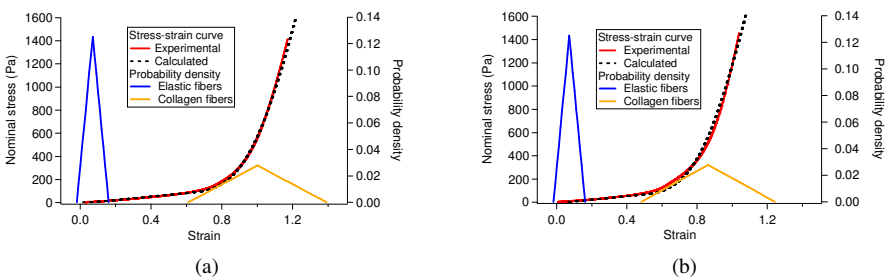

Figure 5. Comparisons of the experimental and theoretical simulation results of the stress-strain relationship of the porcine thoracic aorta under uniaxial loading. The probability density distributions of the elastic and collagen fibers are also shown [17]. (a) Without freezing and thawing. (b) With freezing and thawing.

of the collagen fibers is much stiffer than that of the elastic fibers. The internal force of the vascular wall is expressed as the sum of the force of these fibers and the pressure of a fluid phase, the compressibility of which was defined by a bulk modulus. A comparison of the experimental [16] and theoretical simulation results of the stress-strain relationships of the porcine thoracic aorta with or without freezing and thawing is shown in Fig. 5. The model described the stress-strain relationship, which consists of a toe region and a steep region, and the change in stress-strain relationship (from (a) to (b) in Fig. 5) was expressed by shifting the probability density distribution of the collagen fibers to a shorter length.

3.3 Freezing behavior and histological change in vascular tissue

3.3.1 Materials and methods

Samples were excised from fresh porcine aorta and frozen at one of the following cooling rates: 0.5, 50, or 100°C/min. Ice crystal morphology in the frozen samples, histological morphology, and histological change in tissue constituents were imaged using a cryo-scanning electron microscope, and a field emission scanning electron microscope (FE-SEM) for higher magnification. An optical microscope was also used to examine a section of a frozen sample prepared using the method improved upon in this study [17].

3.3.2 Results and discussion (Fig. 6)

In fresh aortic control tissue, continuous elastic lamellae were uniformly and circumferentially distributed, with intertwined smooth muscle cells and collagen fibers filling the gaps between lamellae.

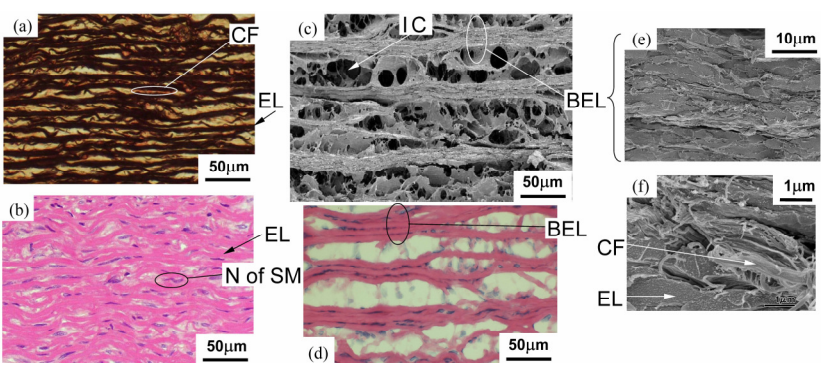

Figure 6. Images of the vascular cross section. (a) Elastica-van Gieson stain (control), (b) Hematoxylin-eosin (HE) stain (control), (c), (e), (f) FE-SEM images of samples frozen at 0.5°C/min, (d) HE stain of a section frozen at 0.5°C/min. Abbreviations: EL, elastic lamella; BEL, bundle of elastic lamellae; SM, smooth muscle cell; N, nucleus; CF, collagen fiber; and IC, ice crystal.

At the lowest cooling rate, bundles of several elastic lamellae formed, with ice crystals growing between bundles. The smooth muscle cells in the gaps were dehydrated and torn, allowing a bridge of broken cytoplasm to form across the gaps. In tightly packed lamellar bundles, the dehydrated and flattened smooth muscle cells and collagen fibers were packed together between lamellae. After freezing and thawing, the formation of cracks, destruction of smooth muscle cells, fragmentation of cytoplasm, and distension of nuclei were observed. Fine elastic fibers were fragmented, with collagen fibers pushed away and unevenly distributed on lamellar surfaces. Higher cooling rates mitigated changes due to the freezing in the microstructure and histological constituents.

4 Cellular Response to Shock Waves

4.1 Materials and methods

Endothelial cells were taken from a pig aorta lumen by abrading with knife. The cells were cultured in a dish filled with DMEM (GIBCO) including 10% FBS and 1% PSN [penicillin-streptomycin] antibiotic mixture in a CO_2 incubator at 37°C, 100% humidity, and 5% CO_2. Cells were subcultured when they were 70% confluent and shock-wave tested when at passage 3–6. A "shock tube" was used to generate shock waves for application to the cells (Fig. 7(a)). The advantageous features of the shock tube apparatus [19] are: (*i*) the propagation wave is plane and (*ii*) the duration time is long (tens of milliseconds) compared with that of laser and focusing shock waves (several μs). As shown in the schematics in Fig. 7(a), the plane shock wave propagates into the sample located at the wall end after passing through several valve operations.

In these experiments, the cells were suspended in the culture medium (Fig. 7(b)). The experimental conditions for the shock waves were: pressure ratio in the apparatus, 4; Mach number in air, 1.4; pulse number 1–5. The interval time for each shock-wave pulse was 10–30 sec. The pressure of the incident shock wave in air was estimated to be 0.2 MPa by considering the wave reflection, and its pressure in water was estimated to be about 0.4 MPa. The thickness of the shock wave in water is not known, but it is usually taken as several μm. After the suspended cells were bombarded with shock waves, their disintegration rate and cell growth (population) were investigated. Every test was performed with at least one control and one shock wave-treated sample.

4.2 Results and discussion

In assessing the cell population in the phase-contrast image, the dependence of the rate of cell disintegration α (normally from 0 to 5%) on the number of shock-wave

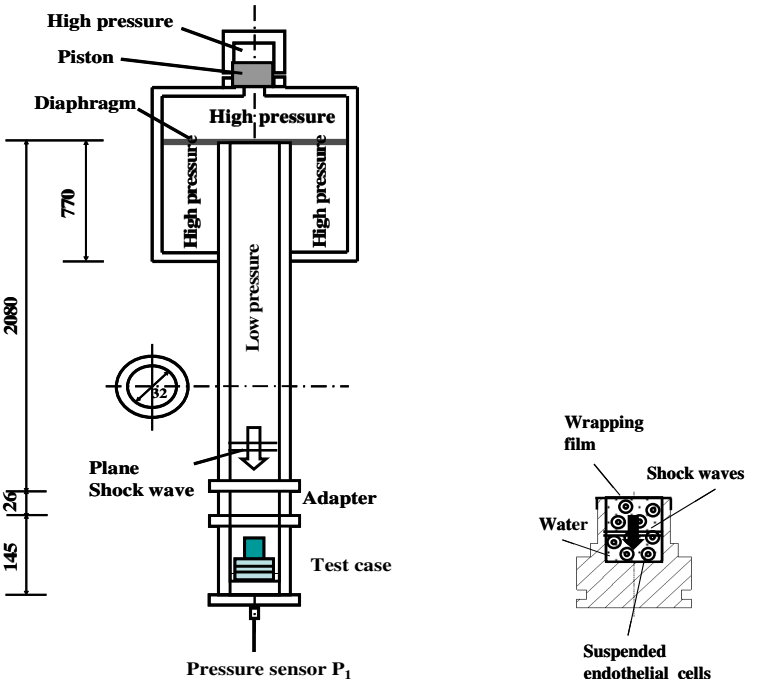

Figure 7. Experimental apparatus for working shock waves on the cells. (a) Diaphragmless shock tube for bio-tests. (b) Detail portion of test case.

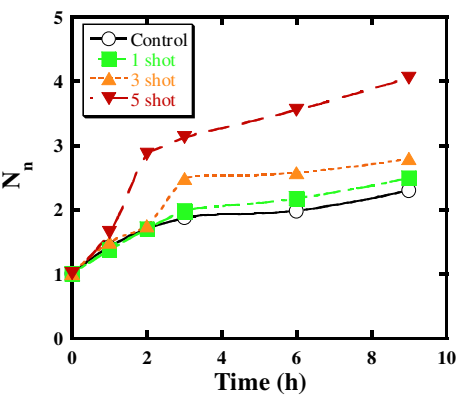

Figure 8. Dependence of the dimensionless cell population with changing number of pulses.

pulses must be considered according to the formula:

$$N_n = \frac{NS_n}{NS_0} \times (1 - \alpha) . \quad (1)$$

Here NS_n and NS_0 are the cell population at n and zero hours, respectively, and N_n is the normalized cell population. The change in the dimensionless cell population N_n with pulse number is plotted in Fig. 8, which shows that the population of shock wave-treated cells was higher than that of control cells. From 0–4 h, the growth rate of the shock wave-treated cells was high compared with that of the controls. In particular, for passage-3 cells, the population rapidly increased after five shock-wave pulses. In examining the effects of passage number on cell population, we found that, within several hours of treatment, the passage-3 cell population was about twice that of the passage-6 population, indicating that cells of lower passage number proliferated more quickly.

These results raise the issue of the nature of the mechanical stimulus. The thickness of the shock wave and the size of the cells were of roughly the same scale (several μm). Therefore, once the shock wave was applied to the cell membrane, proteinaceous sensors on the cell membrane may have detected the pressure gradient (normal stress and shear stress) and signaled the cell interior. This possibility was confirmed using real-time PCR to quantify gene expression related to cell growth; this test showed that gene expression was enhanced by plane shock waves.

5 Conclusions

We performed experimental measurements, mathematical modeling, and theoretical simulations of vascular cells and tissues, focusing on the effects of substrate deformation on cellular and intracellular behavior, the effects of freezing and thawing on the mechanical properties, microstructure and histological characteristics of vascular tissues, and the effects of shock-wave treatment on the cellular response. The following conclusions can be drawn:

1. Actin stress fibers in cultured aortic endothelial cells reorient by responding to the cyclic deformation of the substrate, both in the apical and basal regions of the cell. The orientation angle within the horizontal plane falls within the range predicted by the strain-limit hypothesis.
2. Deformation of cultured aortic endothelial cells agrees well with the results predicted using an incompressible, isotropic, hyperelastic material as a model of the cell adhered to the substrate.
3. Freezing and thawing cause stiffening of elastic aortic tissues. The stress-strain relationship under uniaxial loading was formulated as a mathematical model with

fibers and a fluid phase, and the stiffening was expressed by shifting the distribution of the natural lengths of collagen fibers toward shorter fibers.

4. Freezing behavior of vascular tissue was dependent on the histological structure and cooling rate. The subsequent histological change of vascular tissue was dependent on the cooling rate. Higher cooling rates mitigated changes due to the freezing in the microstructure and histological constituents
5. Measurements of the cell population showed that application of plane shock waves increases the growth of endothelial cells suspended in liquid. Real-time PCR measurements of gene expression confirmed this result and showed that the proteinaceous sensors on the cell membrane can detect high-frequency pressure waves, such as shock waves.

Acknowledgments

This work was partially supported by Grant-in-Aid for Scientific Research on Priority Areas (#15086213) from the Ministry of Education, Culture, Sports, Science and Technology of Japan, Grant-in-Aid for Scientific Research (B) (#16360092) from the Japan Society for the Promotion of Science and Grant-in-Aid for Exploratory Research (#16656065) from the Ministry of Education, Culture, Sports, Science and Technology of Japan.

References

1. Takemasa, T., Sugimoto, K., Yamashita, K., 1997. Amplitude-dependent stress fiber reorientation in early response to cyclic strain. Exp. Cell Res. 230, 407-410.
2. Wang, H., Ip, W., Boissy, R., Grood, E.S., 1995. Cell orientation response to cyclically deformed substrates: Experimental validation of a cell model. J. Biomech. 28, 1543-1552.
3. Yamada, H., Ando, H., 2007. Orientation of apical and basal actin stress fibers in isolated and subconfluent endothelial cells as an early response to cyclic stretching. Mol. Cell. Biomech., in press.
4. Wang, J.H.-C., Goldschmidt-Clermont, P., Moldovan, N., Yin, F.C.-P., 2000. Leukotrienes and tyrosine phosphorylation mediate stretching-induced actin cytoskeletal remodeling in endothelial cells. Cell Motil. Cytoskeleton 46, 137-145.
5. Yamada, H., Morita, D., Matsumura, J., Takemasa, T., Yamaguchi, T., 2002. Numerical simulation of stress fiber orientation in cultured endothelial cells under biaxial cyclic deformation using the strain limit hypothesis. JSME Int. J. 45C, 880-888.

6. Yamada, H., Ando, H., Morita, D., 2006. Numerical simulation of the effects of actin binding and cellular deformation on the orientation of actin stress fibers under cyclic stretch. In: Wada, H. (Ed.), Biomechanics at Micro- and Nanoscale Levels, Vol. II, World Scientific, pp. 149-159.
7. Caille, N., Thoumine, O., Tardy, Y., Meister, J.-J., 2002. Contribution of the nucleus to the mechanical properties of endothelial cells. J. Biomech. 35, 177-187.
8. Yamada, H., Matsumura, J., 2004. Finite element analysis of the mechanical behavior of a vascular endothelial cell in culture under substrate stretch. Trans. JSME, 70A, 710-716 (in Japanese).
9. Yamada, H., Kageyama, D., Takahashi, Y., 2004. Modeling of an endothelial cell taking account of elasticity in cell membrane and fluid pressure in cytoplasm. Proceedings of the 16th Bioengineering Conference, JSME, pp. 17-18 (in Japanese).
10. Yamada, H., Ishiguro, H., Tamagawa, M., 2005. Mechanical behavior and structural changes of cells subjected to mechanical stimuli: Deformation, freezing, and shock waves. In: Wada, H. (Ed.), Biomechanics at Micro- and Nanoscale Levels, Vol. I, World Scientific, pp. 154-164.
11. Yamada, H., Kageyama, D., 2004. Geometry-dependent deformations of the vascular endothelial cell: Investigation of intracellular behavior with finite element analysis. Proceedings of the First Asian Pacific Conference on Biomechanics, pp. 233-234, Osaka, Japan.
12. Yamada, H., Takahashi, Y., 2005. Three-dimensional finite element modeling of a vascular endothelial cell based on confocal microscopic images at unstretched and stretched states. Proceedings of the Second Asian Pacific Conference on Biomechanics, 2 pages in CD-ROM, Taipei, Taiwan.
13. Yamada, H., Mouri, N., 2006. Measurement of the contours of cultured vascular endothelial cells on a stretched substrate with confocal laser scanning microscopy. Proceedings of the Mechanical Engineering Congress, 2006 Japan, No. 06-1, Vol. 5, pp. 221-222, Kumamoto, Japan (in Japanese).
14. Yamada, H., Nobuhara, S., 2007. Finite element analysis of the vascular endothelial cell using an entire cell model with cytoplasm and nucleus. Proceedings of the 19th Bioengineering Conference, 2006 Annual Meeting of BED/JSME, No. 06-65, pp. 126-127, Sendai, Japan (in Japanese).
15. Venkatasubramanian, R.T., Grassl, E.D., Barocas, V.H., Lafontaine, D., Bischof, J.C., 2006. Effects of freezing and cryopreservation on the mechanical properties of arteries. Ann. Biomed. Eng. 34, 823-832.
16. Yamada, H., Fujisaki, K., Ishiguro, H., 2006. Comparison of the tensile deformation behavior of porcine aorta before and after the process of freezing and thawing. Proceedings of the 17th JSME Conference on Frontiers in Bioengineering, No. 06-46, pp. 95-96, Ueda, Japan (in Japanese).

17. Yasuno, K., Yamada, H., 2007. Description of the deformation behavior of porcine aorta under uniaxial loading using a model with elastic and collagen fibers and a fluid phase, Proceedings of the 60th Kyushu Branch Regular Meeting of the JSME, No. 078-1, pp. 197-198, Kitakyushu, Japan (in Japanese).
18. Ishiguro, H., Fujikawa, S., Kajigaya, H., Yamada, H., 2007. Freezing behavior and histological change of complex tissues. Aorta. Cryobiology 55, in press.
19. Tamagawa, M., Yamanoi, I., 2001. Fundamental investigation for developing drug delivery systems and bioprocess with shock waves and bubbles. JSME Int. J. 44C, 1031-1040.

This page intentionally left blank

SUBJECT INDEX